Monthly Notices
of the
ROYAL ASTRONOMICAL SOCIETY

MNRAS **471,** 100–143 (2017)
Advance Access publication 2017 June 15

doi:10.1093/mnras/stx1357

The Hi-GAL compact source catalogue – I. The physical properties of the clumps in the inner Galaxy ($-71.^{\circ}0 < \ell < 67.^{\circ}0$)

Davide Elia,[1★] S. Molinari,[1] E. Schisano,[1] M. Pestalozzi,[1] S. Pezzuto,[1] M. Merello,[1] A. Noriega-Crespo,[2] T. J. T. Moore,[3] D. Russeil,[4] J. C. Mottram,[5] R. Paladini,[6] F. Strafella,[7] M. Benedettini,[1] J. P. Bernard,[8,9] A. Di Giorgio,[1] D. J. Eden,[3] Y. Fukui,[10] R. Plume,[11] J. Bally,[12] P. G. Martin,[13] S. E. Ragan,[14] S. E. Jaffa,[15] F. Motte,[16,17] L. Olmi,[18] N. Schneider,[19] L. Testi,[20,18] F. Wyrowski,[21] A. Zavagno,[4] L. Calzoletti,[22,23] F. Faustini,[22] P. Natoli,[24] P. Palmeirim,[4,25] F. Piacentini,[26] L. Piazzo,[27] G. L. Pilbratt,[28] D. Polychroni,[29] A. Baldeschi,[1] M. T. Beltrán,[18] N. Billot,[30] L. Cambrésy,[31] R. Cesaroni,[18] P. García-Lario,[23] M. G. Hoare,[14] M. Huang,[32] G. Joncas,[33] S. J. Liu,[1] B. M. T. Maiolo,[7] K. A. Marsh,[15] Y. Maruccia,[7] P. Mège,[4] N. Peretto,[15] K. L. J. Rygl,[34] P. Schilke,[19] M. A. Thompson,[35] A. Traficante,[1] G. Umana,[36] M. Veneziani,[6] D. Ward-Thompson,[37] A. P. Whitworth,[15] H. Arab,[31] M. Bandieramonte,[38] U. Becciani,[36] M. Brescia,[39] C. Buemi,[36] F. Bufano,[36] R. Butora,[40] S. Cavuoti,[41,39] A. Costa,[36] E. Fiorellino,[1,26] A. Hajnal,[42] T. Hayakawa,[10] P. Kacsuk,[42] P. Leto,[36] G. Li Causi,[1] N. Marchili,[1] S. Martinavarro-Armengol,[43,44] A. Mercurio,[39] M. Molinaro,[40] G. Riccio,[39] H. Sano,[10] E. Sciacca,[36] K. Tachihara,[10] K. Torii,[45] C. Trigilio,[36] F. Vitello[36] and H. Yamamoto[10]

Affiliations are listed at the end of the paper

Accepted 2017 May 31. Received 2017 May 25; in original form 2016 September 15

ABSTRACT

Hi-GAL (Herschel InfraRed Galactic Plane Survey) is a large-scale survey of the Galactic plane, performed with *Herschel* in five infrared continuum bands between 70 and 500 μm. We present a band-merged catalogue of spatially matched sources and their properties derived from fits to the spectral energy distributions (SEDs) and heliocentric distances, based on the photometric catalogues presented in Molinari et al., covering the portion of Galactic plane $-71.^{\circ}0 < \ell < 67.^{\circ}0$. The band-merged catalogue contains 100 922 sources with a regular SED, 24 584 of which show a 70-μm counterpart and are thus considered protostellar, while the remainder are considered starless. Thanks to this huge number of sources, we are able to carry out a preliminary analysis of early stages of star formation, identifying the conditions that characterize different evolutionary phases on a statistically significant basis. We calculate surface densities to investigate the gravitational stability of clumps and their potential to form massive stars. We also explore evolutionary status metrics such as the dust temperature, luminosity and bolometric temperature, finding that these are higher in protostellar sources compared to pre-stellar ones. The surface density of sources follows an increasing trend as they evolve from pre-stellar to protostellar, but then it is found to decrease again in the majority of the most evolved clumps. Finally, we study the physical parameters of sources with respect

★ E-mail: davide.elia@iaps.inaf.it

to Galactic longitude and the association with spiral arms, finding only minor or no differences between the average evolutionary status of sources in the fourth and first Galactic quadrants, or between 'on-arm' and 'interarm' positions.

Key words: catalogues – ISM: clouds – dust, extinction – local interstellar matter – infrared: ISM – submillimetre: ISM.

1 INTRODUCTION

The formation of stars remains one of the most important unsolved problems in modern astrophysics. In particular, it is not clear how massive stars ($M > 8$ M$_\odot$) form, despite their importance in the evolution of the Galactic ecosystem (e.g. Ferrière 2001; Bally & Zinnecker 2005). The formation of high-mass stars is not as well-understood as that of low-mass stars, mainly because of a lack of observational facts upon which models can be built. High-mass stars are intrinsically difficult to observe because of their low number in the Galaxy, their large distance from the Sun and their rapid evolution. Numerous observational surveys have been undertaken in recent years in different wavebands to obtain better statistics on massive pre-stellar and protostellar objects. (Jackson et al. 2006; Stil et al. 2006; Lawrence et al. 2007; Carey et al. 2009; Churchwell et al. 2009; Schuller et al. 2009; Rosolowsky et al. 2010; Hoare et al. 2012; Urquhart et al. 2014a; Moore et al. 2015). Among these, Hi-GAL (Herschel InfraRed Galactic Plane Survey) is the only complete far-infrared (FIR) survey of the Galactic plane.

Hi-GAL (Molinari et al. 2010a) is an Open Time Key Project, which was granted about 1000 h of observing time using the *Herschel Space Observatory* (Pilbratt et al. 2010). It delivers a complete and homogeneous survey of the Galactic plane in five continuum FIR bands between 70 and 500 μm. This wavelength coverage allows us to trace the peak of emission of most of the cold ($T < 20$ K) dust in the Milky Way at high resolution for the first time, material that is expected to trace the early stages of the formation of stars across the mass spectrum. Hi-GAL data were taken using in parallel two of the three instruments aboard *Herschel*, PACS (70- and 160-μm bands, Poglitsch et al. 2010) and SPIRE (250-, 350- and 500-μm bands, Griffin et al. 2010).

This paper is meant to complete the discussions presented in Molinari et al. (2016a) on the construction of the photometric catalogue for the portion of Galaxy in the range $-71.^\circ0 \lesssim \ell \lesssim 67.^\circ0$, $|b| < 1.^\circ0$, an area corresponding to the first Hi-GAL proposal (subsequently extended to the whole Galactic plane). In particular, here we explain how we went from the photometric catalogue to the physical one, introducing band-merging, searching for counterparts, assigning distances as well as constructing and fitting spectral energy distributions (SEDs). In the last part of this paper, in which the distribution of sources with respect to their position in the Galactic plane is analysed in detail, we focus on two regions, i.e. $289.^\circ0 < \ell < 340.^\circ0$ and $33.^\circ0 < \ell < 67.^\circ0$. The innermost part of the Galactic plane, including the Galactic Centre, where the kinematic distance estimate is particularly problematic, will be discussed in a separated paper (Bally et al., in preparation), while the two longitude ranges containing the two tips of the Galactic bar ($340.^\circ0 < \ell < 350.^\circ0$ and $19.^\circ0 < \ell < 33.^\circ0$) have been presented in Veneziani et al. (2017).

1.1 Brief presentation of the surveyed regions

1.1.1 Fourth Galactic quadrant

In the longitude range investigated in more detail in this paper, three spiral arms are in view (see Fig. 1), according to a four-armed spiral model of the Milky Way (Urquhart et al. 2014a, and references therein). Moving towards the Galactic Centre, for $289^\circ \lesssim \ell \lesssim 310^\circ$ the Carina–Sagittarius arm is observed, while at $\ell \sim 310^\circ$ the tangent point of the Scutum–Crux arm is encountered (García et al. 2014). The emission from this latter arm is expected to dominate up to the tangent point of the Norma arm at $\ell \sim 330^\circ$. Around this longitude, the main peak of the OB star formation distribution across the Galaxy is found (Bronfman et al. 2000). Finally, the tangent point of the subsequent arm, the so-called *3-kpc* arm, is located at $\ell \sim 338^\circ$ (García et al. 2014), i.e. very close to the inner limit of the investigated zone.

Significant star formation activity is found in the surveyed region, as testified by the presence of 103 out of 481 star-forming complexes in the list of Russeil (2003), and of 393 star-forming regions out of 1735 in the Avedisova (2000) overall catalogue, of which 29 are Hα-emission regions of the RCW catalogue (Rodgers, Campbell & Whiteoak 1960). Furthermore, 337 out of 1449 regions with embedded OB stars of the Bronfman, Nyman & May (1996) and Bronfman et al. (2000) list are found in this region of the sky.

Hi-GAL observations of the fourth Galactic quadrant have already been used for studying InfraRed Dark Clouds (IRDCs, Egan et al. 1998) in the $300^\circ \lesssim \ell \lesssim 30^\circ$, $|b| \leq 1^\circ$ range (Wilcock et al. 2012a,b), highlighting the fundamental role of the *Herschel* FIR data for exploring the internal structure of these candidate sites for massive star formation. Furthermore, Veneziani et al. (2017) used the catalogue presented here to study the compact source population in the far tip of the long Galactic bar. These data will be exploited, if needed, in this article as well, for instance, for comparison between the fields studied in this paper and inner regions of the Galaxy.

Finally, the nearby Coalsack nebula ($d = 100$–200 pc, see references in Beuther et al. 2011) is also seen in the foreground of our field ($300^\circ \lesssim \ell \lesssim 307^\circ$, Wang et al. 2013). It is one of the most prominent dark clouds in the southern Milky Way but shows no evidence of recent star formation (e.g. Kato et al. 1999; Kainulainen et al. 2009).

1.1.2 First Galactic quadrant

In the first quadrant portion investigated in more detail in this paper ($33^\circ \lesssim \ell \lesssim 67^\circ$), two spiral arms are in view, namely the Carina–Sagittarius and the Perseus arms. The Carina–Sagittarius tangent point is found at $\ell \simeq 51^\circ$ (Vallée 2008) near the W51 star-forming region. From here to the endpoint of the region we are considering, only the Perseus arm is expected.

This area is smaller than that surveyed in the fourth quadrant and has a lower rate of star formation activity per unit area. Russeil (2003) finds 33 star-forming regions in this area, and Avedisova (2000) finds just 97.

Hi-GAL studies of this portion of the Galactic plane focused so far mainly on one of the two Herschel Science Demonstration Phase fields, namely the one centred around $\ell = 59^\circ$, regarding compact source physical properties obtained from earlier attempts of photometry of Hi-GAL maps (Elia et al. 2010; Beltrán et al. 2013; Olmi et al. 2013; Veneziani et al. 2013), structure of IRDCs (Peretto et al. 2010; Battersby et al. 2011), source and filament large-scale disposition (Bally et al. 2010; Molinari et al. 2010b; Billot et al.

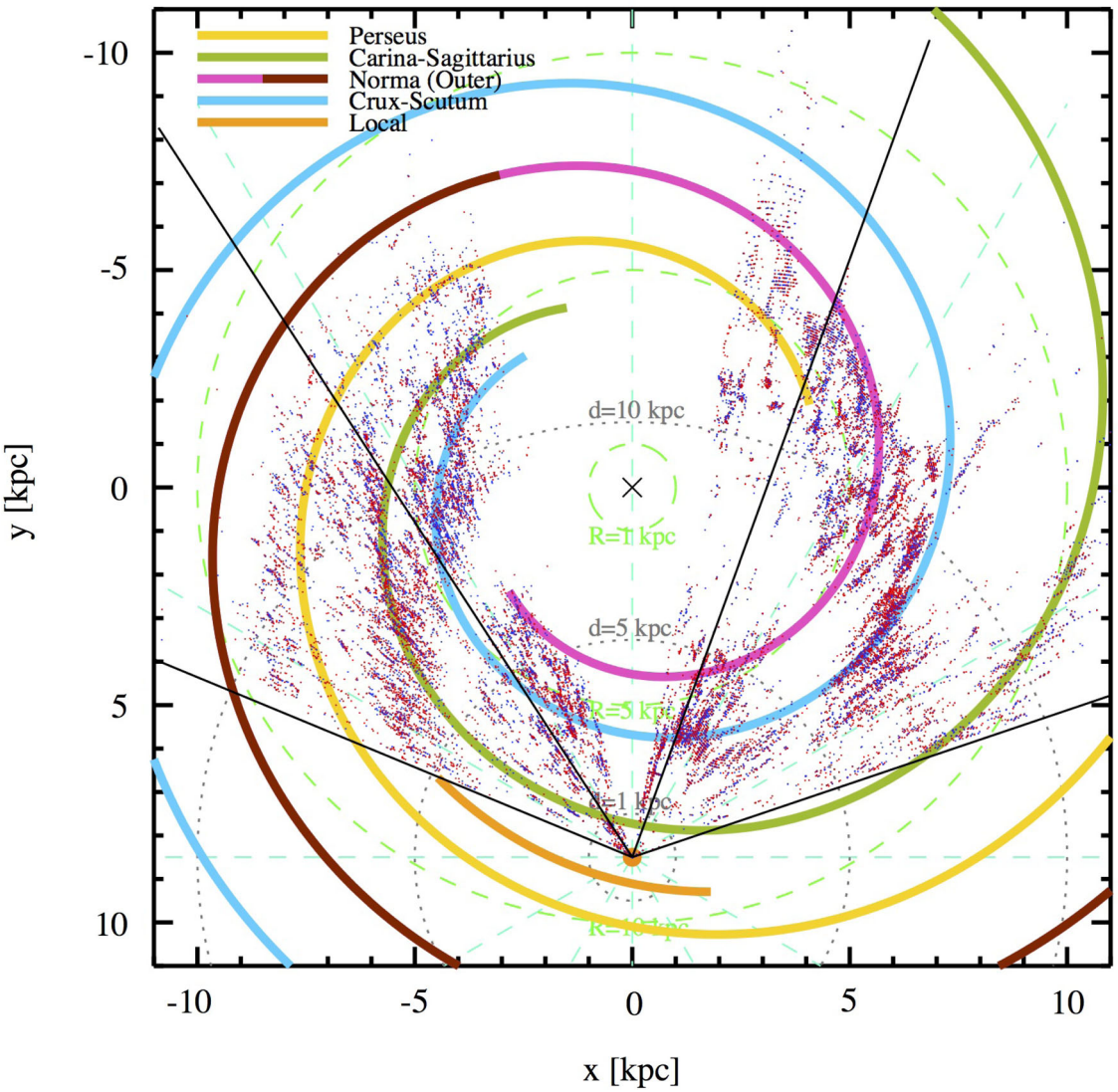

Figure 1. Plot of the position in the Galactic plane of the pre-stellar (red dots) and protostellar (blue dots) Hi-GAL objects provided with a distance estimate. Unbound objects are not shown to reduce the crowding of the plot. For definitions of pre-stellar, protostellar and unbound objects, see Section 3.5. Two pairs of black solid lines delimit the longitude ranges analysed in this paper. Further sources are found closer to the Galactic Centre, most of which are analysed in Veneziani et al. (2017, see their fig. 1). In the inner zone devoid of points, distances were not estimated (see text); thus, only distance-independent source properties were derived. The Galactic Centre is indicated with a $\times$ symbol at coordinates $[x, y] = [0, 0]$ and the Sun with an orange dot at coordinates [0, 8.5], at the bottom of the plot. Cyan dashed lines indicate the Galactic longitude in steps of 30°. *R* denote Galactocentric distances (light-green dashed circles) and *d* denote heliocentric ones (grey dotted circles), with the following steps: 1, 5 and 10 kpc. Spiral arms, from the four-arm Milky Way prescription of Hou, Han & Shi (2009), are plotted with different colours, with the arc–colour correspondence reported in the upper left-hand corner of the plot. In particular, the Norma arm is represented using two colours: magenta for the inner part of the arm and brown for the portion of it generally designated as the outer arm, which starting point is established by comparison with Momany et al. (2006). Finally, the local arm, not included in the model of Hou et al. (2009), is drawn, taken from Xu et al. (2016).

2011) and diffuse emission morphology (Martin et al. 2010). As in the case of the fourth quadrant, the catalogue presented here has already been used by Veneziani et al. (2017) for studying the clump population at the near tip of the Galactic bar. Finally, a recent paper of Eden et al. (2015) focused on two lines of sight centred towards $\ell = 30^\circ$ and 40°, studying arm/interarm differences in luminosity distribution of Hi-GAL sources.

1.2 Structure of this paper

This paper is organized as follows. In Section 2, the data reduction, source detection and photometry strategy are briefly presented, referring to Molinari et al. (2010a) for further detail. In Section 3, SED building, filtering, complementing with ancillary photometry and distances are described. In Section 4, the use of a simple radiative model to derive the physical parameters of the Hi-GAL SEDs is illustrated, while the extraction of such properties from the photometry is summarized in Section 5. The statistics of the physical properties are discussed in Section 6, and the implications on the estimate of the evolutionary stage of sources are reported in Section 7. Finally, in Section 8, source properties are correlated with their Galactic positions: A comparison between sources in the fourth and first Galactic quadrants is provided, and, after positional matching of the sources and the locations of Galactic spiral arms,

the behaviour of arm versus interarm sources is briefly discussed. Further details on how the catalogue is organized, and on possible biases affecting the listed quantities, are provided in the appendices at the end of this paper.

2 DATA: MAP MAKING AND COMPACT SOURCE EXTRACTION

The technical features of the Hi-GAL survey are presented in Molinari et al. (2010a); therefore, here we limit ourselves to a summary of only the most relevant aspects. The Galactic plane was divided into 2×2 deg^2 sections, called 'tiles', that were observed with *Herschel* at a scan speed of 60 arcsec s^{-1} in two orthogonal directions. PACS and SPIRE were used in 'parallel mode', i.e. data were taken simultaneously with both instruments (and therefore at all five bands). Note that when used in parallel mode, PACS and SPIRE observe a slightly different region of sky. A more complete coverage is nevertheless recovered when considering contiguous tiles; remaining areas of the sky covered only by either one of the two are not considered for science in this paper. Single maps of the Hi-GAL tiles were obtained from PACS/SPIRE detector timelines using a pipeline specifically developed for Hi-GAL and containing the ROMAGAL map-making algorithm (Traficante et al. 2011) and the WGLS post-processing (Piazzo et al. 2012) for removing artefacts in the maps.

Astrometric consistency with *Spitzer* MIPSGAL 24-μm data (Carey et al. 2009, http://mipsgal.ipac.caltech.edu/) is obtained by applying a rigid shift to the entire mosaic. This is obtained as the mean shift measured on a number of bright and isolated sources common to *Spitzer* 24-μm and Hi-GAL PACS 70-μm data.

The further astrometric registration of SPIRE maps is then carried out by repeating the same procedure, but comparing counterparts of the same source at 160 and 250 μm.

Compact sources were detected and extracted using the algorithm CuTEx (Molinari et al. 2011), which is based on the study of the curvature of the images. This is done by calculating the second derivative at any pixel of the Hi-GAL images, efficiently damping all emission varying on intermediate to large spatial scales, and amplifying emission concentrated in small scales. This principle is particularly advantageous when extracting sources that appear within a bright and highly variable background emission. The final integrated fluxes are then estimated by CuTEx through a bi-dimensional Gaussian fit to the source profile. All details of the photometric catalogue are presented by Molinari et al. (2016a), who also report estimates of the completeness limits in flux in each band, measured by extracting a controlled 90 per cent sample of sources artificially spread on a representative sample of real images. Such limits in the regions investigated in this paper are discussed in Appendix C2 for their implications on the estimate of source mass completeness limits as a function of the heliocentric distance.

The final version of the single-band catalogues of the portion of Hi-GAL data presented here contains 123 210, 308 509, 280 685, 160 972 and 85 460 entries in the 70-, 160-, 250-, 350- and 500-μm bands, respectively.

3 FROM PHOTOMETRY TO PHYSICS

This paper focuses on the study of compact cold objects extracted from *Herschel* data. Within this framework, a final catalogue of objects for scientific studies has been obtained by merging the Hi-GAL single-band photometric catalogues and filtering the resulting five-band catalogue, applying specific constraints to the source SEDs. In the following sections, the steps of these processes are explained in detail: band-merging, search for counterparts beyond the *Herschel* frequency coverage, assigning distances, SED filtering and fitting.

3.1 Band-merging and source selection

The first step for creating a multiwavelength catalogue consists of assigning counterparts of a given source across *Herschel* bands. This operation is based on iterating a positional matching (cf. Elia et al. 2010, 2013) between source lists obtained at two adjacent bands. In this paper, however, instead of assuming a fixed matching radius as done in previous works, the matching region consisted of the ellipse describing the source at the longer of the two wavelengths.[1] In other words, a source has a counterpart at shorter wavelength if the centroid of the latter falls within the ellipse fitted to the former. In this way, it is possible that more than one counterpart fall into the longer wavelength ellipse. In such multiplicity cases, the association is established only with the short-wavelength counterpart closest to the long-wavelength ellipse centroid.[2] The remaining ones are reported as independent catalogue entries, and considered for further possible counterpart search at shorter wavelengths. At the end of the five band-merging, a catalogue is produced, in which each entry can contain from one to five detections in as many bands.

The subsequent step is to filter the obtained five-band catalogue in order to identify SEDs that are eligible for the modified blackbody (hereafter grey body) fit, hence to derive the physical properties of the objects. This selection is based on considerations of the regularity of the SEDs in the range 160–500 μm, since the 70-μm band is generally expected to depart from the grey-body behaviour (e.g. Bontemps et al. 2010; Schneider et al. 2012).

First of all, as done in Elia et al. (2013), only sources belonging to the common PACS+SPIRE area and detected at least in three consecutive *Herschel* bands (i.e. the combinations 160–250–350 μm or 250–350–500 μm or, obviously, 160–250–350–500 μm) were selected.

Secondly, fluxes at 350 and 500 μm were scaled according to the ratio of deconvolved source linear sizes, taking as a reference the size at 250 μm (cf. Motte et al. 2010a; Nguyen Luong et al. 2011). This choice is supported by the fact that cold dust is expected to have significant emission around 250 μm; also, according to the adopted constraints to filter the SEDs, this is the shortest wavelength in common for all the selected SEDs. Finally, we searched for further irregularities in the SEDs such as dips in the middle, or peaks at 500 μm.

At the end of the filtering pipeline, we remain with 100 922 sources. For each of these sources, we estimate physical parameters such as dust temperature, surface density and, when distance is available, linear size, mass and luminosity, by fitting a single-temperature grey body to the SED. The details of this procedure are described in Section 4. Clearly, the determination of source physical quantities such as temperature and mass is more reliable when a better coverage of the SED is available. Based on the selection criteria listed above, sources in our catalogue can be confirmed, even considering the 70-μm flux, with detections at only three bands: This is the case for combinations 160–250–350 μm (with no detection at 70 μm) and 250–350–500 μm (that we call 'SPIRE-only' sources),

[1] Such ellipse corresponds to the half-height section of the two-dimensional Gaussian fitted by CuTEx to the source profile.

[2] For the 70-μm band, we also take into account possible multiplicity for the estimate of the bolometric luminosity, as is explained in Section 4.

Table 1. Number of sources in the Hi-GAL catalogue, in ranges of longitude.

Longitude range	Protostellar		Highly reliable starless (pre-stellar)		Poorly reliable starless (pre-stellar)		Total
	w/ distance	w/o distance	w/ distance	w/o distance	w/ distance	w/o distance	
$-71^\circ \leq \ell < -20^\circ$	8227	1425	10 384 (9598)	2978 (2265)	10 696 (7531)	3321 (1519)	37 031
$-20^\circ \leq \ell < -10^\circ$	1752	273	2667 (2506)	611 (537)	2548 (1855)	591 (345)	8442
$-10^\circ \leq \ell < 0^\circ$	0	2154	0 (0)	3357 (3139)	0 (0)	3417 (2544)	8928
$0^\circ \leq \ell < 19^\circ$	505	3165	398 (380)	5689 (5271)	318 (249)	5488 (4053)	15 563
$19^\circ \leq \ell < 33^\circ$	2646	549	3172 (2893)	1260 (1068)	3045 (2200)	1312 (832)	11 984
$33^\circ \leq \ell < 67^\circ$	2704	1184	4189 (3818)	3149 (2548)	3814 (2520)	3934 (2000)	18 974
Total	15 834	8750	20 810 (19 195)	17 044 (14 828)	20 421 (14 355)	18 063 (11 293)	100 922

which we consider as genuine SEDs, although more affected by a less reliable fit (especially the SPIRE-only case, in which it might be difficult to constrain the SED peak, and consequently the temperature). For this reason, after the SED filtering procedure, we further split our SEDs into two sub-catalogues: 'high reliability' (62 438 sources) and 'low reliability' (38 484 sources). Notice that, according to the definitions that will be provided in Section 3.5, all the sources in the latter list belong to the class of 'starless' compact sources.

In Table 1, the source number statistics for the band-merged catalogue are provided, divided in ranges of longitude (identified by the two intervals studied by Veneziani et al. 2017) and in evolutionary stages introduced in Section 3.5.

3.2 Caveats on SED building and selection

Building a five-band catalogue and selecting reliable sources for scientific analysis require a set of choices and assumptions, which have been described in the previous sections. Here we collect and explicitly recall all of them to focus the reader's attention on the limitations that must be kept in mind when using the Hi-GAL physical catalogue:

(i) The concept of 'compact source' used for this catalogue refers to unresolved or poorly resolved structures, whose size, therefore, does not exceed a few instrumental PSFs ($\lesssim 3$, Molinari et al. 2016a). Structures with larger angular sizes – such as a bright diffuse interstellar medium (ISM), filaments or bubbles – escape from this definition and are not considered in the present catalogue.

(ii) The appearance of the sky varies strongly throughout the wavelength range covered by *Herschel*. The lack of a detection in a given band may be ascribed to a detection error, or to the physical conditions of the source as, for instance, the case of a warm source seen by PACS but undetectable at the SPIRE wavelengths. In this respect, the present catalogue does not aim to describe all star formation activity within the survey area, but rather to provide a census of the coldest compact structures, corresponding to early evolutionary stages in which internal star formation activity has not yet been able to dissipate the dust envelope, or has not started at all. Detections at 70 μm only, or at 70/160 μm, or at 70/160/250 μm, are expected to have counterparts in the mid-IR (MIR); such cases, corresponding to more evolved objects, surely deserve to be further studied, but this lies out of the aims of this paper and is reserved for future works.

(iii) The band-merging procedure works fine in the ideal case of a source detected at all wavelengths as a bright and isolated peak. Possible multiplicities, however, can produce multiple branches in the counterpart association, so that, for instance, the flux at a given wavelength might result from the contributions of two or more counterparts detected separately at shorter wavelengths. This can also introduce inconsistent fluxes in the SEDs and produce irregularities such that several bright sources present in the Hi-GAL maps might be ruled out from the final catalogue according to the constraints described in Section 3.1.

(iv) Very bright sources might be ruled out by the filtering algorithm due to saturation occurring at one or more bands, which produces unrecoverable gaps in the SEDs.

(v) The physical properties derived from *Herschel* SED analysis (see next sections) are global (e.g. mass, luminosity) or average (e.g. temperature) quantities for sources that, depending on their distance, can be characterized by a certain degree of internal but unresolved structure (see Section 6.1), as will be discussed in Appendix C.

3.3 Counterparts at non-*Herschel* wavelengths

For every entry in the band-merged filtered catalogue, we searched for counterparts at 24 μm (MIPSGAL, Gutermuth & Heyer 2015) as well as at 21 μm (*MSX*, Egan et al. 2003) and 22 μm (*WISE*, Wright et al. 2010). The fluxes of these counterparts, typically associated with a warm internal component of the clump, are not considered for subsequent grey-body fitting of the portion of the SED associated with cold dust emission, but only for estimating the source bolometric luminosity.

In particular, we notice that the choice of sources in the catalogue of Gutermuth & Heyer (2015) is rather conservative, and only a small fraction has $F_{24} < 0.005$ Jy. For this reason, we performed an additional search of sources in the MIPSGAL maps, using the APEX source extractor[3] (Makovoz & Marleau 2005), in order to recover those sources that, from a visual inspection of the maps, appear to be real, although for some reason were not included in the original catalogue. Furthermore, as a cross-check, a similar procedure has been performed also with DAOFIND (Stetson 1987), and only sources confirmed by this have been added to the photometry list of Gutermuth & Heyer (2015). Following this procedure, approximately 2000 additional SEDs have been complemented with a flux at 24 μm, mostly having fluxes in the range $0.0001 < F_{24} < 0.001$ Jy. The risk of adding poorly reliable sources with low signal-to-noise ratio is mitigated by the fact that 24-μm counterparts of our *Herschel* sources are considered for scientific analysis only if they are confirmed by a detection at 70 μm (see Section 3.5 and Appendix B).

To assign counterparts to the Hi-GAL sources at 21, 22 and 24 μm, the ellipse representing the source at 250 μm was used as the matching region, and the flux of all counterparts at a given wavelength within this region was summed up into one value. Indeed,

[3] http://irsa.ipac.caltech.edu/data/SPITZER/docs/dataanalysistools/tools/mopex/

possible occurrences of multiplicity can induce a relevant contribution at MIR wavelengths in the calculation of the bolometric luminosity of Hi-GAL sources.

On the long-wavelength side of the SED, we cross-matched our band-merged and filtered catalogue with those of Csengeri et al. (2014) from the ATLASGAL survey (870 μm, Schuller et al. 2009) and of Ginsburg et al. (2013) from the BOLOCAM Galactic Plane Survey (BGPS, 1.1 mm, Rosolowsky et al. 2010; Aguirre et al. 2011). The adopted searching radius was 19 arcsec for the former and 33 arcsec for the latter, corresponding to the full width at half-maximum of the instruments at the observed wavelengths. Out of 10 861 entries in the ATLASGAL catalogue, 10 517 of them lie inside the PACS+SPIRE common science area considered in this paper, of which 6136 are found to be associated with a source of our catalogue through this 1:1 matching strategy. Similarly, 6020 out of 8594 entries of the BGPS catalogue lie in the common science area, of which 4618 turn out to be associated with an entry of our catalogue. Finally, access to ATLASGAL images allowed us to extract further counterparts, not reported in the list of Csengeri et al. (2014), by using CuTEx. In cases in which the deconvolved size of the ATLASGAL and/or BGPS counterpart is larger than the one measured at 250 μm, fluxes were rescaled according to the procedure described in Section 3.1.

3.4 Distance determination

Assigning distances to sources is a crucial step in the process of giving physical significance to the information extracted from Hi-GAL data. While reliable distance estimates are available for a limited number of known objects, as, for example, H II regions (e.g. Fish et al. 2003) or masers (e.g. Green & McClure-Griffiths 2011), this information does not exist for the majority of Hi-GAL sources. Therefore, we adopted the scheme presented in Russeil et al. (2011), based on the Galactic rotation model of Brand & Blitz (1993), to assign kinematic distances to a large proportion of sources: A ^{12}CO (or ^{13}CO) spectrum is extracted at the line of sight of every Hi-GAL source, and the velocity of the local standard of rest $V_{\rm LSR}$ of the brightest spectral component is assigned to it, allowing the calculation of a kinematic distance. To determine the $V_{\rm LSR}$, the ^{13}CO data from the Five College Radio Astronomy Observatory (FCRAO) Galactic Ring Survey (GRS, Jackson et al. 2006), and ^{12}CO and ^{13}CO data from the Exeter-FCRAO Survey (Brunt et al., in preparation; Mottram et al., in preparation) were used for the portion of Hi-GAL covering the first Galactic quadrant for $\ell < 55^\circ$ and for $\ell > 55^\circ$, respectively. The pixel size of those CO cubes is 22.5 arcsec, corresponding to Nyquist sampling of the FCRAO beam. NANTEN ^{12}CO data (Onishi et al. 2005) were used to assign velocities to Hi-GAL sources in the fourth quadrant. The pixel size of these data is 4 arcmin (against an angular resolution of 2.6 arcmin), so that more than one Hi-GAL source might fall on to the same CO line of sight, and the same distance is assigned to them. The spectral resolutions of the two data sets were 0.15 and 1.0 km s^{-1}, respectively.

Once the $V_{\rm LSR}$ is determined, the near/far distance ambiguity is solved by matching the source positions with a catalogue of sources with known distances (H II regions, masers and others) or, alternatively, with features in extinction maps (in this case, the near distance is assigned). In cases for which none of the aforementioned data can be used, the ambiguity is always arbitrarily solved in favour of the far distance, and a 'bad-quality' flag is given to that assignment.

The additional use of extinction maps to solve for distance ambiguity (Russeil et al. 2011) (where applicable) can be a source of error, whose magnitude typically increases with increasing difference between the near and far heliocentric distance solutions. For this paper, we rely on the use of extinction maps for practical reasons and also because, for most of the sources, no spectral line emission has yet been observed other than what can be extracted from the two CO surveys.

Finally, at present, no distance estimates have been obtained in the longitude range $-10\overset{\circ}{.}2 < \ell < 14\overset{\circ}{.}0$, due to the difficulty in estimating the kinematic distances of sources in the direction of the Galactic Centre. We were able to assign a heliocentric distance to 57 065 sources out of the 100 922 of the band-merged filtered catalogue, i.e. 56 per cent (see also Table 1). However, for 35 904 of these, the near/far ambiguity has not been solved, since the extinction information is not available, and the far distance is assigned by default (see above).

The distribution of sources in the Galactic plane is shown in Fig. 1. It can be seen that the available distances do not produce a clear segregation between high-source-density regions corresponding to spiral arm locations and less populated interarm regions, as will be discussed in more detail in Section 8.2. On one hand, massive star-forming clumps are expected to be organized along spiral arms (e.g. CH_3OH and H_2O masers observed by Xu et al. 2016), while, on the other hand, the large number of sources present in our catalogue, corresponding to a large variety of physical and evolutionary conditions probed with *Herschel*, makes it likely to also include clumps located outside the arms. Any consideration of this aspect is subject to a more correct estimate of heliocentric distances: The work of assigning distances to Hi-GAL sources is still in progress within the VIALACTEA project, and a more refined set of distances (and for an increased number of sources) will be delivered in Russeil et al. (in preparation).

3.5 Starless and protostellar objects

One of the most important steps in the determination of the evolutionary stages of Hi-GAL sources is discriminating between pre-stellar and protostellar sources, namely starless but gravitationally bound objects and objects showing signatures of ongoing star formation, respectively. Here we follow the approach already described in Elia et al. (2013). If a 70-μm counterpart is available, that object can with a high degree of confidence be labelled as protostellar (Dunham et al. 2008; Ragan, Henning & Beuther 2013; Svoboda et al. 2016). This criterion works well for relatively nearby objects, but as soon as we extend our studies to regions farther away than, say, 4–5 kpc, two competing effects concur in confusing the source counts (see also Baldeschi et al. 2017), both affecting the estimates of the star formation rate (SFR). First, at large distances, 70-μm counterparts of relatively low mass sources might be missed (and sources mislabelled) because of limits in sensitivity.[4] Secondly, since the protostellar label is given on the basis of the detection of a 70-μm counterpart, starless and protostellar cores close together and far away could be seen and labelled as a single

[4] For example, applying equation (4) (presented in the following), a grey body with a mass of 50 $M_\odot$, temperature of 15 K, dust emissivity with exponent $\beta = 2$ with the same reference opacity as adopted in this paper (see Section 4) and located at a distance of 10 kpc would have a flux of 0.02 Jy at 70 μm, and of 0.84 Jy at 250 μm, consequently detectable with *Herschel* at the latter band but not at the former (Molinari et al. 2016a).

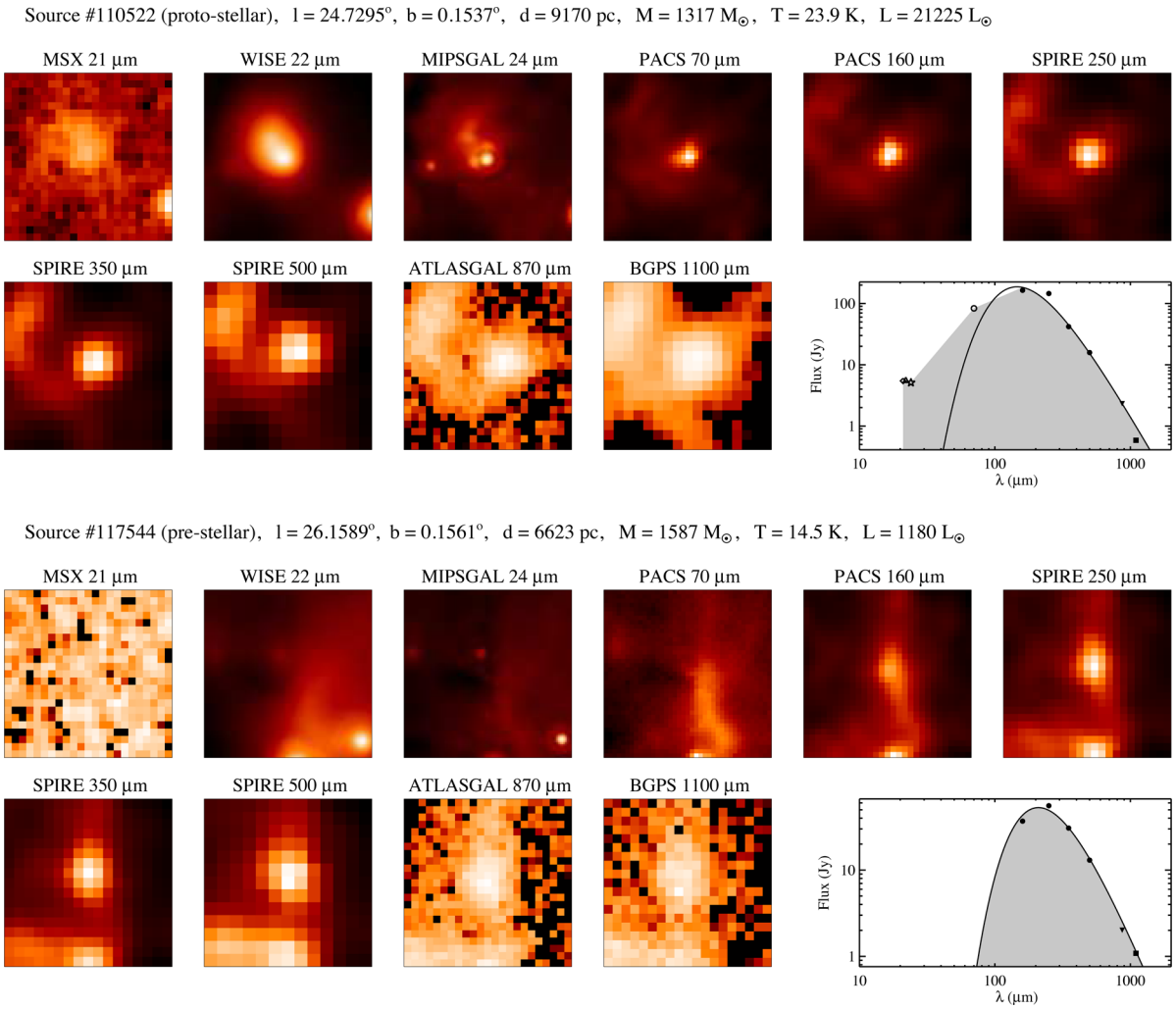

Figure 2. Multiwavelength 2 × 2 arcmin^2 images of two sources listed in our catalogue, to provide an example of a protostellar (upper 11 panels) and a pre-stellar source (lower 11 panels). The source coordinates and physical properties are reported above each set of panels. For each source position, 10 images at 21, 22, 24, 70, 160, 250, 350, 500, 870 and 1100 μm, taken from the survey indicated in the title, are shown (the colour scale is logarithmic, in arbitrary units). Finally, the SED of each of the two sources is shown: filled and open symbols indicate fluxes that are taken into account or not, respectively, for the grey-body fit (solid line, see Section 4). The grey-shaded area is a geometric representation of the integral calculated to estimate the source bolometric luminosity (see Sections 3.3 and 4).

protostellar clump due to lack of resolution. We address this issue in Appendix C1.

To mitigate the first effect, we performed deeper, targeted extractions at PACS wavelengths towards two types of sources. One type consisted of 'SPIRE-only' sources, i.e. sources clearly detected only at 250, 350 and 500 μm. Since SED fitting for such sources is poorly constrained, a further extraction at 160 μm, deeper than that of Molinari et al. (2016a), was required in order to set at least an upper limit for the flux shortwards of what could be the peak of the SED. In this way, 9705 further detections and 9992 upper limits at 160 μm were recovered.

The second type of sources consists of those showing a 160-μm counterpart (original or found after a deeper search) but no detection at 70 μm. To ascertain that the starless nature of these objects is not assigned simply due to a failure of the source-detection process, we performed a deeper search for a 70-μm counterpart towards those targets: In this way, a possible clear counterpart not originally listed in the single-band catalogues would allow us to label the object as protostellar. Adopting this strategy, 912 further detections and 76 215 upper limits at 70 μm were recovered.

Whereas the protostellar objects are expected to host ongoing star formation, the relation between starless objects and star formation processes must be further examined, since only gravitationally bound sources fulfil the conditions for a possible future collapse. Here we use the so-called 'Larson's third relation' to assess if an object can be considered bound: The condition we impose involves the source mass, M, and radius, r (see Sections 4 and 6), and is formulated as $M(r) > 460\,\mathrm{M}_\odot (r/\mathrm{pc})^{1.9}$ (Larson 1981). Masses above this threshold identify bound objects, i.e. genuine pre-stellar aggregates.

In Table 1, the statistics of the sources of the catalogue, divided into protostellar, pre-stellar and starless unbound, are reported, while in Fig. 2 the SEDs and the corresponding grey-body fits are shown for one protostellar and one pre-stellar source, for the sake of example. More details and a discussion about the protostellar-to-pre-stellar source ratio are given in Section 8.1.

One of the aims of this paper is to show the amount of information that can be extracted simply from continuum observations in the FIR/sub-mm, combining Hi-GAL data with other surveys in adjacent wavelength bands and using spectroscopic data only to obtain kinematic distances. On one hand, for many sources, these data can be complemented with line observations to obtain a more detailed picture, while, on the other hand, Hi-GAL produced an unprecedentedly large and unbiased catalogue containing many thousands of newly detected cold clumps, for which it is important to provide a first classification. The criteria we provide to separate different populations, although somewhat conventional in the *Herschel* literature, remain probably too clear-cut and surely affected by biases we introduced in this section and also discussed in the following sections of this paper. Reciprocal contamination of the samples certainly increases overlap of the physical property distributions obtained separately for the different populations, as will be seen in Sections 6 and 7.

4 SED FITTING

Once the SEDs of all entries in the filtered catalogue are built by assembling the photometric information, as explained above, it is possible to fit a single-grey-body function to its $\lambda \geq 160$ μm portion, and therefore derive the mass M and the temperature T of the cold dust in those objects.

Many details on the use of the grey body to model FIR SEDs have been provided and discussed by Elia & Pezzuto (2016). Here we report only concepts and analytic expressions that are appropriate for this paper. The most complete expression for the grey body explicitly contains the optical depth:

$$F_\nu = (1 - \mathrm{e}^{-\tau_\nu}) B_\nu(T_\mathrm{d})\Omega, \quad (1)$$

recently used, e.g. in Giannini et al. (2012), where F_ν is the observed flux density at the frequency ν, $B_\nu(T_\mathrm{d})$ is the Planck function at the dust temperature T_d and Ω is the source solid angle in the sky. The optical depth can be parametrized, in turn, as

$$\tau_\nu = (\nu/\nu_0)^\beta, \quad (2)$$

where the cut-off frequency $\nu_0 = c/\lambda_0$ is such that $\tau_{\nu_0} = 1$, and β is the exponent of the power-law dust emissivity at large wavelengths. After constraining $\beta = 2$, as typically adopted also in the Gould Belt (e.g. Könyves et al. 2015) and HOBYS (e.g. Giannini et al. 2012) consortia, and as recommended by Sadavoy et al. (2013), and Ω to be equal to the source area as measured by CUTEX at the reference wavelength of 250 μm (cf. Elia et al. 2013), the free parameters of the fit remain T and λ_0. For these parameters, we explored the ranges $5 \leq T \leq 40$ K and $5 \leq \lambda_0 \leq 350$ μm, respectively.

The clump mass does not appear explicitly in equation (1) but can be derived from

$$M = \left(d^2\Omega/\kappa_\mathrm{ref}\right)\tau_\mathrm{ref}, \quad (3)$$

as shown by Pezzuto et al. (2012), where κ_ref and τ_ref are the opacity and the optical depth, respectively, estimated at a given reference wavelength λ_ref. To preserve the compatibility with previous works based on other *Herschel* key-projects (e.g. Könyves et al. 2010; Giannini et al. 2012), here we decided to adopt $\kappa_\mathrm{ref} = 0.1$ cm^2 g^{-1} at $\lambda_\mathrm{ref} = 300$ μm (Beckwith et al. 1990, already accounting for a gas-to-dust ratio of 100), while τ_ref can be derived from equation (2). The choice of κ_ref constitutes a critical point (Deharveng et al. 2012; Martin et al. 2012); thus, it is interesting to show how much the mass would change if another estimate of κ_ref were adopted. The dust opacity at 300 μm from the widely used OH5 model (Ossenkopf & Henning 1994) is $\kappa_{300} = 0.13$ cm^2 g^{-1}, which would produce a 30 per cent underestimation of masses with respect to our case. Preibisch et al. (1993) quote $\kappa_{1300} = 0.005$ cm^2 g^{-1}, which, for $\beta = 2$, would correspond to $\kappa_{300} = 0.094$ cm^2 g^{-1}, implying an ∼6 per cent larger mass. Similarly, the value of Netterfield et al. (2009), $\kappa_{250} = 0.16$ cm^2 g^{-1}, would translate into $\kappa_{300} = 0.11$ cm^2 g^{-1}, practically consistent with the value adopted here. However, further literature values of κ_{250} quoted by Netterfield et al. (2009) in their table 3 span an order of magnitude from $\kappa_{250} = 0.024$ cm^2 g^{-1}(Draine & Li 2007) to $\kappa_{250} = 0.22$–0.25 cm^2 g^{-1}(Ossenkopf & Henning 1994), which would lead to a factor from 6 to 0.6 on the masses calculated in this paper.

For very low values of λ_0 (i.e. much shorter than the minimum of the range we consider for the fit, namely 160 μm), the grey body has a negligible optical depth at the considered wavelengths, so that equation (1) can be simplified as follows:

$$F_\nu = \frac{M\kappa_\mathrm{ref}}{d^2}\left(\frac{\nu}{\nu_\mathrm{ref}}\right)^\beta B_\nu(T_\mathrm{d}) \quad (4)$$

(cf. Elia et al. 2010). We note that the estimate of λ_0 does not affect our results significantly when it implies $\tau \leq 0.1$ at 160 μm. According to equation (2) and for $\beta = 2$, we find that the critical value is encountered for $\lambda_0 \sim 50.6$ μm. If the fit procedure using equation (1) provides a λ_0 value shorter than that, the fit is repeated based on equation (4), and the mass and temperature computed in this alternative way are considered as the definitive estimates of these quantities for that source. In Fig. 3, we show how the temperature and mass values obtained through equations (1) (T_tk, M_tk) and (4) (T_tn, M_tn) appear generally equivalent as long as λ_0 (obtained through the former) is much shorter than 160 μm (say, $\lambda <$ 100 μm), since both models have extremely low (or zero) opacities at the wavelengths involved in the fit. Quantitatively speaking, the average and standard deviation of the $T_\mathrm{tk}/T_\mathrm{tn}$ ratio for $\lambda < 160$ μm are 1.01 and 0.02, respectively. However, an increasing discrepancy is visible at increasing λ_0, highlighting the tendency of equation (4) to underestimate the temperature and to overestimate the mass.

SED fitting is performed by χ^2 optimization of a grey-body model on a grid that is refined in successive iterations to converge on the final result. The strategy of generating an SED grid to be compared with data also gives us the advantage of applying PACS colour corrections directly to the model SEDs (since its temperature is known for each of them), rather than correcting the data iteratively (cf. Giannini et al. 2012).

For sources with no assigned distance, a virtual value of 1 kpc was assumed, to allow the fit anyway and distance-independent quantities (such as T) to be derived, and also distance-independent combinations of single distance-dependent quantities (as L_bol/M, see Section 6.5).

The luminosity of the starless objects was estimated using the area under the best-fitting grey body. For protostellar objects, however, the luminosity was calculated by summing two contributions: the area under the best-fitting grey body starting from 160 μm and longwards, plus the area of the observed SED between 21- and 160-μm counterparts (if any) to account for MIR emission contribution exceeding the grey body.

5 SUMMARY OF THE CREATION OF THE SCIENTIFIC CATALOGUE

The generation of the catalogue used for the scientific analysis presented in this paper can be summarized as follows:

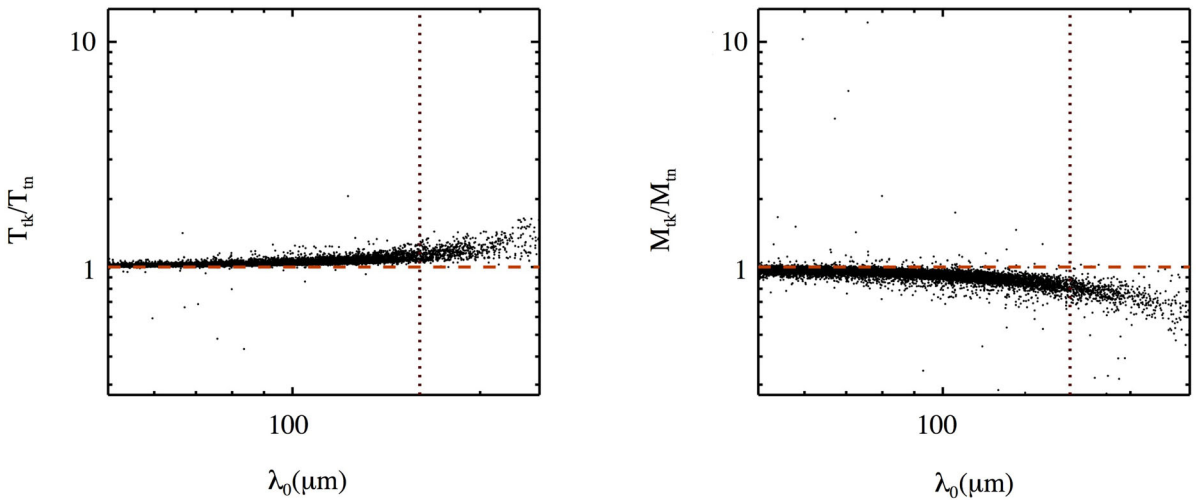

Figure 3. Left-hand panel: ratio of the dust temperatures derived by fitting equations (1) and (4) to SEDs (and denoted here with T_{tk} and T_{tn}, to indicate an optically 'thick' and 'thin' regime, respectively) versus the corresponding λ_0 obtained through equation (1). The x-axis starts from 50.6 μm, corresponding to the minimum value for which this comparison makes sense (see text). The $\lambda_0 = 160$ μm value is highlighted as a reference with a vertical dotted line. The red dashed line represents the $T_{tk} = T_{tn}$ condition. Right-hand panel: the same as the left-hand panel, but for the masses M_{tk} and M_{tn} derived through equations (3) and (4), respectively.

(i) Select the sources located in regions observed with both PACS and SPIRE.

(ii) Perform positional band-merging of single-band catalogues. First, the single-band catalogue at 500 μm is taken, and the closest counterpart in the 350-μm image, if available, is assigned. The same is repeatedly done for shorter wavelengths, up to 70 μm. The ellipse describing the object at a longer wavelength is chosen as the matching region.

(iii) Select sources in the band-merged catalogue that have counterparts in at least three contiguous *Herschel* bands (except the 70 μm) and show a 'regular' SED (with no cavities and not increasing towards longer wavelengths).

(iv) Find counterparts at MIR and mm wavelengths for all entries in the band-merged and filtered catalogues. Shortwards of 70 μm, catalogues at 21, 22 and 24 μm were searched and the corresponding flux reported is the sum of all objects falling in the ellipse at 250 μm. Longwards of 500 μm, counterparts were searched by mining 870-μm ATLASGAL public data, or extracting sources through CuTEx, as well as 1.1-mm BGPS data.

(v) Fill the catalogue where fluxes at 160 and/or at 70 μm were missing, to improve the quality of labelling sources as starless or protostellar (see the next step).

(vi) Move the selected SEDs that remain with only three fluxes in the five Hi-GAL bands to a list of sources with, on average, barely reliable physical parameter estimation.

(vii) Classify sources as protostellar or starless, depending on the presence or lack of a detection at 70 μm, respectively.

(viii) Assign a distance to all sources using the method described in Russeil et al. (2011).

(ix) Fit a grey body to the SED at $\lambda \geq 160$ μm to derive the envelope average temperature, and, for sources provided with a distance estimate, the mass and the luminosity.

(x) Make a further classification, among starless sources, between gravitationally unbound or bound (pre-stellar) sources, based on the mass threshold suggested by Larson's third law.

The catalogue, generated as described above and constituted by two lists ('high reliability' and 'low reliability', respectively), is available for download at http://vialactea.iaps.inaf.it/vialactea/public/HiGAL_clump_catalogue_v1.tar.gz.

The description of the columns is reported in Appendix A.

6 RESULTS

6.1 Physical size

For a source population distributed throughout the Galactic plane at an extremely wide range of heliocentric distances, as in our case, it is fundamental to consider the effective size of these compact objects (i.e. detected within a limited range of angular sizes) in order to assess their nature.

Sure enough, we can derive the linear sizes only for objects with a distance estimate, starting from the angular size estimated at the reference wavelength of 250 μm as the circularized and deconvolved size of the ellipse estimated by CuTEx. In Fig. 4, left-hand panel, we show the relation between the physical diameter and the distance for these sources, highlighting how this quantity is given by the combination of the source angular size and its distance. Given the large spread in distance, a wide range of linear sizes is found, corresponding to very different classes of ISM structures.

In Fig. 4, right-hand panel, we provide the histogram of the diameter D separately for the protostellar, pre-stellar and starless unbound sources, using the subdivision scheme proposed by Bergin & Tafalla (2007) (cores for $D < 0.2$ pc, clumps for $0.2 \geq D \leq 3$ pc and clouds for $D > 3$ pc, although the natural transition between two adjacent classes is far from being so sharp) to highlight how only a small portion of the Hi-GAL compact sources are compatible with a core classification, while most of them are actually clumps. A very small fraction of sources, corresponding to the most distant cases, can be considered as entire clouds. However, given the dominance of the clump-sized sources, it is practical to refer to the sources of the present catalogue with the general term 'clumps'. The underlying, generally inhomogeneous substructure of these clumps is not resolved in our observations, but it can be reasonably supposed that they are composed of a certain number of cores and by an intercore diffuse medium (e.g. Merello et al. 2015) so that, in the

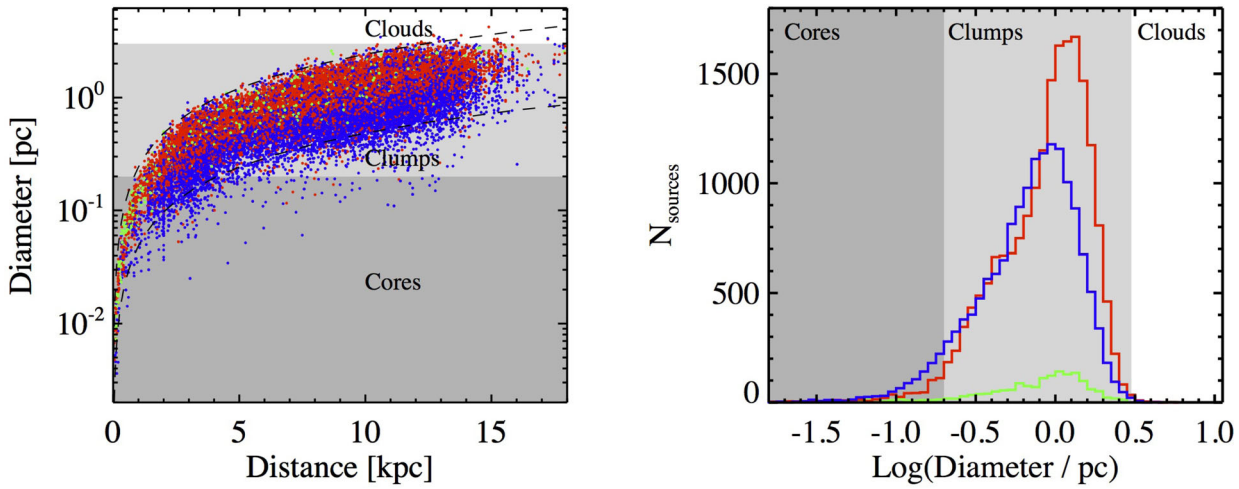

Figure 4. Left-hand panel: Hi-GAL clump linear diameters, estimated at 250 μm, versus distances (blue: protostellar; red: pre-stellar; green: starless unbound). Different background levels of grey indicate size ranges corresponding to different object typologies (see text). The upper and lower dashed lines represent an angular size of 50 and 10 arcsec, respectively. Right-hand panel: distribution of source diameters for protostellar, pre-stellar and starless unbound sources. Line and background colours are the same as in the left-hand panel.

protostellar cases, we generally should not expect to observe the formation process of a single protostar, but rather of a protocluster.

We note that the histograms in Fig. 4, right-hand panel, should not be taken as a coherent size distribution of our source sample, due to the underlying spread in distance. It is not possible therefore to make global comparisons between the different classes as, for example, in Giannini et al. (2012), who considered objects from a single region, all located at the same heliocentric distance. The same consideration applies to the distribution of other distance-dependent quantities.

6.2 Dust temperature

The distributions of grey-body temperatures of the sources are shown in Fig. 5. As already found by Giannini et al. (2012), Elia et al. (2013), Giannetti et al. (2013) and Veneziani et al. (2017) through Hi-GAL observations, but also by Olmi et al. (2009) through BLAST observations, the distributions of pre-stellar and protostellar sources show some relevant differences, the latter being found towards warmer temperatures with respect to the former. A quantitative argument is represented by the average values $\bar{T}_{\rm pre} = 12.0$ K and $\bar{T}_{\rm prt} = 16.0$ K for pre-stellar and protostellar sources, and the median values $\tilde{T}_{\rm pre} = 11.7$ K and $\tilde{T}_{\rm prt} = 15.1$ K, respectively.

Furthermore, both the temperature distributions seem quite asymmetric, with a prominent high-temperature tail. This can be seen by means of the skewness indicator (defined as $\gamma = \mu_3/\sigma^3$, where μ_3 is the third central moment and σ is the standard deviation) of the two distributions: $\gamma_{\rm pre} = 1.06$ and $\gamma_{\rm prt} = 1.40$, respectively. The positive skew, in this case, indicates that the right-hand tail is longer ($\gamma = 0$ for a normal distribution), and quantifies that. On the other hand, the pre-stellar distribution appears more peaked than the protostellar one. The kurtosis of a distribution, defined as $\delta = \mu_4/\sigma^4$ (where μ_4 is the fourth central moment), is useful to quantify the level of peakedness (for a normal distribution, $\delta = 3$). In these two cases, the kurtosis values are found to be quite different for the two distributions ($\delta_{\rm pre} = 3.67$ and $\delta_{\rm prt} = 3.04$, respectively). Finally, we also plot the cumulative distributions of the temperatures, which is another way to highlight the behaviours examined so far. We find

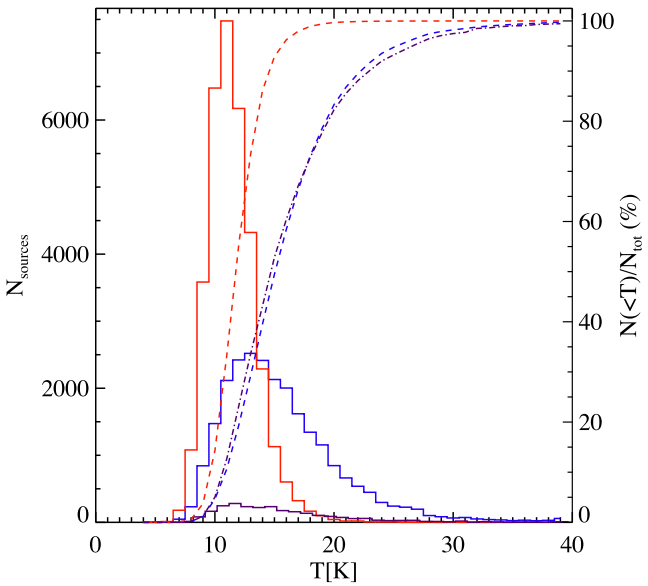

Figure 5. Grey-body temperature distributions for the pre-stellar (red histogram) and protostellar (blue histogram) sources considered for science analysis in this paper. Cumulative curves of the same distributions are also plotted as dashed lines (and the same colours), according to the *y*-axis on the right-hand side of the plot. Finally, the temperature distribution of the sub-sample of MIR-dark protostellar sources is plotted in dark purple, and the corresponding cumulative as a dot–dashed dark-purple line.

that 99 per cent of the pre-stellar (protostellar) sources have dust temperatures lower than 18.1 K (33.1 K), and the temperature range widths required to go from 1 per cent to 99 per cent levels are 9.9 and 24.2 K, respectively.

The differences found between the two distributions are even more meaningful from the point of view of the separation between the two classes of sources, if one keeps in mind that the temperature is estimated from data at wavelengths longer than 160 μm, hence independently of the existence of a measurement at 70 μm, which discriminates between protostellar and starless sources in our case.

These findings can be regarded from the evolutionary point of view: While pre-stellar sources represent the very early stage (or 'zero' stage) of star formation and, as such, are characterized by very similar temperatures, protostellar sources are increasingly warmer as the star formation progresses in their interior (e.g. Battersby et al. 2010; Svoboda et al. 2016), so that the spanned temperature range is larger and skewed towards higher values. A prominent high-temperature tail should be regarded, in this sense, as a signature of a more evolved stage of star formation activity.

To corroborate this view, we consider the temperatures of the sub-sample of protostellar sources of our catalogue lacking a detection in the MIR (i.e. at 21 and/or 22 and/or 24 μm, hereafter MIR-dark sources, as opposed to MIR-bright), whose distribution is also shown in Fig. 5. They represent 10 per cent of the total protostellar sources (therefore dominated by MIR-bright cases). The average and median temperature for this class of objects are $\bar{T}_{\rm Md} = 16.0$ K and $\tilde{T}_{\rm Md} = 14.8$ K, respectively, i.e. halfway between the values found for pre-stellar sources and those for the whole sample of protostellar ones, which is dominated by MIR-bright sources.

The reader should be aware that the dust temperature discussed here is derived simply from the grey-body fit of the SED at $\lambda \geq 160$ μm and represents an estimate of the average temperature of the cold dust in the clump. Using line tracers, it is possible to probe the kinetic temperature of warmer environments, such as the inner part of protostellar clumps, which is typically warmer ($T >$ 20 K, e.g. Molinari et al. 2016b; Svoboda et al. 2016) than the median temperature found here for this class of sources. Despite this, as seen in this section, the grey-body temperature can help to infer the source evolutionary stage, and turns out to be particularly efficient in combination with other parameters, as further discussed in Section 7.

6.2.1 Herschel *colours and temperature*

The availability of dust temperatures derived from grey-body fits makes it possible to directly compare with *Herschel* colours (cf. Elia et al. 2010; Spezzi et al. 2013), to ascertain which ones are better representative of the temperature. In Fig. 6, the source temperature is plotted versus the 10 possible colour pairs that can be obtained by combining the five *Herschel* bands (for each combination, only sources detected at both wavelengths are displayed). We designate as colour the decimal logarithm of the ratio of fluxes at two different wavelengths. Since the 70-μm band is not involved in the temperature determination, the colours built from it [plots (a)–(d)] do not show any tight correlation with temperature, while for the remaining six colours such correlation appears more evident, especially for those colours involving the 160-μm band. The best combination of spread of colour values (which decreases the level of temperature degeneracy, mostly at low temperatures) and agreement with the analytic behaviour expected for a grey body is found for colours involving the flux at 160 μm [panels (e)–(g)]. In particular, for the F_{500}/F_{160} colour, the grey-body curve has the shallowest slope, so that we propose this colour as the most suitable diagnostic of the average temperature in the absence of a complete grey-body fit. For the case of SPIRE-only sources, lacking a counterpart at 160 μm, only three colours are available, but their relation with dust temperature [cf. panels (h)–(j)] appears to be affected by a high degree of degeneracy, making these colours unreliable temperature indicators.

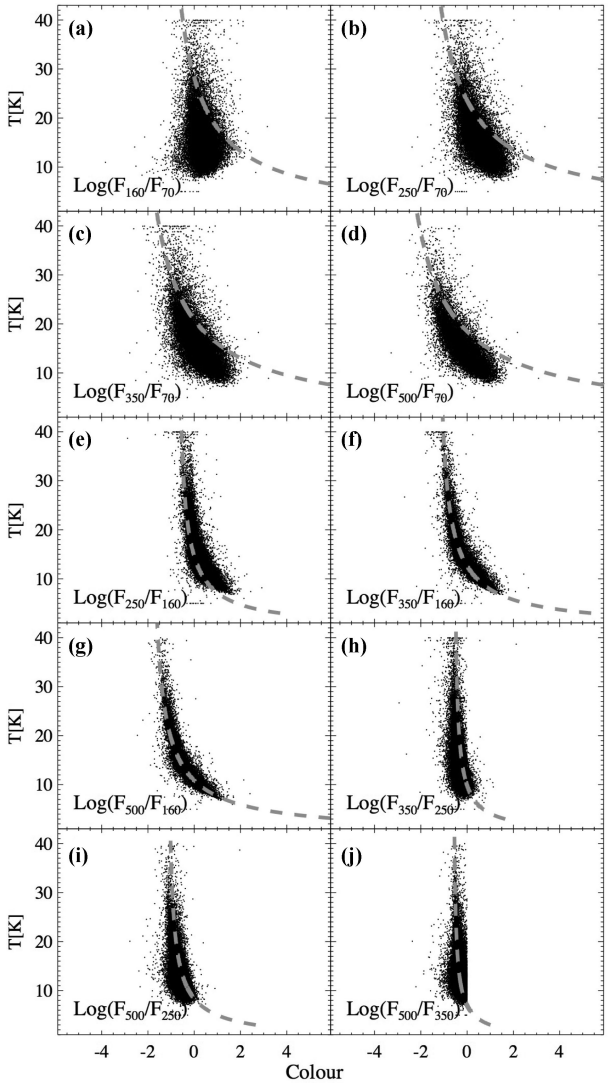

Figure 6. Panels (a)–(j): plots of source temperature (as derived through the grey-body fit) versus all colours obtainable from possible pair combinations of the five Hi-GAL wavebands. Each plot is obtained using all sources provided with fluxes at the two involved wavelengths, specified at the bottom of the panel. The unnatural vertical cut of the point distribution in panel (j) is an artefact due to one of the filters adopted for source selection, ruling out sources with $F_{350} < F_{500}$ (rescaled fluxed are considered, see Section 3.1). The grey-dashed line represents the temperature of a grey body with $\beta = 2$.

6.3 Mass and surface density

Once source masses are obtained, it would be straightforward to show and analyse the resulting distribution (clump mass function, hereafter ClumpMF). However, since such discussion implies considerations about the clump mass–size relation and, somehow equivalently, the surface density, we postpone the analysis of the ClumpMF until the end of this section, after having dealt with those preparatory aspects.

A meaningful combination of source properties is represented by the mass M versus radius r diagram, which has been shown to be a powerful tool for investigating the gravitational stability of *Herschel* compact sources, and their potential ability to form massive stars (André et al. 2010; Giannini et al. 2012; Elia et al. 2013). In both cases, in fact, requirements expressed in terms of surface density threshold can be translated into a simple mass–radius relation. Fig. 7

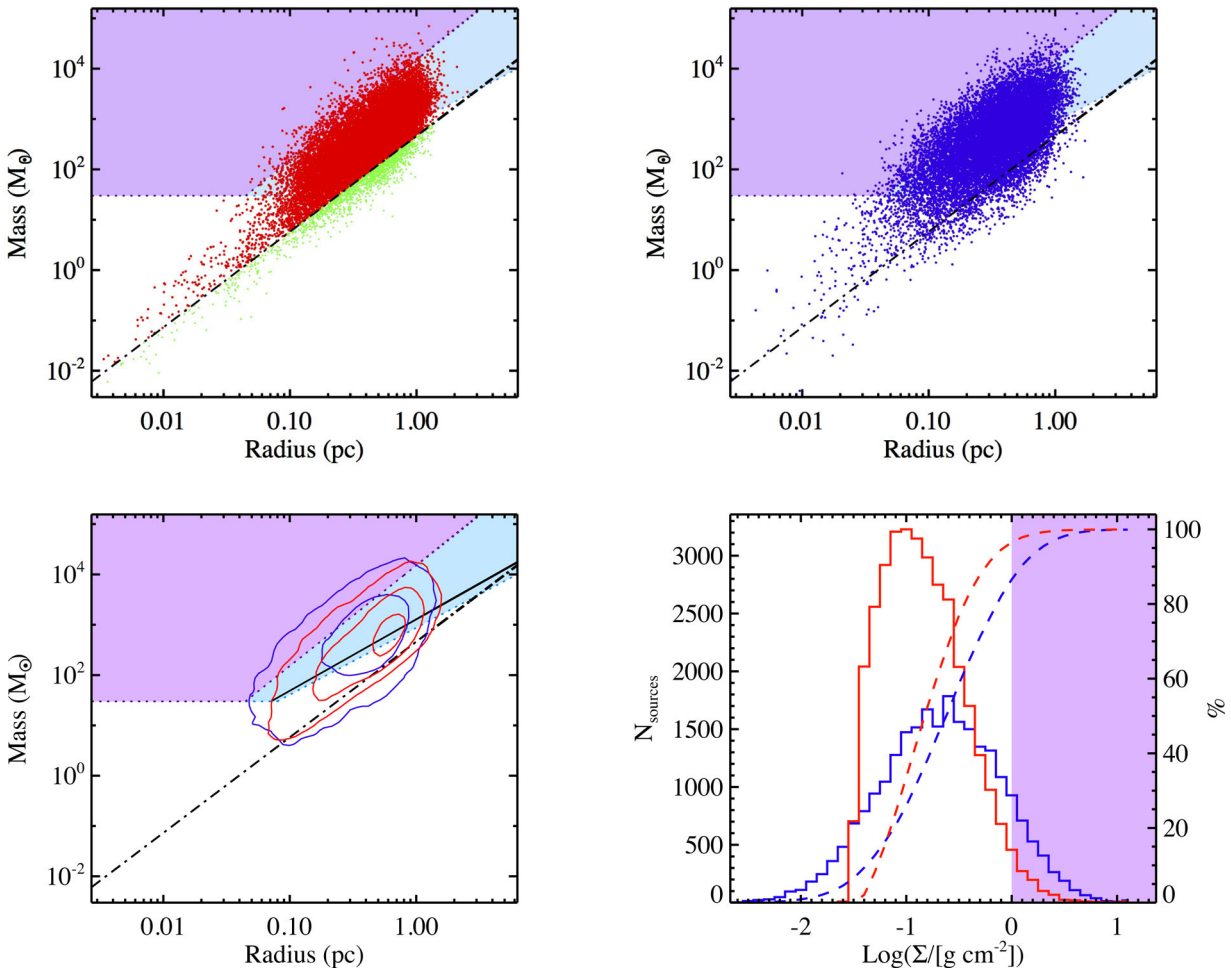

Figure 7. Top left-hand panel: mass versus radius plot for starless sources. Pre-stellar (red) and starless (green) sources are separated by the line $M(r) = 460\,M_{\odot}(r/pc)^{1.9}$ (Larson 1981) (dot–dashed black line) (see Section 3.5). The areas of the mass–radius plane corresponding to combinations fulfilling the Kauffmann & Pillai (2010) and Krumholz & McKee (2008) thresholds for compatibility with high-mass star formation are filled with light blue and purple, respectively, the latter being contained in the former, and both delimited by a darker dotted line. Notice that adopting a lower limit of $10\,M_{\odot}$ for the definition of a massive star, and a star formation efficiency factor of 1/3 for the core-to-star mass transfer as in Elia et al. (2013), these zones cannot extend below $30\,M_{\odot}$. Top right-hand panel: the same as in top left-hand panel, but for protostellar sources. Bottom left-hand panel: source density isocontours representing the pre-stellar and protostellar distributions displayed in the two upper panels of this figure. Densities have been computed by subdividing the area of the plot in a grid of 70 × 70 cells; once the global maxima for both distributions have been found, the plotted contours represent the 2 per cent, 20 per cent and 70 per cent of the largest of those two peak values, so that the considered levels correspond to the same values for both distributions, to be directly comparable. The black solid line crossing the bottom part of the light-blue area represents the threshold of Baldeschi et al. (2017). Bottom right-hand panel: surface density distributions (solid histograms) for pre-stellar (red) and protostellar (blue) sources. Because surface density is a distance-independent quantity, all sources (with and without distance estimates) are taken into account to build these distributions. The cumulative curves are plotted with dashed lines, normalized to the *y*-axis scale on the right-hand side. The zone corresponding to densities surpassing the Krumholz & McKee (2008) threshold is filled with purple colour.

shows the mass versus radius distribution for the sources analysed in this study. In the top left-hand panel, the starless sources are shown, while, to avoid confusion, the protostellar ones are reported in the top right-hand panel: Larson's relation mentioned in Section 3.5 is plotted to separate the starless bound (pre-stellar) and unbound sources.

From this plot, it is possible to determine if a given source satisfies the condition for massive star formation to occur, where such condition is expressed as surface density, Σ, threshold. Krumholz & McKee (2008) established a critical value of $\Sigma_{crit} = 1$ g cm^{-2} based on theoretical arguments. However, López-Sepulcre, Cesaroni & Walmsley (2010) and Butler & Tan (2012), based on observational evidence, suggest the less severe values of $\Sigma_{crit} = 0.3$ and 0.2 g cm^{-2}, respectively. Also, Kauffmann & Pillai (2010), based on empirical arguments, propose the threshold $M(r) > 870\,M_{\odot}(r/pc)^{1.33}$ as a minimum condition for massive star formation. Finally, the recent analysis by Baldeschi et al. (2017) of the distance bias affecting the source classification according to the two aforementioned thresholds produced the further criterion $M(r) > 1282\,M_{\odot}(r/pc)^{1.42}$. In the upper side, we represent the most (Krumholz & McKee 2008) and the least (Kauffmann & Pillai 2010) demanding thresholds, respectively, to allow comparison with the behaviour of our catalogue sources.

As reported in Table 2, a remarkable fraction of sources appear to be compatible with massive star formation based on the three thresholds (defined as Σ_{KM}, Σ_{B} and Σ_{KP}, respectively), especially the last. This is further highlighted by the bottom left-hand panel of Fig. 7, which summarizes the previous two panels reporting the

Table 2. Hi-GAL sources with the mass–radius relation compatible with massive star formation according to the surface density thresholds Σ_{KP}, Σ_B and Σ_{KM} (see text).

	$\Sigma > \Sigma_{KP}$		$\Sigma > \Sigma_B$		$\Sigma > \Sigma_{KM}$	
	Counts	Per cent	Counts	Per cent	Counts	Per cent
Protostellar	11 210	71.3	10 012	63.7	2062	13.1
Pre-stellar	12 431	64.8	9973	52.0	546	2.8

source densities for both the pre-stellar and the protostellar source populations. The peak of the protostellar source concentration lies well inside the area delineated by the Kauffmann & Pillai (2010) relation, while the pre-stellar distribution peaks at smaller densities. Rigorously speaking, however, such considerations on the initial conditions for star formation should be applied only to the pre-stellar clumps, since in the protostellar ones part of the initial clump mass has already been transferred on to the forming star(s) or dissipated under the action of stellar radiation pressure or through jet ejection. In any case, the presence of a significant number of very dense pre-stellar sources translates into an interestingly large sample of targets for subsequent study of the initial conditions for massive star formation throughout the Galactic plane (see Section 8.1). For such sources, due to contamination between the two classes described in Section 3.5, a further and deeper analysis is requested to ascertain their real starless status, independently of the lack of a *Herschel* detection at 70 μm.

Notice that the fractions corresponding to the threshold of Kauffmann & Pillai (2010) reported in Table 2 appear remarkably lower than the quantity estimated by Wienen et al. (2015) for the ATLASGAL catalogue, i.e. 92 per cent. This discrepancy cannot be explained simply by the better sensitivity of Hi-GAL: Taking the sensitivity curve in the mass versus radius of Wienen et al. (2015, their fig. 23), we find that the majority of our sources lie above that curve. The main reason, instead, resides in the analytic form itself of the adopted threshold. As mentioned above, Baldeschi et al. (2017) show that, even in the presence of dilution effects due to distance, sources in the mass versus radius plot are found to follow a slope steeper than the exponent 1.33, so that large physical radii, typically associated with sources observed at very far distances, correspond to masses larger than the Kauffmann & Pillai (2010) power law. This is not particularly evident in our Fig. 7 since the largest probed radii are around 1 pc, and the large spread of temperatures makes the plot quite scattered. Instead, fig. 23 of Wienen et al. (2015) contains a narrower distribution of points (since masses were derived in correspondence to only two temperatures, both higher than 20 K), extending up to $r \simeq 6$ pc: At $r \gtrsim 1$ pc, almost the totality of sources satisfy the Kauffmann & Pillai (2010) relation. Clearly, another contribution to this discrepancy can be given by the scatter produced by possible inaccurate assignment of the far kinematic distance solution in cases of unsolved ambiguity (see Section 3.4).

The information contained in the mass–radius plot can be rearranged in a histogram of the surface density[5] Σ such as that in Fig. 7, bottom right-hand panel. The pre-stellar source distribution presents a sharp artificial drop at small densities due to the removal of the unbound sources, which is operated along $M \propto r^{1.9}$, i.e. at an almost constant surface density ($M \propto r^2$). Instead, despite the considered pre-stellar population being globally more numerous than the protostellar one, at high densities ($\Sigma \gtrsim 1$ g cm^{-2}) the latter prevails over the former. The protostellar distribution, in general, appears shifted towards larger densities, compared with the pre-stellar one, as can be seen in the different behaviour of the cumulative curves, also shown in the figure. This evidence is in agreement with the result of He et al. (2015), based on the MALT90 survey. Further evolutionary implications will be discussed in Section 7.3.

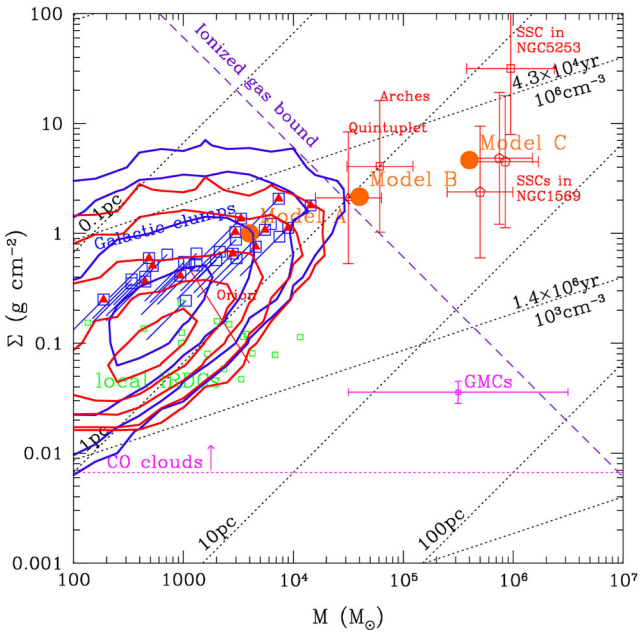

Figure 8. Plot of surface density versus mass of Tan (2005, his fig. 1), with overplotted number density contours of pre-stellar (red) and protostellar (blue) sources of our catalogue. The source density is computed in bins of 0.2 in decimal logarithm, and contour levels are 5, 20, 100, 250 and 500 sources per bin. The horizontal cut at lowest densities for red contours is due to the removal of starless unbound sources. The diagonal dotted lines represent the loci of given radii and number densities (and corresponding free-fall times). Typical ranges for molecular clouds are indicated with magenta lines, while the condition for the ionized gas to remain bound is indicated by the blue dashed line. Finally, locations for a selection of IRDCs (green squares), dense star-forming clumps (blue squares), massive clusters (red symbols) and cluster models of Tan (2005) (filled orange circles) are shown. Additional information reported in this diagram is provided in Tan (2005) and Molinari et al. (2014, their fig. 11).

We note, as discussed in Section 6.1, that the compact sources we consider may correspond, depending on their heliocentric distance, to large and in-homogeneous clumps with a complex underlying morphology not resolved with *Herschel*. On one hand, this implies that the global properties we assign to each source do not remain necessarily constant throughout its internal structure; thus, a source fulfilling a given threshold on the surface density might, in fact, contain sub-critical regions. On the other hand, in a source with a global sub-critical density, super-critical portions might actually be present, leading to misclassifications; for this reason, the numbers reported in Table 2 should be taken as lower limits.

We use the collected information about source masses and surface densities to place them in the Σ versus M plot of Tan (2005), in which different classes of structures populate different regions. Our Fig. 8 is analogous to fig. 11 of Molinari et al. (2014), but the 'temporary' data set used for that plot is replaced here with the

[5] It is notable that if a grey body is fitted to an SED through equation (1), the surface density is proportional to τ_{ref} (equation (3)), which is, in turn, proportional to $\lambda_0^{-\beta}$ (equation 2), with $\beta = 2$ in this paper. This implies that a description based on the surface analysis is, for such sources, equivalent to that based on the λ_0 parameter.

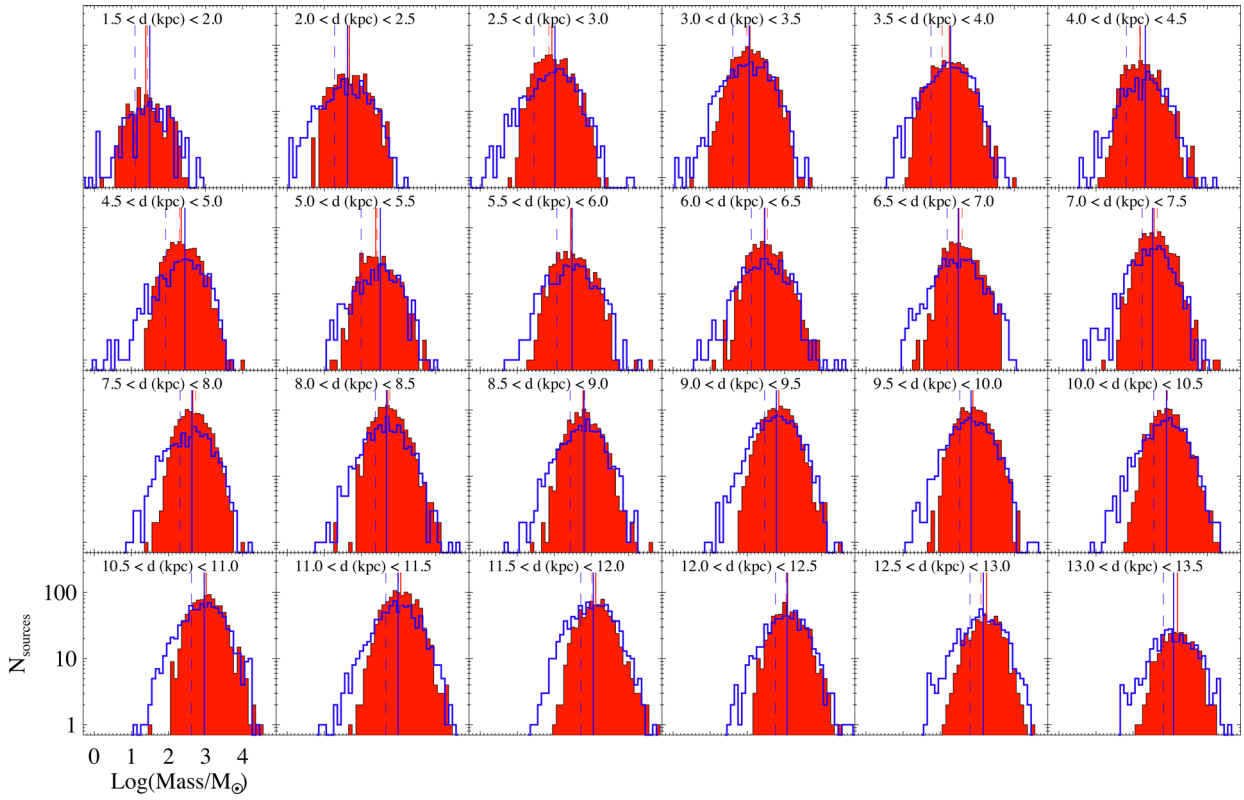

Figure 9. Clump mass function for pre-stellar (red filled histogram) and protostellar (blue histogram) sources, obtained in 0.5-kpc-wide heliocentric distance ranges. Each panel corresponds to the range that is reported in the upper part. The dashed red and blue lines indicate the completeness limits, and the solid red and blue vertical lines indicate the lower limit used to fit the curves in Fig. 10, for the pre-stellar and protostellar cases, respectively.

values from the final Hi-GAL physical catalogue. The Hi-GAL sources are found to lie in the regions quoted by Tan (2005) for Galactic clumps and local IRDCs. In the upper right-hand part of their distribution, they graze the line representing the condition for ionized gas to remain bound. This plot summarizes the nature of the sources in our catalogue: clumps spanning a wide range of mass/surface density combinations, with many of them found to be compatible with the formation of massive Galactic clusters.

6.4 The ClumpMF

The ClumpMF is an observable that has been extensively studied for understanding the connection between star formation and parental cloud conditions. Although formulations are quite similar, the ClumpMF should not be confused with the core mass function (hereafter CoreMF), typically studied in nearby star-forming regions ($d \lesssim 1$ kpc). Differences between these two distributions will be discussed later in this section.

Large IR/sub-mm surveys generated numerous estimates of the ClumpMF (e.g. Reid & Wilson 2005, 2006; Eden et al. 2012; Tackenberg et al. 2012; Urquhart et al. 2014a; Moore et al. 2015). Likewise, data from Hi-GAL have been used for building the ClumpMF in selected regions of the Galactic plane (Elia et al. 2013; Olmi et al. 2013).

Building the mass function of a given sample of sources (Hi-GAL clumps in the present case) requires a sample to be defined in a consistent way. A clump mass function built from a sample of sources spanning a wide range of distances (as in our case) would be meaningless, since at large distances low-mass objects might not be detected or might be confused within larger, unresolved structures (see Appendix C); therefore, it makes little sense to discuss it. Therefore, we first subdivide our source sample into bins of heliocentric distance, and then build the corresponding mass functions separately. In addition, as pointed out, e.g. by Elia et al. (2013), it is more appropriate to build separate ClumpMFs for pre-stellar and protostellar sources. Strictly speaking, only the mass distributions of pre-stellar sources are intrinsically coherent, as the mass of the protostellar sources does not represent the initial core mass, but rather a lower limit, which depends on the current evolutionary stage of each source.

In Fig. 9, the clump mass functions are shown. They have been calculated using sources provided with a distance estimate, from 1.5 to 13.5 kpc in distance bins of 0.5 kpc, in logarithmic mass bins, and separately for pre-stellar and protostellar clumps.

It can be immediately noticed that, for any distance range, the protostellar ClumpMF is wider than the pre-stellar one, so that a deficit of pre-stellar clumps with respect to protostellar ones is seen both at lowest and highest masses in each bin of distance. The former effect is mostly due to sensitivity: Sure enough, thanks to higher temperature, a protostellar source can be detected more easily than a pre-stellar source of the same mass. For example, according to equation (C2) in Appendix C2, applied to a given mass, the flux of a source at $T = 15$ K (i.e. $\sim\bar{T}_{\rm prt}$) is nearly twice that of a source at $T = 12$ K (i.e. $\sim\bar{T}_{\rm pre}$ K). The latter effect can in part be explained by the pre-stellar/protostellar possible blending and misclassification at increasing distance, discussed in Appendix C,

which leads to artificially overestimating the fraction of protostellar sources. However, from the quantitative point of view, this effect seems not sufficient to entirely account for the complete lack of pre-stellar sources as massive as the most massive protostellar ones. A further contribution is surely given as well by the more rapid evolution of massive pre-stellar sources towards the protostellar status (see e.g. Motte et al. 2010b; Ragan et al. 2013). To correctly examine this point, sub-samples that are consistent in terms of heliocentric distance must be isolated, as we do, in fact, in building Fig. 9. Indeed, the structure of two clumps of, say, 200 $M_\odot$ detected at $d = 10$ and 2 kpc would be strongly different: The former would be expected to be likely composed of an underlying population of low-mass cores (Baldeschi et al. 2017), whereas the second, being better resolved by *Herschel*, would be denser and less fragmented than the former, therefore representing a more reliable candidate for hosting massive star formation and having shorter evolutionary time-scales. This scenario is confirmed in most panels of Fig. 9, where, given a range of heliocentric distances, a lack of pre-stellar clumps with respect to the protostellar ones is generally found in the bins corresponding to the highest masses present. Importantly, this indicates that it is not sufficient to simply claim that massive clumps have very short lifetimes (Ginsburg et al. 2012; Tackenberg et al. 2012; Csengeri et al. 2014): Indeed, a large clump mass might also result from an associated large heliocentric distance, which implies multiple source confusion and inclusion of diffuse emission contaminating source photometry (see also Baldeschi et al. 2017). In this respect, clump density has to be taken into account as well, since only high densities ensure conditions for massive star formation and therefore for a faster evolution of a clump.

The differences observed between pre-stellar and protostellar ClumpMFs are expected to be reflected on the slope of the power-law fit of the high-mass end of these distributions, i.e. the usual way to extract information from the ClumpMF and compare it with the stellar initial mass function. The estimate of this slope is generally plagued by uncertainties due to an arbitrary choice of mass bins and of the lower limit of the range to be involved in the fit. Olmi et al. (2013) have presented an efficient way, based on the application of Bayesian statistics, to overcome such issues. Here we adopt a simpler approach:

(i) The slope of the ClumpMF is derived indirectly, by estimating the slope of the corresponding cumulative function defined, as a function of M, as the fraction of sources having mass larger than M. If a ClumpMF is calculated in logarithmic bins and is expected to have a power-law behaviour above a certain value $M_{\rm fit}$, so that $\mathrm{d}N(M)/\mathrm{dlog}_{10}(M) \propto M^{\alpha}$, then the corresponding cumulative function (hereafter CClumpMF) has the same exponent α (e.g. Shirley et al. 2003), and the estimate of such slope is independent of the bin used to sample the ClumpMF.

(ii) The portion of the ClumpMF used in the fit should be delimited at the bottom by the turnover point of the ClumpMF $M_{\rm peak}$, namely the peak of a lognormal best fit (Chabrier 2003). One has to ensure that this mass limit is larger than the completeness limit of the distribution. The estimation of the mass completeness limit $M_{\rm compl}$ is not trivial in our case, since multiple bands and variable temperature and distance concur in the mass determination, as discussed in Appendix C2. Equation (C2) can be applied to compute the limit, assuming the central distance of each bin, the median temperatures of pre-stellar and protostellar sources, and a flux completeness limit at 350 μm, $F_{\rm compl,\,350}$, as estimated by Molinari et al. (2016a). This completeness limit, quoted by these authors as a function of Galactic longitude (their fig. 9), reaches a maximum of 13.08 Jy around $\ell = 0^\circ$ (a region that does not provide sources for this analysis, given the lack of distance information), and a minimum of 0.65 Jy in the eastmost tile of the first quadrant. In intermediate regions, which provide the biggest contribution in building our ClumpMFs, in general $F_{\rm compl,\,350} \lesssim 4$ Jy, which we adopt here. In a few cases in which $M_{\rm peak} < M_{\rm compl}$, the latter is taken as the lower limit of the fit range.

In each panel of Fig. 9, the peak of the ClumpMF and the completeness limit are shown for both pre-stellar and protostellar distributions, while in Fig. 10 the corresponding CClumpMFs are shown. The slopes obtained through the power-law fit range from −0.88 to −1.46 for the pre-stellar sources and from −0.88 to −1.23 for the protostellar ones. As expected from the discussion above, slopes of protostellar ClumpMFs are systematically shallower than the pre-stellar ones (cf. also di Francesco et al. 2010), being the former strongly biased by the lack of clumps at the highest mass bins compared with protostellar ones. In some cases, slopes of pre-stellar ClumpMFs can take values even steeper than the stellar initial mass function (IMF, $\alpha_{\rm IMF} = -1.35$, Salpeter 1955), as testified also by Tackenberg et al. (2012). In contrast, the slopes of protostellar ClumpMFs always remain shallower than $\alpha_{\rm IMF}$, thus confirming the typical expectation for a generic mass distribution of unresolved clumps (Ragan, Bergin & Gutermuth 2009; di Francesco et al. 2010; Peretto & Fuller 2010; Eden et al. 2012; Pekruhl et al. 2013), while for the CoreMF a slope compatible with $\alpha_{\rm IMF}$ is typically found (e.g. Giannini et al. 2012; Polychroni et al. 2013; Könyves et al. 2015). On one hand, this confirms, across a wide range of heliocentric distances and based on unprecedentedly large statistics, a behaviour of the ClumpMF already known from literature. On the other hand, we caution the reader that (i) the behaviour of the pre-stellar ClumpMFs has to be better investigated in the future (for example, by means of higher resolution observations of high-density pre-stellar cores, as suggested by Fig. 8), and (ii) the ClumpMFs discussed here are obtained regardless of Galactic longitude, but simply grouping sources by heliocentric distance. More focused studies on selected ranges of Galactic longitude will enable the generation of mass distributions for even more coherent data sets, while also making it possible to explore environmental variations when looking at, e.g. individual spiral arms, tangent points and star-forming complexes. This, in turn, will allow an assessment of similarities and differences among different Galactic locations.

Finally, ClumpMF slopes at different distances allow us to test the possible effects of gradual lack of spatial resolution on the ClumpMF slope. This problem has already been investigated by Reid et al. (2010) by means of simulations. Despite a depletion of sources in low-mass bins is expected at increasing heliocentric distance, together with an increase in high-mass bins due to blending, Reid et al. (2010) did not find a progressive shallowing of the ClumpMF. Here we can confirm, based on observational arguments, that the slopes reported across various panels of Fig. 10 do not show any particular trend with distance. Therefore, whereas a clear distinction is found between the mass spectrum of cores (typically resolved by *Herschel* if located at $d \lesssim 1$ kpc, Giannini et al. 2012; Baldeschi et al. 2017), and that of clumps, with the former being steeper than the latter, no further systematic steepening is found for clumps observed at increasing distances. This might also be regarded as indirect evidence of the self-similarity of molecular clouds (Stutzki et al. 1998; Smith, Clark & Bonnell 2008; Elia et al. 2014) over the investigated range of physical scales, which, in this case, is the range of the linear sizes of compact sources located between $d = 1.5$ and 13.5 kpc.

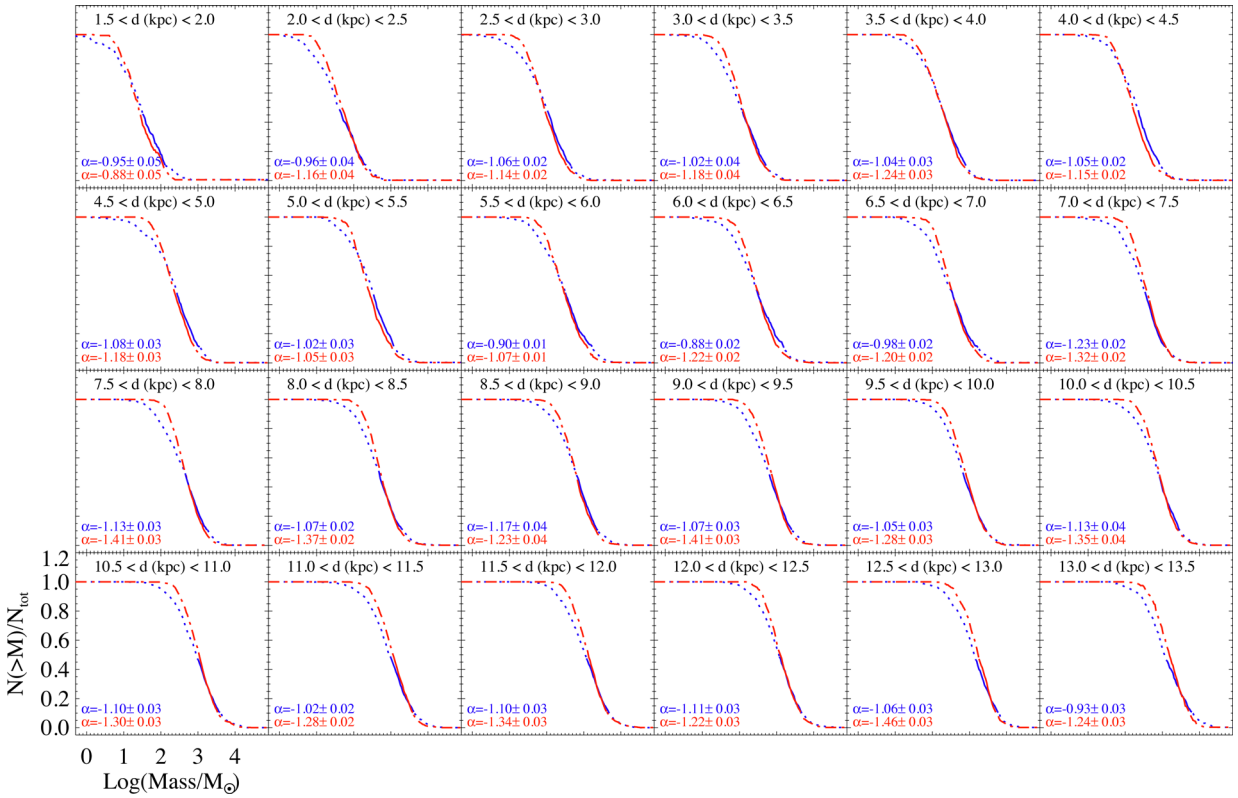

Figure 10. CClumpMFs for pre-stellar (red dot–dashed line) and protostellar (blue dotted line) sources, obtained in the same distance ranges as used for Fig. 9. The power-law (linear in bi-logarithmic scale) portion is highlighted with solid lines, and the corresponding slope is reported in the panel with the same colour coding.

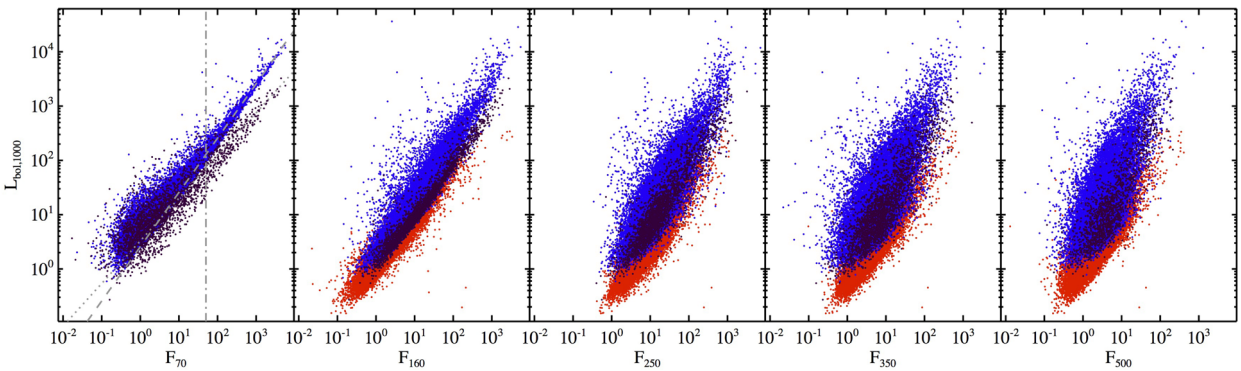

Figure 11. From the left- to right-hand side: source bolometric luminosity rescaled to the virtual distance $d_v = 1$ kpc versus *Herschel* monochromatic flux at 70, 160, 250, 350 and 500 μm, respectively. For clarity purposes, symbols of sources belonging to the same evolutionary class have been plotted all together: protostellar sources (blue) are overlaid on the pre-stellar sources (red), and MIR-dark protostellar sources (dark purple) are overlaid, in turn, on protostellar sources. In the leftmost panel (corresponding to the 70-μm case), the power-law fit is shown for sources with large fluxes ($F_{70} \gtrsim 50$ Jy, grey dot–dashed vertical line), separately for the MIR-bright sub-sample (dashed line) and for the MIR-dark one (dotted line).

6.5 Bolometric luminosity and temperature

Before discussing the use of bolometric luminosity, estimated as described in Section 4, to infer the evolutionary stage of a clump, we show how this quantity correlates with monochromatic *Herschel* fluxes. Indeed, Dunham et al. (2008) already suggested the *Spitzer* flux at 70 μm as a reliable proxy of the total protostellar core luminosity, and Ragan et al. (2012) confirmed an evident correlation between fluxes measured at all the three PACS bands (70, 100 and 160 μm) and bolometric luminosity of *Herschel* clumps. In the five panels of Fig. 11, the bolometric luminosity, conveniently rescaled to a common virtual distance $d_v = 1$ kpc, is plotted versus the *Herschel* flux at different bands. The tightest correlation is found at PACS wavelengths, especially at 70 μm (left-hand panel), where an overall power-law behaviour for MIR-bright sources can be identified at large fluxes ($F_{70} \gtrsim 50$ Jy). At lower fluxes, one observes a departure of luminosity (observed also in Ragan et al. 2012) from the trend, which in this case represents the lower limit of the distribution. Interestingly, a secondary trend, similar to the main one but at a lower luminosity level and essentially due to MIR-dark protostellar sources, is observed: $F_{70} \gtrsim 50$ Jy. The power-law best fit yields the expressions $L_{\rm bol,MIR\text{-}bright}[L_\odot] = 2.56 F_{70}\,[\rm Jy]^{1.00}$

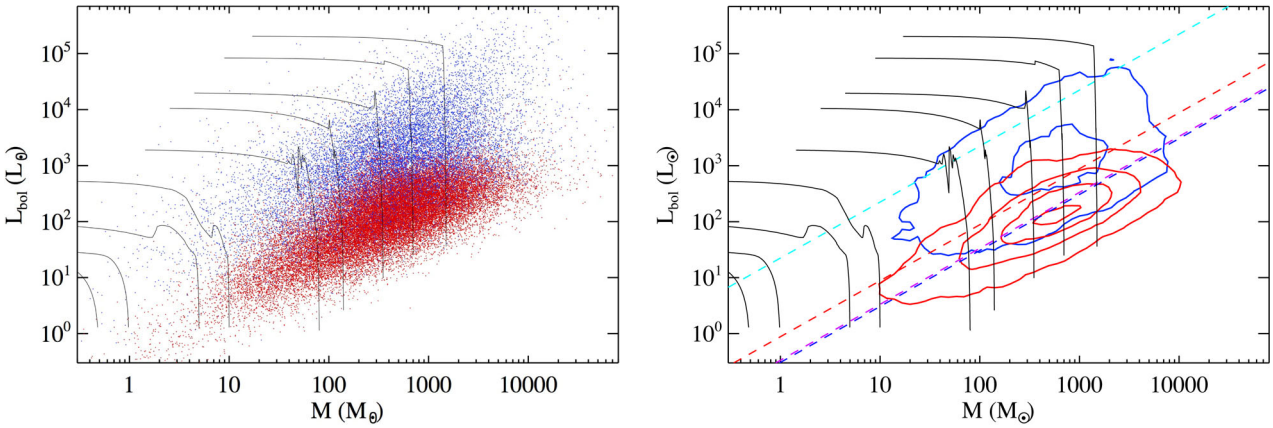

Figure 12. Left-hand panel: L_{bol} versus M_{env} plot for all the sources considered in this paper. The black lines represent evolutionary tracks from Molinari et al. (2008). Right-hand panel: the same as in the left-hand panel, but with source density contours plotted instead of single sources. Contours are determined as in the bottom left-hand panel of Fig. 7, using levels of 5 per cent, 25 per cent, 50 per cent and 75 per cent of the maximum density found in the plot. Dashed lines correspond to some relevant percentiles of the L_{bol}/M_{env} ratio for different source populations (cf. Fig. 13): In the area of the diagram below the red line, 90 per cent of pre-stellar sources are located, while above the blue, dark-purple and light-blue lines, 90 per cent of all protostellar, MIR-dark protostellar and H II-region-compatible sources are located.

(corresponding to linear behaviour, as in Ragan et al. 2012) and $L_{bol,MIR\text{-}dark}[L_\odot] = 3.29 F_{70}\,[Jy]^{0.79}$ for the two sub-samples in the considered range of fluxes, respectively.

The relation between bolometric luminosity and envelope mass is particularly interesting as an indicator of the evolutionary status of a core/clump. The L_{bol} versus M_{env} diagram is a widely used tool (Saraceno et al. 1996; André et al. 2008; Molinari et al. 2008; Giannini et al. 2012; Elia et al. 2013; Giannetti et al. 2013; Ragan et al. 2013) in which evolutionary tracks, essentially composed of an accretion phase and a clean-up phase (Molinari et al. 2008; Smith 2014), can be plotted and compared with data. In the earliest stages of star formation, as the protostar gains mass from the surrounding envelope, these tracks are nearly vertical, while, after the central star has reached the zero-age main sequence (ZAMS), they assume a nearly horizontal behaviour corresponding to dispersal of the residual clump material.

In Fig. 12, left-hand panel, we built the L_{bol} versus M_{env} plot using the bolometric luminosity obtained as described in Section 4, while the envelope mass is the source mass M we derived through the grey-body fit. For protostellar objects, M_{env} represents the residual mass of the parental clump/cloud still surrounding the embedded protostars, while for the starless sources it is the whole clump mass itself. Hereafter, we will adopt $M_{env} = M$. The right-hand panel of the figure clarifies, by means of density contours, how protostellar sources are spread in a large area corresponding to a variety of ages, encompassing even evolutionary stages closer to the transition between clump collapse and envelope dissolution (ZAMS). However, since the bolometric luminosities are computed starting from the MIR ($\sim$20 μm) or from longer wavelengths, while the most evolved Hi-GAL sources are expected to also have counterparts at shorter wavelengths (e.g. Li et al. 2012; Tapia et al. 2014; Strafella et al. 2015; Yun et al. 2015), it is likely that for a fraction of protostellar sources the evolutionary stage is underestimated, and the actual spread in age of this population is larger than represented here.

As better highlighted by source density contours displayed in the right-hand panel of Fig. 12, pre-stellar sources are generally confined in a relatively narrower region corresponding to the absence of collapse, or to the earliest clump collapse phases. This result can be compared with recent Hi-GAL works focused on smaller portions of the Galactic plane. In Veneziani et al. (2017), the clump populations at the tips of the Galactic bar, extracted from the entire catalogue presented here, show a similar behaviour. In contrast, a comparison with the analysis of a portion of the third Galactic quadrant of Elia et al. (2013), as well as the larger number of sources considered and the spread over heliocentric distances (resulting in a wider range of masses and luminosities), highlights two points. First, the barycentre of the mass distribution is located towards higher values as a consequence of larger source distances involved in our sample. Secondly, a higher degree of overlap is seen between the pre-stellar and protostellar source populations, the former being found, at $M > 10\,M_\odot$, to be overlapped with the accretion portion of the evolutionary tracks, also populated by the protostellar sources. This does not necessarily mean that in the outer Galaxy a clearer segregation of the pre-stellar versus protostellar clump populations is seen through this diagnostic tool (see also Giannini et al. 2012, for another example of analysis of an outer Galaxy region, namely Vela-C), since distance effects must also be taken into account. On average, the sources of Giannini et al. (2012) and Elia et al. (2013) are much closer ($d = 700$ pc and $d \lesssim 2200$ pc, respectively) than most sources of our sample, and larger distances might introduce ambiguities in the pre-stellar versus protostellar classification (see Appendix C). Further extension of the clump property analysis to other regions of the outer Galaxy (Merello et al., in preparation), and a systematic treatment of possible biases introduced by distance (Baldeschi et al. 2017), will make it possible to confirm this interpretation.

To express the relation between L_{bol} and M through a single indicator, one can use their ratio L_{bol}/M (cf. e.g. Ma, Tan & Barnes 2013; Molinari et al. 2016b),[6] which has the advantage of being a distance-independent observable, allowing the use of the evolutionary analysis for catalogue entries devoid of a distance estimate. Fig. 13 shows the histograms of this quantity for pre-stellar and protostellar Hi-GAL sources, separately. Also here it can be seen

[6] A comparison with the L_{bol}/M ratio found by other similar surveys is provided in Appendix D.

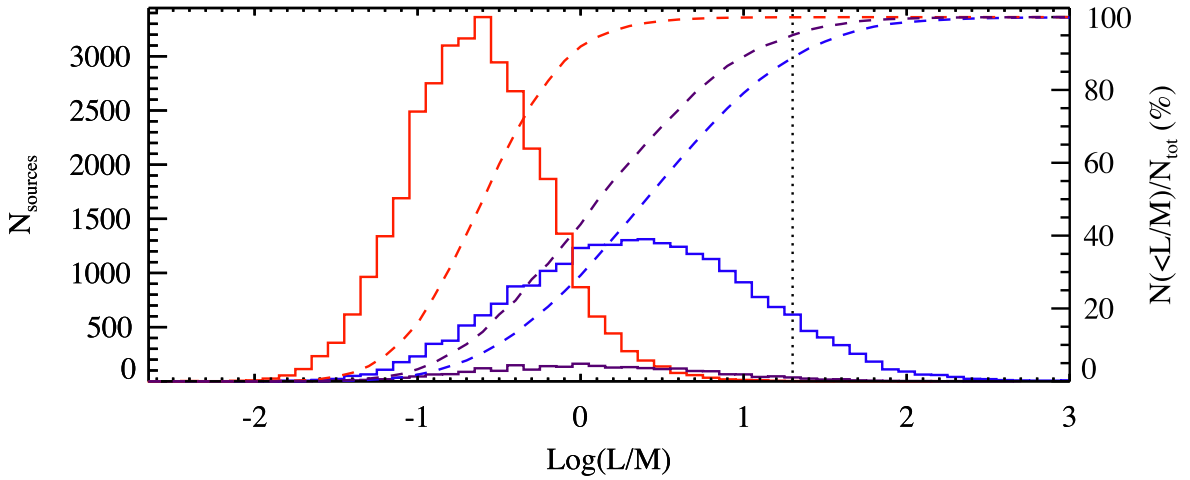

Figure 13. The same as in Fig. 5, but for the $L_{\rm bol}/M$ ratio. The vertical dotted line represents the peak of the distribution of Cesaroni et al. (2015) (see text).

that the distributions of $L_{\rm bol}/M$ ratios for pre-stellar and protostellar sources appear very different: In general, pre-stellar objects show a more confined distribution around 0.3 $L_\odot/M_\odot$, while protostellar sources are widely distributed with a peak around 2.5 $L_\odot/M_\odot$. A significant overlap of the two histograms is found in any case: Notice, for instance, that 90 per cent of pre-stellar sources are found at $L_{\rm bol}/M < 0.9\,L_\odot/M_\odot$, while 90 per cent of protostellar sources are found at $L_{\rm bol}/M > 0.3\,L_\odot/M_\odot$ (Fig. 12, right-hand panel).

The larger width of the protostellar source distribution suggests that they are transition objects in an evolutionary phase between pure (yet starless) collapse and 'naked' young stars without a dust envelope: The protostar(s) responsible for the increase in bolometric luminosity can still be embedded in a large cold dust envelope, responsible for keeping the mass of the entire protostellar clump high enough to reduce the $L_{\rm bol}/M$ ratio. Furthermore, one should keep in mind that conditions favourable to the formation of stars might be met only in a fraction of the entire volume of a distant protostellar clump. The observed $L_{\rm bol}/M$ ratio of a protostellar object is a single observable computed from the global emission of an envelope containing unresolved young stellar objects (YSOs) not necessarily coeval, but more generally at mixed stages of evolution (Yun et al. 2015).

From the analysis of the dust temperature distribution (Section 6.2), we could infer that MIR-dark protostellar sources are at an intermediate evolutionary stage between pre-stellar and MIR-bright protostellar sources. However, the $L_{\rm bol}/M$ metric indicates (see Fig. 13) that this population spans a wide range of values, instead of being confined to the tail of the overall protostellar distribution. The cumulative distribution is only slightly different from that of the overall protostellar sample, and very different from that of the pre-stellar sample. Furthermore, the 10 per cent percentile of this distribution (Fig. 12, right-hand panel) is indistinguishable from the same percentile computed for the protostellar population. In summary, the $L_{\rm bol}/M$ ratio for MIR-dark protostellar sources is not significantly different from that of the other protostellar sources.

To identify possible additional sub-classes within the protostellar population, the correlation with external evolutionary tracers can be used (as we intend to do in future papers based on this catalogue). For example, in the RMS survey (Lumsden et al. 2013), an effort has been made to identify massive YSOs and ultracompact H II regions by means of multiwavelength ancillary data, both photometric and spectroscopic (e.g. Urquhart et al. 2009, and references therein). Similarly, for Hi-GAL, Cesaroni et al. (2015) studied, in the longitude range $10^\circ < \ell < 65^\circ$, the counterparts of CORNISH (Hoare et al. 2012; Purcell et al. 2013) sources, treated as bona fide young H II regions, and distributed across the range $2 < L_{\rm bol}/M < 270\,L_\odot/M_\odot$. From the data of Cesaroni et al. (2015), we estimate the peak of this distribution to lie around $(L/M)_{\rm P} \equiv 22.4\,L_\odot/M_\odot$. At values larger than this peak, in principle, even more evolved sources are expected, so the fact that the distribution decreases beyond this peak is mostly due to completeness: Indeed the SED filtering we apply, mostly based on the availability of detections at 250 and 350 μm, causes the removal of a large number of evolved sources from our physical catalogue.

The locus corresponding to $(L/M)_{\rm P}$ is also reported in Fig. 12, right-hand panel, as a light-blue dashed line: If we compare it with a similar diagram in Molinari et al. (2008), we notice that their 'IR sources', namely the SEDs fitted with an embedded ZAMS envelope (many of which compatible with the presence of an ultracompact H II region), lie in the region of the diagram above this threshold.

Since our catalogue covers an area of the sky larger than that observed by the CORNISH survey to date, it would be useful to develop a *Herschel*-based method – verified by means of independent tracers – able to identify possible H II-region candidates in other parts of the Galactic plane, such as the the fourth quadrant. For this reason, the sources with $L_{\rm bol}/M \geq (L/M)_{\rm P}$ will henceforth be treated as 'H II-region candidates'.

Additional information can be obtained from the study of the source luminosity. For example, the $L_{\rm smm}/L_{\rm bol}$ ratio is a distance-independent evolutionary indicator frequently discussed in the study of the low-mass star formation. André, Ward-Thompson & Barsony (2000) characterized Class 0 objects (Andre, Ward-Thompson & Barsony 1993) through the ratio of their sub-mm luminosity, calculated for $\lambda \geq 350$ μm, to their bolometric luminosity, establishing a minimum threshold of 0.005 for identifying an object of this class. Subsequently, Maury et al. (2011) refined this value to 0.01, which, if one prefers to use the inverse of this ratio (as, e.g. Beuther et al. 2010, and in this paper), translates into the condition $L_{\rm bol}/L_{\rm smm} < 100$. Obviously, Class 0/I/II/III is meaningful only for single low-mass protostars, while in our study we address sources that do not correspond to single YSOs, and, furthermore, in a relevant fraction of cases, these might host massive star formation. Therefore, in our case, the $L_{\rm bol}/L_{\rm smm}$ ratio cannot be used to identify Class 0 sources (see also Fallscheer et al. 2013); rather, we can only safely state that

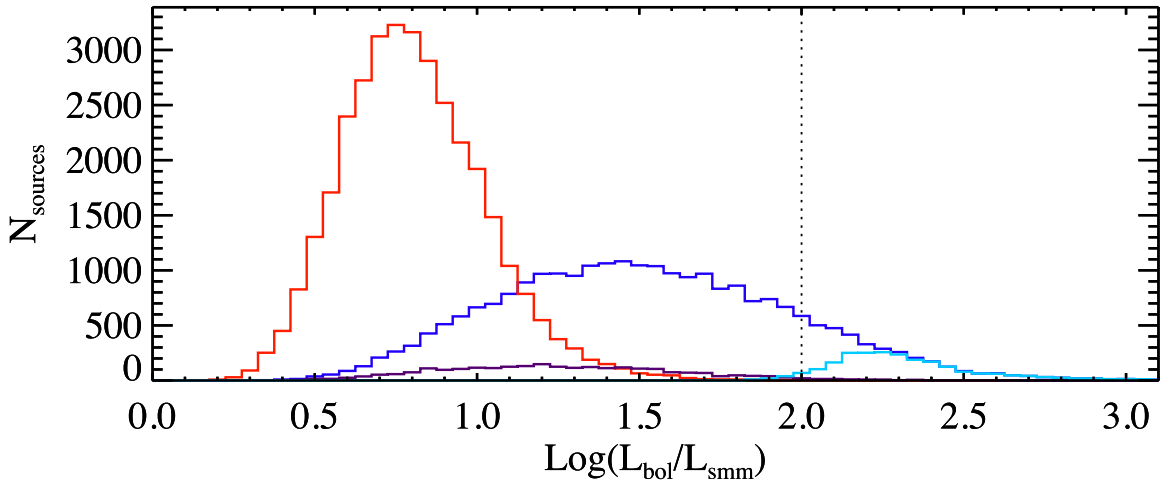

Figure 14. Distributions of $L_{\rm bol}/L_{\rm smm}$ ratio for science analysis in this paper: Pre-stellar and protostellar ones are represented with a red and blue histogram, while the MIR-dark and H II-region candidate sub-samples of the protostellar ones are represented with a dark-purple and a light-blue histogram, respectively. The dotted vertical line represents the threshold for identifying Class 0 YSOs in the low-mass regime of star formation (Maury et al. 2011).

sources whose SEDs have a significant contribution of emission at sub-millimetric wavelengths are at an early stage of star formation.

In Fig. 14, the distributions of $L_{\rm bol}/L_{\rm smm}$ for pre-stellar and protostellar sources are shown, again exhibiting a different behaviour of the two: The former (having about 99.96 per cent of sources below the critical value of 100) peaks at a value smaller than the latter, which, in turn, has only 86 per cent below the threshold. Since many of the sources of our catalogue belong to well-known star-forming regions where the presence of sources more evolved than Class 0 has been assessed, these results clearly indicate that an evolutionary classification based only on *Herschel* photometry (even extended to shorter wavelengths down to ∼20 μm) generally leads to a biased classification of most sources as Class 0 (or, more precisely, as their high-mass equivalents), as already pointed out by Giannini et al. (2012) and Elia et al. (2013). Looking in more detail at the two sub-classes of protostellar sources introduced above, the MIR-dark sources show a spread similar to that encountered in Fig. 13, while the H II-region candidates constitute the right-hand tail of the protostellar distribution, with most bins located above the threshold value of 100.

An even higher degree of segregation between pre-stellar and protostellar sources can be found in the bolometric temperature distribution shown in Fig. 15, being defined by Myers & Ladd (1993) as

$$T_{\rm bol} = 1.25 \times 10^{-11}\,{\rm K} \times \frac{\int_0^\infty \nu F_\nu {\rm d}\nu}{\int_0^\infty F_\nu {\rm d}\nu}\,. \qquad (5)$$

This diagnostic has been recently used by Strafella et al. (2015) by using Hi-GAL data, but building SEDs with a wider range of photometric data points, going from *Spitzer*-IRAC bands, which can lead to a shift of bolometric temperatures towards values in the range $T_{\rm bol} \sim$ 100–1000 K, much larger than those found here ($T_{\rm bol} \lesssim 100$ K). In fact, similarly to the $L_{\rm smm}/L_{\rm bol}$ ratio, bolometric temperatures cannot be used to infer the Class 0/I/II/III source classification (Lada & Wilking 1984; Lada 1987; Andre et al. 1993), according to which almost all sources of our catalogue would fall in the Class 0 range ($T_{\rm bol} < 70$ K, Chen et al. 1995). At the same time, by revealing a net separation between pre-stellar and protostellar clumps and a pronounced spread inside the distribution of the latter,

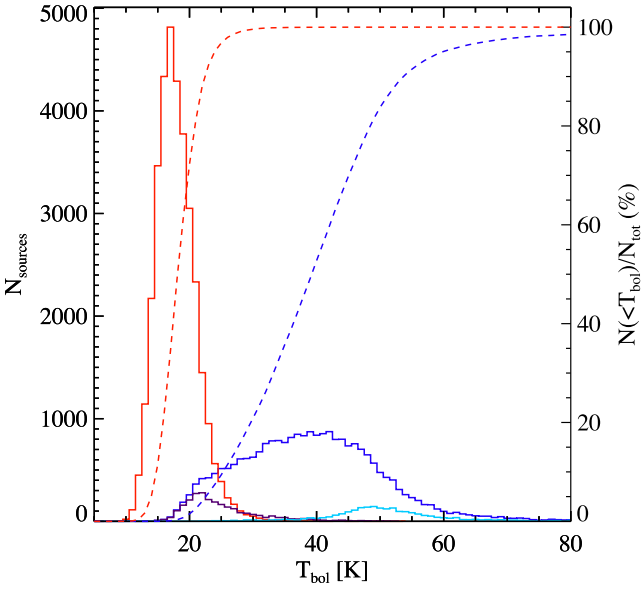

Figure 15. The same as in Fig. 5, but for the bolometric temperature.

bolometric temperatures can still be used to highlight the variety in evolutionary stage of the Hi-GAL sources.

Looking at the histogram of the MIR-dark protostellar sources in Fig. 15, it is evident that these sources represent the low-$T_{\rm bol}$ tail of the overall protostellar distribution. This is expected, given the $T_{\rm bol}$ definition (see equation 5), since small MIR fluxes correspond to low $T_{\rm bol}$ values. In contrast, the H II-region candidates are located towards the highest probed bolometric temperatures, although they do not constitute the totality of protostellar sources at these temperatures. This suggests that bolometric temperature and $L_{\rm bol}/M$ are not perfectly coupled, as it will be discussed in Section 7.2.

In general, typical bolometric temperatures are found to range from ∼10 K (pre-stellar sources) to ∼80 K, a range incompatible with average values for the clump populations of Mueller et al. (2002), 78 K, and Ma et al. (2013), 113 K. A direct comparison with these two works, however, is not appropriate due to the different spectral ranges covered, with the MIR range dominated, in

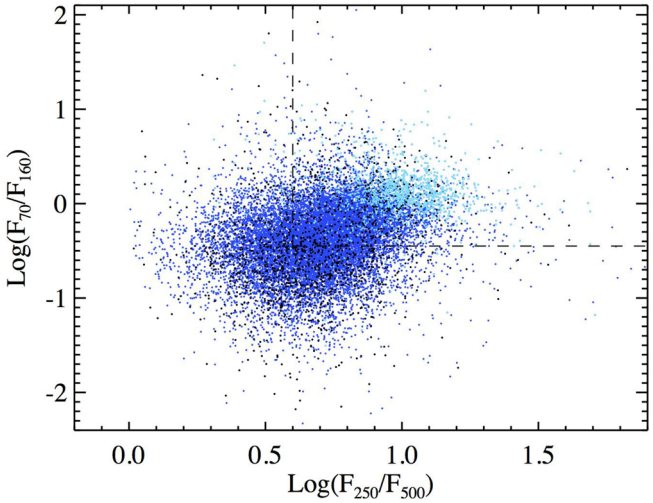

Figure 16. Plot of the F_{70}/F_{160} versus F_{250}/F_{500} colours for the sub-sample of protostellar sources (blue dots) provided with fluxes at these four bands. The positions of sources with no detection in the MIR are overplotted as black dots, while sources identified as H II regions (see the text) are overplotted as light-blue dots. The dashed lines delimit the area identified by Paladini et al. (2012) to contain H II regions.

those cases, by *IRAS* fluxes (see Appendix D for a more detailed comparison between the clump properties derived by Ma et al. 2013 and those in this work).

7 AN EVOLUTIONARY SCENARIO

In this section, we synthesize the physical quantities described above with the aim to formulate an evolutionary classification scheme for protostellar sources.

7.1 *Herschel* colours

Examples of *Herschel*-based colour–colour diagrams are found in literature as tools to perform source evolutionary classification. While here we cannot apply the prescriptions such as those given in Ali et al. (2010) or Spezzi et al. (2013), intended for classifying single low-mass YSOs in nearby star-forming regions, it is, however, interesting to consider and extend the analysis of Paladini et al. (2012) of a sample of 16 H II regions observed in Hi-GAL around $\ell = 30^{\circ}$. In Fig. 16, following these authors, we build the F_{70}/F_{160} versus F_{250}/F_{500} diagram for the protostellar sources of our sample with fluxes at these four wavelengths. Paladini et al. (2012) identify a region at the top right-hand side of the diagram in which *Herschel* fluxes of analysed H II regions are found to lie (despite some contamination by non-H II regions). We find that 8034 of the considered sources (i.e. 48 per cent of the total) are located in this area of the diagram. We highlight with a different colour the positions of sources fulfilling the condition $L_{\rm bol}/M \geq (L/M)_{\rm P}$, which we assume to be H II-region candidates. We find that the great majority of such sources (1297 out of 1391 , i.e. 93 per cent) lie well inside the region defined by Paladini et al. (2012).

It is also interesting to explore the behaviour of the sub-sample of protostellar MIR-dark sources, which are expected to correspond to an earlier evolutionary phase. These appear not to be confined to the H II-region locus and are generally more spread out. This indicates that this choice of *Herschel* colours does not appear to be correlated with the presence of one or more *MSX*/*WISE*/*Spitzer* counterparts.

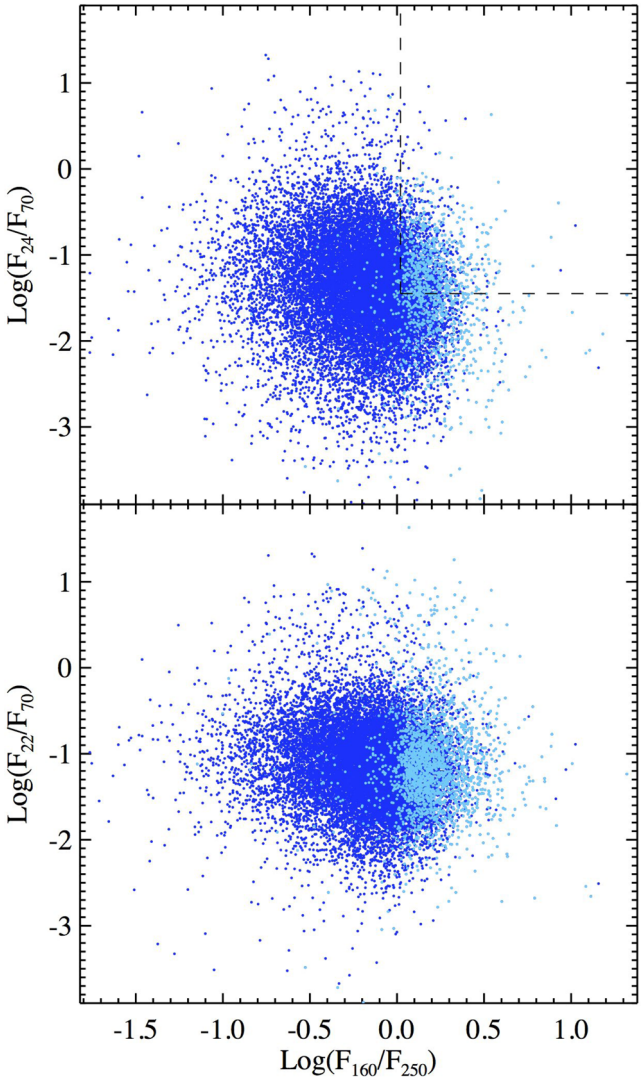

Figure 17. The same as Fig. 16, but for the colours F_{24}/F_{70} (top panel) and F_{22}/F_{70} (bottom panel) versus F_{70}/F_{160}. Each of the two plots is based on the sub-sample of protostellar sources provided with the four fluxes requested to build it. In the top panel, the dashed lines delimit the area occupied by H II regions in the analogous colour–colour diagram of Paladini et al. (2012).

Another diagnostic used by Paladini et al. (2012) is the F_{24}/F_{70} versus F_{160}/F_{250} diagram, thus involving the *Spitzer*-MIPS flux at 24 μm, which is shown in Fig. 17, top panel. As sources with $F_{24} \gtrsim 2$ Jy tend to be saturated in MIPS (Carey et al. 2008), we also construct an F_{22}/F_{70} versus F_{160}/F_{250} diagram using *WISE* 22-μm data (Fig. 17, bottom panel). In both panels, data appear highly scattered, though the sub-sample of sources identified as H II-region candidates still occupies a smaller area of this space, where $\mathrm{Log}(F_{160}/F_{250}) > 0$, similarly to Paladini et al. (2012). The large scatter in the y direction, however, demonstrates that an MIR counterpart does not provide leverage to separate out early-stage sources from a more evolved population in these diagrams.

7.2 Bolometric quantities

Here we explore the relations between the parameters and attempt to use these to better define the evolutionary sequence of protostellar sources.

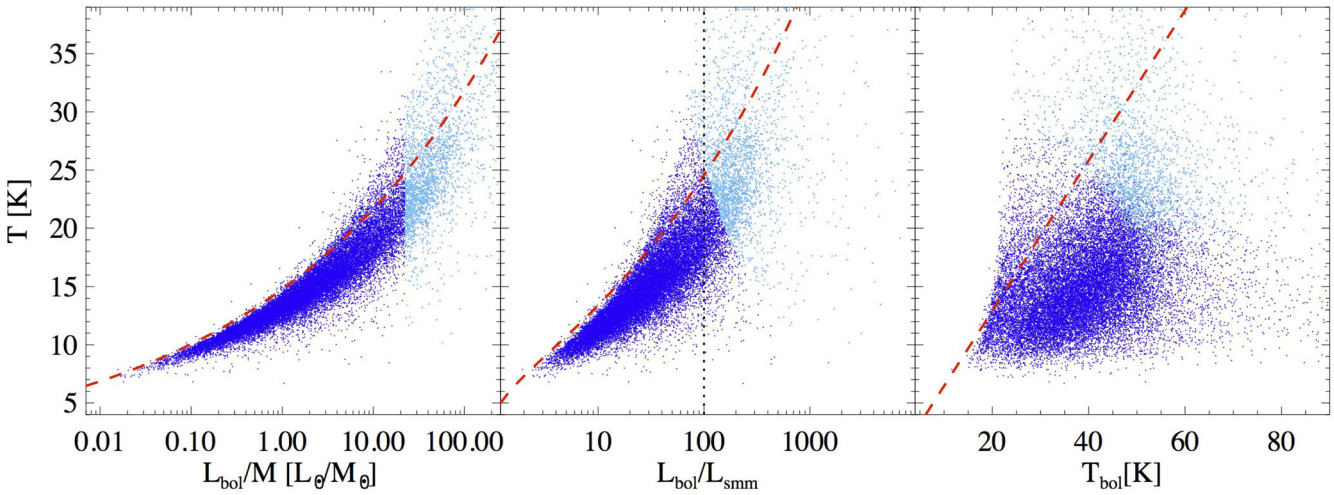

Figure 18. Plot of temperature T of protostellar sources (blue dots) versus the $L_{\rm bol}/M$ ratio (left-hand panel), the $L_{\rm smm}/L_{\rm bol}$ ratio (centre panel) and the bolometric temperature $T_{\rm bol}$ (right-hand panel). The sub-sample of sources compatible with an H II region is plotted in cyan. Red dashed lines represent, in each panel, the expected behaviour of an optically thin grey body (equation 4) with $\beta = 2$, as derived by Elia & Pezzuto (2016). In the centre panel, the vertical dotted line is the same as in Fig. 14.

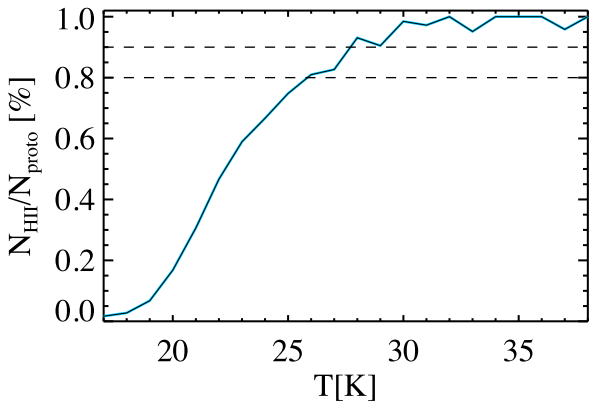

Figure 19. Fraction of protostellar sources classified as H II-region candidates ($L_{\rm bol}/M \geq (L/M)_{\rm P}$) over the total number of the protostellar ones versus temperature. The two horizontal dashed lines indicate the 80 per cent and 90 per cent levels.

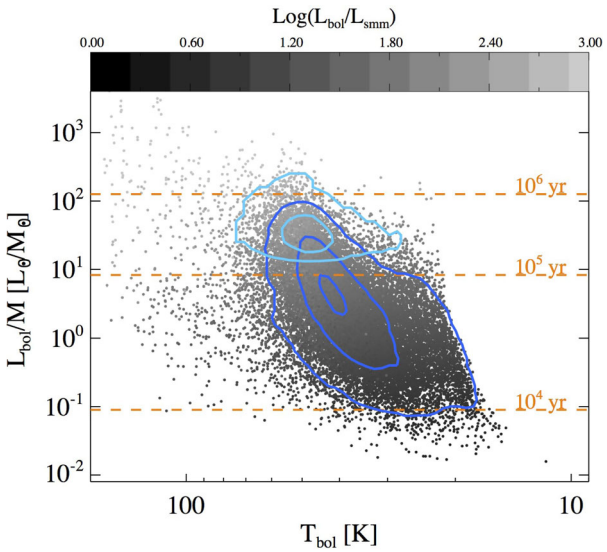

Figure 20. Plot of $L_{\rm bol}/M$ versus $T_{\rm bol}$ for protostellar sources. The dot colour depends on the $L_{\rm smm}/L_{\rm bol}$ ratio of the source, ranging logarithmically from 1 to 1000 (from the darkest to the lightest level of grey present in the plot, respectively; for values outside this range, the colour scale saturates). Blue and light-blue contours represent the areas enclosing, from the innermost to the outermost contour, 10 per cent, 50 per cent and 90 per cent of all the protostellar sources, and of the H II-region candidates, respectively. Dashed orange lines correspond to $L_{\rm bol}/M$ achieved after 10^4, 10^5 and 10^6 yr along the rightmost evolutionary track of Fig. 12.

In Section 6.2, a mild segregation between pre-stellar and protostellar clump grey-body temperatures was found. In Fig. 18, we directly compare the dust temperature with evolutionary indicators such as $L_{\rm bol}/M$, $L_{\rm bol}/L_{\rm smm}$ and $T_{\rm bol}$, introduced in Section 6.5. As expected, all three quantities increase as a function of T. Also, at a given temperature, most of protostellar clumps show an excess of these quantities with respect to the theoretical behaviour of a grey body with $\beta = 2$.

Two general considerations emerge from the three panels of this figure: Since the average temperature estimated for protostellar sources is dominated by the cold envelope modelled as a grey body, it subtends a certain degree of degeneracy of evolutionary stages, which can be resolved, thanks to indicators (reported on the x-axes of the three panels), which are derived by including emission at wavelengths shorter than 70 μm. However, looking at in particular the behaviour of some of the more evolved sources in our sample, such as those compatible with an H II region based on their $L_{\rm bol}/M$ (see Section 6.5), their temperature is definitely high. In Fig. 19, the fraction of protostellar sources classified as H II-region candidates out of the total number of protostellar sources per bin of temperature is shown: At $T \gtrsim 26$ K, 80 per cent of the protostellar sources have an $L_{\rm bol}/M$ greater than the threshold required for classifying it as an H II-region candidate, while the 90 per cent level is achieved at $T \gtrsim 28$ K. This is in good agreement with the estimate of $T = 25$ K by Hofner et al. (2000) for clumps hosting ultracompact H II regions.

To show more directly the mutual connections among $L_{\rm bol}/M$, $L_{\rm bol}/L_{\rm smm}$ and $T_{\rm bol}$, in Fig. 20, we plot $L_{\rm bol}/M$ versus $T_{\rm bol}$ for protostellar sources, while also showing $L_{\rm bol}/L_{\rm smm}$ by means of a colour scale. The source density contours, both for the entire sample of

protostellar sources and for the H II-region candidates, guide the reader through the most crowded areas of the plot.

The evolutionary tracks of Molinari et al. (2008), reported in Fig. 12, can be used for providing a rough estimate of the time elapsed since the beginning of the collapse, given a value of the $L_{\rm bol}/M$ ratio.[7] In Fig. 20, $L_{\rm bol}/M$ values of 10^4, 10^5 and 10^6 yr corresponding to the highest mass track, i.e. the one starting at an initial mass $M_0 = 1500\,{\rm M}_\odot$, are displayed as horizontal lines. According to this rough time-scale, the figure suggests that a large fraction of protostellar sources (18 482 objects) would correspond to an age of $t < 10^5$ yr, while H II-region candidates are found to be well above that value. Comparing with protostellar (Class 0 + I) phase lifetimes of a few 10^5 yr quoted by Dunham et al. (2014) for cores in the Gould Belt, we find that the majority of protostellar sources present in Fig. 20 correspond to a shorter evolutionary time: This indicates a faster evolution for clumps hosting the formation of more massive stars, as a significant part of Hi-GAL clumps are generally supposed to be (cf. Section 6.3).

Recently, Molinari et al. (2016b) calibrated the $L_{\rm bol}/M$ through $CH_3C_2H(12–11)$ line observations, finding that (i) this line is detected at $L_{\rm bol}/M > 1\,{\rm L}_\odot/{\rm M}_\odot$ (which should correspond to a temperature $T < 30$ K in the inner part of the clump), and (ii) the temperature indicated by this tracer starts to increase at $L_{\rm bol}/M > 10\,{\rm L}_\odot/{\rm M}_\odot$, where this threshold is interpreted as the first appearance of a ZAMS star(s) in the clump. Comparing this scenario with our statistics, we find that 50 per cent of our protostellar clumps have $L_{\rm bol}/M$ between 1 and 10 ${\rm L}_\odot/{\rm M}_\odot$, with an average bolometric temperature of 40 K. Only 20 per cent of protostellar clumps, however, have $L_{\rm bol}/M > 10\,{\rm L}_\odot/{\rm M}_\odot$, while – as we expect [since $(L/M)_{\rm P} > 10\,{\rm L}_\odot/{\rm M}_\odot$] – all of the H II-region candidates are above this threshold, having an average bolometric temperature of 55 K.

The $L_{\rm bol}$ versus $T_{\rm bol}$ diagram is a diagnostic used to characterize the YSOs from the evolutionary point of view (Myers et al. 1998). Recently, Strafella et al. (2015) applied it to a population of Hi-GAL sources all belonging to the same region (Vela-D), assumed to be located at the same heliocentric distance. On one hand, it is possible to remove the dependence on distance by taking into account $L_{\rm bol}/M$ instead of $L_{\rm bol}$. The $L_{\rm bol}/M$ versus $T_{\rm bol}$ source behaviour in Fig. 20 is qualitatively similar to fig. 9 of Strafella et al. (2015), given the strongly different amount of sources and the different quantity reported on the y-axis, as explained above. A similar range of $T_{\rm bol}$ is found, as well as some spread in $L_{\rm bol}/M$. This spread becomes remarkably large at high $T_{\rm bol}$, highlighting that these two indicators can, in a few cases mostly concentrated at high bolometric temperatures, give conflicting information about the evolutionary stage of a source. On the other hand, a direct comparison with the plot of Strafella et al. (2015) can be performed by binning sources with respect to distance, which is rendered in Fig. 21 through a colour scale. The box enclosing the positions of the protostellar cores in the analogous plot reported in that paper ($30 \lesssim T_{\rm bol} \lesssim 500$ K, $1 \lesssim L_{\rm bol} \lesssim 300\,{\rm L}_\odot$) still contains a relevant number of sources (2470) from our sample. Nevertheless, a significant fraction of the sources of Strafella et al. (2015) are found to have $T_{\rm bol} > 100$ K, while most of our sources lie below that value. This is essentially due to the wider wavelength range considered by these authors to compute

[7] Of course, such correspondence depends on the considered track, in turn, characterized by the clump initial mass M_0 at time $t = 0$. Furthermore, tracks are obtained for a clump forming a single star, a quite unrealistic case, especially at high clump masses.

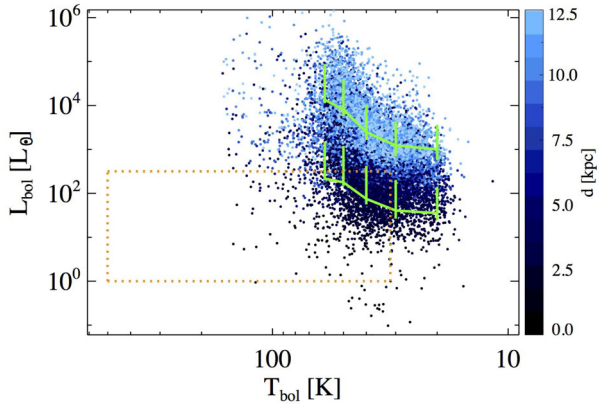

Figure 21. Plot of $L_{\rm bol}$ versus $T_{\rm bol}$ for protostellar sources. The dot colour, described by the colour bar on the right-hand side, scales with the source heliocentric distance (the scale saturates at 12.5 kpc). The orange dashed box corresponds to the region occupied in this diagram by the *Herschel*+*Spitzer* protostellar sources studied in Vela-C by Strafella et al. (2015). As an example, median values of the luminosity calculated over six bins of $T_{\rm bol}$ (starting from 20 K and in steps of 10 K) for sources at $d > 10$ kpc (upper green broken line) and at $d < 3$ kpc (lower green broken line), respectively, are shown. The typical distribution of luminosities being strongly skewed, with a longer tail at high luminosities, it does not make sense to show, as error bars, the values of the standard deviation; therefore, here we use bars defined by the 15th (bottom of the bar) and the 85th percentile (top of the bar), enclosing 70 per cent of luminosity values present in the considered bin of $T_{\rm bol}$.

$T_{\rm bol}$, starting from 3.6 μm, which inevitably leads $T_{\rm bol}$ to increase according to equation (5).

Grouping sources with comparable distances, a general trend of the luminosity to strongly increase with increasing bolometric temperature is seen in the range $15 \lesssim T_{\rm bol} \lesssim 65$ K, which is large enough to reconstruct such a behaviour. This can be seen through two examples we give in Fig. 21, considering sources in the two very different distance ranges, namely $d < 3$ kpc and $d < 10$ kpc. However, in such examples, the log–log slope of $L_{\rm bol}$ versus $T_{\rm bol}$ is everywhere shallower than 6, which is the value expected for a perfect grey body with $\beta = 2$ (cf. equations 35 and 44 of Elia & Pezzuto 2016). This means that, although the departure from a cold grey-body behaviour observed in protostellar envelopes at $\lambda < 160$ μm introduces an excess both in $L_{\rm bol}$ and $T_{\rm bol}$, the latter is more sensitive than the former to the extension of the SED towards shorter wavelengths. Notice that this qualitative consideration is given by neglecting the further effect of the spread in distance underlying the two samples used to draw the curves in Fig. 21.

7.3 Surface density

Here we search for possible correlations between the main source evolutionary indicators and the source surface density introduced in Section 6.3. Notice that this parameter is not derived from only photometric measurements, but also from the source linear size.

In Section 6.3, we have shown that protostellar sources are found to be, on average, slightly smaller and denser than starless ones (Figs 4 and 7). A the same time, the clump column density is observed to decrease with increasing temperature (e.g. IRDCs, Peretto et al. 2010), in such a way that the combination of these two opposing effects contributes to the overlap between the surface density distributions of the starless and protostellar populations seen in Fig. 7. In Fig. 22, panel (a), the surface density versus dust

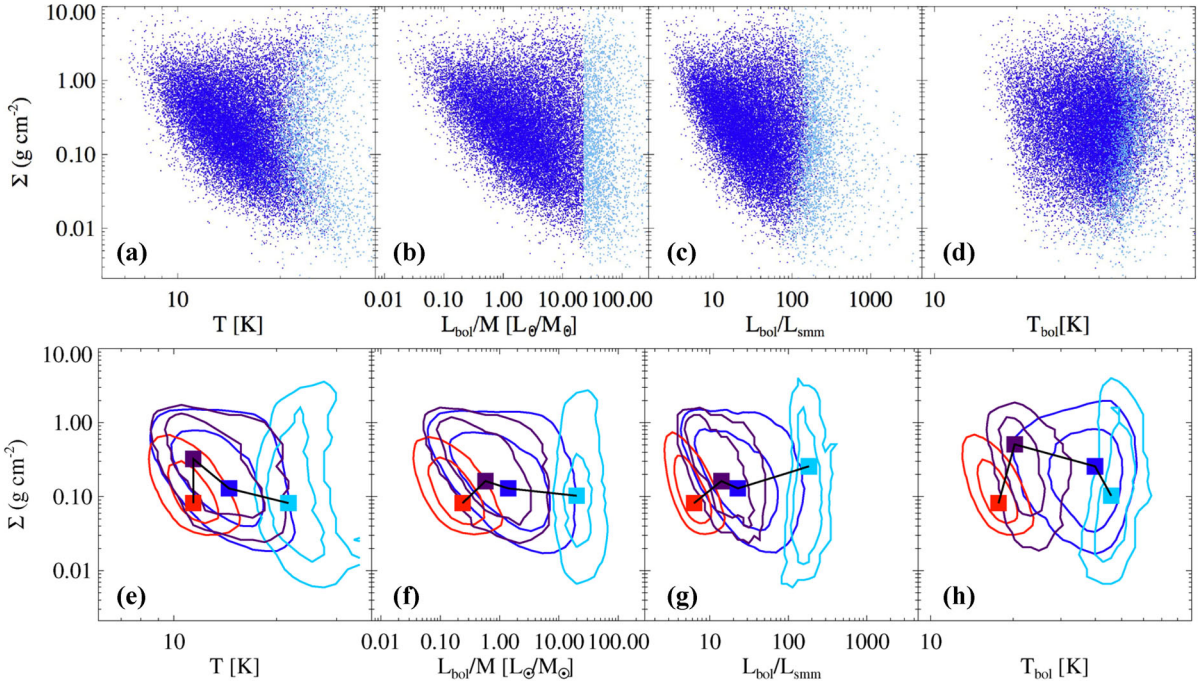

Figure 22. Upper panels: relation between clump surface density and, from panels (a)–(d), dust temperature, $L_{\rm bol}/M$, $L_{\rm bol}/L_{\rm smm}$ and bolometric temperature, respectively. Blue dots represent protostellar clumps, except for the sub-sample of sources compatible with an H II region, plotted in cyan. Lower panels (e)–(h): the same diagrams as in the upper panels, but with source density contours enclosing 90 per cent and 20 per cent of sources, respectively. Contours describing the sample of pre-stellar sources and the sub-sample of MIR-dark protostellar sources are also plotted in red and dark purple, respectively. In absolute terms, hence, the contours drawn for different populations correspond to different values: For example, 34 021 being the total number of pre-stellar sources considered for building this plot, the external contour is drawn in order to contain 6804 sources, and the internal one to contain 30 618 sources; the total numbers of protostellar, candidate H II region and MIR-dark sources are 24 397 , 2377 and 2535 , respectively (notice that the second and third populations are sub-samples of the first one), from which the values corresponding to the source density contours can be easily derived as in the example above. Finally, in each panel, the peaks of the source distributions of the four aforementioned evolutionary classes are reported with filled circles of same colours of the contours, and connected by a black line.

temperature relation is plotted for protostellar sources. The bulk of sources show the aforementioned trend, but with increasing temperatures the spread in surface density increases, so that a remarkable fraction of sources that appear to be, at the same time, dense and warm are found: For instance, considering protostellar sources with $T > 25$ K, a total of 673 have $\Sigma \leq 0.1$ g cm^2 and 611 have $\Sigma > 0.1$ g cm^2 (52 per cent and 48 per cent of the total, respectively). In particular, candidate H II regions are found at the highest temperatures, but the position in the plot is not indicative of any particular trend, spanning the entire range of surface densities, from 0.01 to 10 g cm^{-2}.

Not surprisingly, a similar behaviour is found for Σ versus the $L_{\rm bol}/M$ ratio [Fig. 22, panel (b)], given the tight correlation between T and $L_{\rm bol}/M$ seen in Fig. 18. The plot in panel (c) of Σ versus $L_{\rm bol}/L_{\rm smm}$ is very similar to the previous one, as expected. Finally, a larger spread with respect to previous panels is found in the Σ versus the $T_{\rm bol}$ plot. To highlight a possible evolutionary sequence emerging from these diagrams, we report them in the bottom panels of Fig. 22, showing the source density contours not only for the populations in panels (a)–(d), but also for pre-stellar and MIR-dark protostellar sources. The pre-stellar population occupies a relatively small region in the left-hand part of the diagrams, while apparently no large differences are found between contours of MIR-dark and overall protostellar sources. This confirms the impression obtained in previous sections, namely that the MIR-dark sources do not necessarily constitute the 'earliest stage tail' of the protostellar population. Some degree of segregation is found only with respect to the bolometric temperature (panel (d)), as already suggested by Fig. 15. Finally, the H II-region candidates occupy the right-hand portion of all plots, showing the largest scatter in surface density. Despite the large scatter and partial overlap among different classes of objects, if we consider – in each plot – only the peaks of the source density contours, an evolutionary sequence through various classes might be identified: MIR-dark sources are typically denser than pre-stellar sources, but also denser than generic protostellar ones, and H II-region candidates are normally found at lower densities than the generic protostellar sources. On average, protostellar sources are denser than the starless ones, and characterized by a wide range of densities, often showing a surface density increase in the early stages of star formation, followed by a drop with increasing age (corroborating the results of Giannetti et al. 2013; Guzmán et al. 2015), although cases of evolved sources with large surface densities are also found.

7.4 A tool for source classification

Having examined the clump physical parameters as evolutionary diagnostics, we show a 'radar-plot' visualization of these, which allows a powerful and compact way to show multivariate data. In particular, we chose five distance-independent quantities, namely T, $L_{\rm bol}/M$, $L_{\rm bol}/L_{\rm smm}$, $T_{\rm bol}$ and Σ.

In Fig. 23, the medians of the five indicators for the whole classes of pre-stellar and protostellar clumps are reported on the five axes of the radar plot, and points are connected through a polygonal line

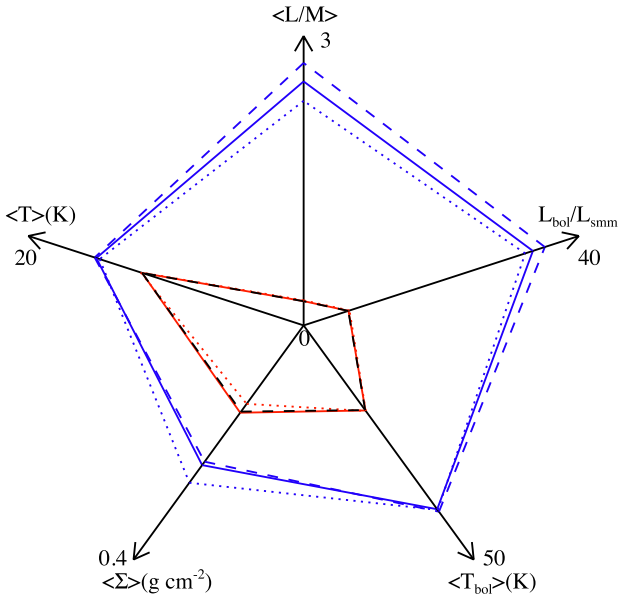

Figure 23. Radar plot for the median of five physical parameters (see text) for the classes of pre-stellar and protostellar clumps (red and blue lines, respectively). Solid lines represent the statistics of the entire populations, whereas separate statistics for the fourth and first Galactic quadrants (see Section 8.1) are represented with dashed and dotted lines, respectively. Scales on each axis are linear, ranging from 0 to the value specified at the end.

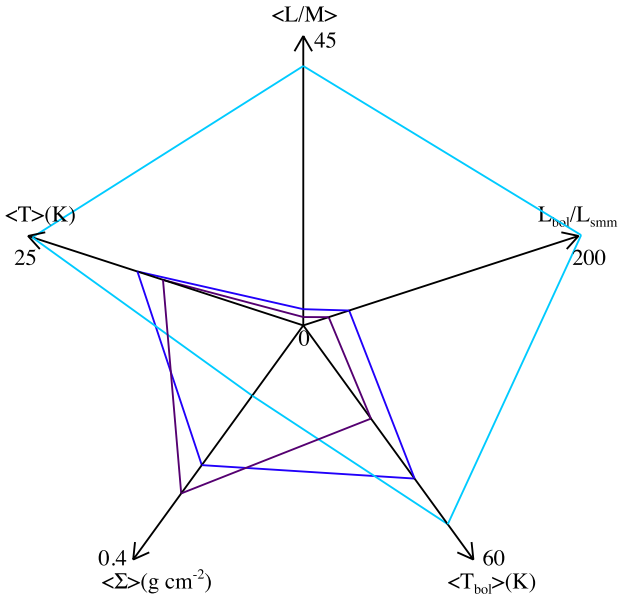

Figure 24. As in Fig. 23, but for protostellar sources (blue line) and for the two extracted populations of MIR-dark sources (dark-purple line) and H II-region candidates (light-blue line), respectively.

to form a pentagon. One can notice that the pentagon corresponding to the protostellar sources includes the pentagon representing the pre-stellar ones, since the values of the considered age indicators are typically larger for the former class of objects. Such a behaviour is also estimated, independently, for the fourth and first Galactic quadrants, as we will discuss in Section 8.1.

The radar plot of the protostellar sources can be further compared with that of the two sub-samples we discussed in previous sections as possible extremes of their age distribution: the MIR-dark and the candidate H II regions, respectively. In Fig. 24, all evolutionary indicators appear decreased for the MIR-dark sample, and enhanced for the candidate H II regions, with respect to the overall protostellar population, except for the surface density, which, as seen in Section 7.3, exhibits the opposite global trend.

The metric described above could be used in the future, for instance, to characterize the properties of clump populations associated with IRDCs (e.g. Traficante et al. 2015), lying on (versus off) filaments (e.g. Schisano et al. 2014), located in the outer (versus inner) Galaxy, etc. Moreover, this representation of the median (or mean) properties of a sample can be applied to a single source, allowing one to immediately assess if and how this approaches or deviates from the global behaviour of a certain class of sources this, in principle, belongs to.

8 SOURCE SPATIAL DISTRIBUTION ALONG THE GALACTIC PLANE

8.1 First versus fourth Galactic quadrant

So far we considered the global statistics of the Hi-GAL sources, regardless of their position in the Galactic plane. In this section, the statistics of Hi-GAL source properties are presented in bins of Galactic longitude, and discussed in view of a comparison between the fourth and first quadrants. To introduce this analysis, with particular respect to the discussion of distance-dependent observables, first of all we show the heliocentric distance distribution in the fourth and the first Galactic quadrants, separately (Fig. 25). The main differences, i.e. those extending over more than two bins, are seen around 3–4 kpc, where fourth-quadrant sources are predominant in number, and around 4.5–7 kpc, where the opposite case is found. However, the overall behaviour of the two distributions is similar, thus making a comparison between the two quadrants feasible for distance-dependent properties such as mass, linear size and luminosity (see below).

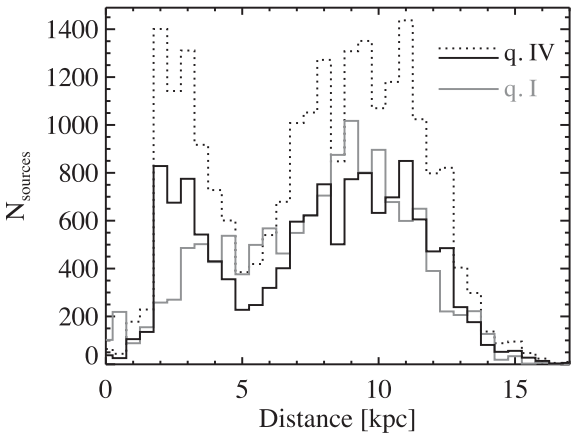

Figure 25. Source heliocentric distance distributions (cf. Fig. 4, left-hand panel), obtained separately for the fourth (black) and first (grey) quadrants, respectively. To better compare the two distributions, the original fourth quadrant histogram (dotted line) has been normalized (solid line) by the ratio of the total source counts in the two quadrants.

Fig. 26 presents the starting points for discussing the distribution of sources and their properties in the plane. Panel (a) shows how sources are distributed in longitude. A relation with the trends found in single-band catalogues by Molinari et al. (2016a) is expected, despite the SED filtering carried out in this work. In fact, for each

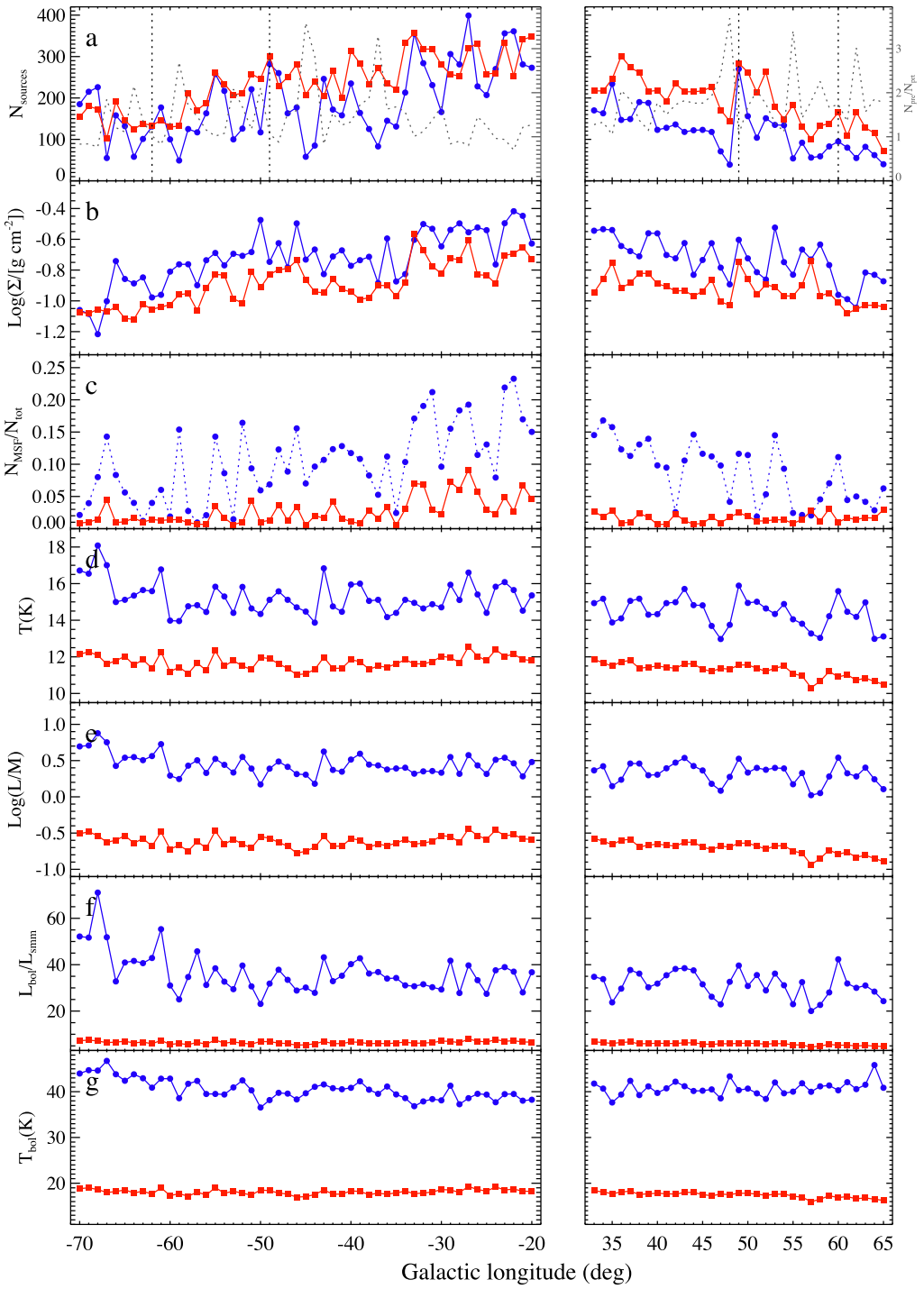

Figure 26. Distribution of relevant quantities obtained in this paper for pre-stellar (red filled squares) and protostellar (blue filled circles) sources as a function of the Galactic longitude, averaged over bins of width 1°, in the longitude range of the fourth (left-hand panels) and first (right-hand panels) Galactic quadrants considered in this work: (a) source number (where the dotted black line represents the pre-stellar over protostellar source number ratio reported on the right-hand axis); (b) median of the decimal logarithm of surface density; (c) fractional number of dense clump fulfilling conditions for massive star formation (according to Krumholz & McKee 2008); (d) median temperature; (e) median of the decimal logarithm of $L_{\rm bol}/M$; (f) median of the $L_{\rm bol}/L_{\rm smm}$ ratio; and (g) median of bolometric temperature.

physical quantity, we have considered that (i) a positive correlation is found moving towards the inner Galaxy, and (ii) as shown by Molinari et al. (2016a), for both pre-stellar and protostellar sources, localized excesses are found at positions corresponding to spiral arm tangent points or star-forming complexes.

Enoch et al. (2008) used the number ratio between starless and protostellar cores to roughly estimate, through a proportionality factor, the lifetime of the cores they detected in nearby low-mass star-forming regions. Because, in our case, we are dealing with clumps instead of cores, we cannot apply a similar prescription

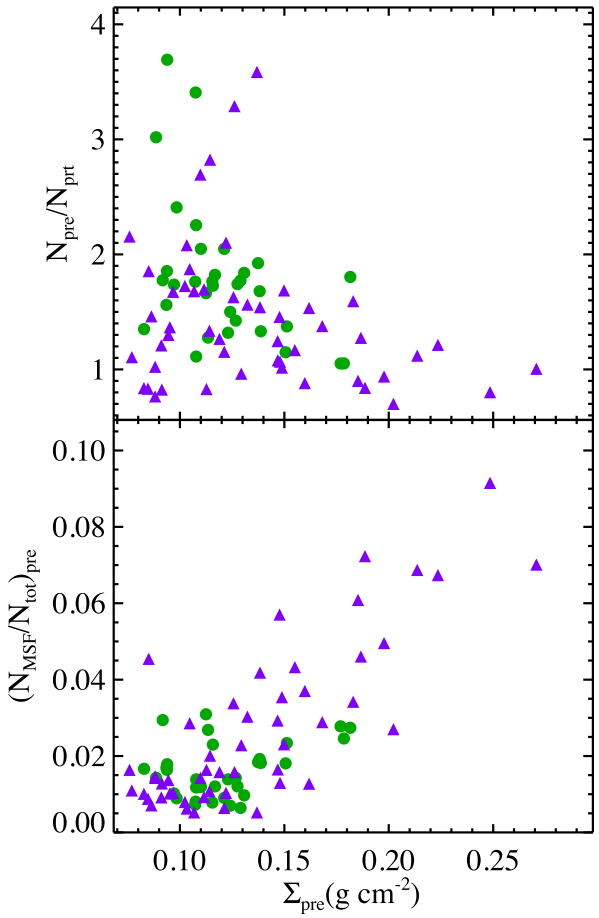

Figure 27. Number ratio of pre-stellar on protostellar sources (top panel), and of sources compatible with massive star formation on the total (bottom panel), as a function of the median surface density of pre-stellar sources, estimated in the same 1° bin of Galactic longitude. Data are taken from Fig. 26(a)–(c). Data from the fourth and first Galactic quadrants are represented with purple triangles and green circles, respectively.

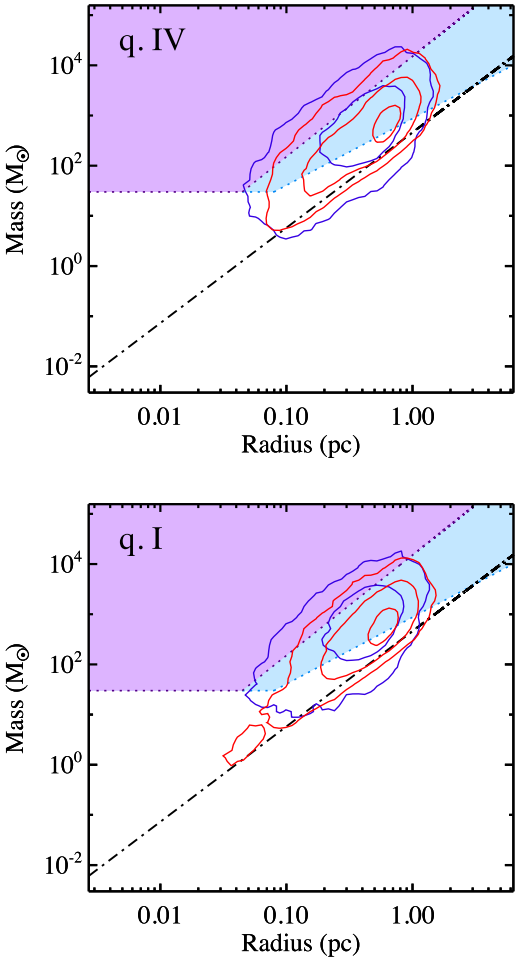

Figure 28. The same contour plots as in bottom left-hand panel of Fig. 7, but obtained separately for sources in the fourth (top panel) and first (bottom panel) Galactic quadrants, respectively.

directly, although useful considerations can be made concerning clumps. Our clump statistics give a ratio of ∼1, which, as found by Svoboda et al. (2016) on their sample of 4683 clumps identified at 1.1 mm in the first quadrant, would be suggestive of comparable lifetimes for the two classes (see also Motte et al. 2010b; Ragan et al. 2013). Here, thanks to large statistics, we are able to describe this quantity, N_{pre}/N_{prt}, as a function of Galactic longitude [Fig. 26, panel (a)]. Pre-stellar sources are in excess with respect to protostellar ones almost everywhere, except for a few cases where $N_{pre}/N_{prt} < 1$ in the fourth quadrant. In general, this ratio is lower in the fourth quadrant, i.e. 1.25 versus 1.63 for the first quadrant.

To infer relative clump lifetimes from this number ratio is not trivial, since time-scales can also depend on the mass. Indeed, the deficit of pre-stellar sources with respect to protostellar ones at both the lowest and the highest masses found at a given heliocentric distance was extensively discussed in Section 6.4, concluding that, in particular, it should be due to rapid evolution of the most massive, but also densest pre-stellar clumps from the quiescent phase to star-forming activity. A synoptic look at panels (a) and (b) (the latter showing the median surface density) of Fig. 26 seems not to confirm such a scenario, since no evident correlation is seen between N_{pre}/N_{prt} and density. However, plotting the former against the latter (Fig. 27, top panel), values of $N_{pre}/N_{prt} > 2$ are found only for lower median surface densities of pre-stellar sources ($\Sigma \lesssim 0.15$ g cm^2). Furthermore, at higher densities ($\Sigma \gtrsim 0.2$ g cm^2), only cases with $N_{pre}/N_{prt} < 1.3$ are found. Unfortunately, we cannot consider this as a strong argument, since the inverse of these statements is not found to be true in general. Future studies, focused on a more accurate identification and analysis of specific regions characterized by a very high or a very low N_{pre}/N_{prt}, will better assess the relation with pre-stellar clump density.

The fraction of sources exceeding the threshold necessary for massive star formation (N_{MSF}/N_{tot}) according to the prescription of Krumholz & McKee (2008) (see Section 6.3) is shown in panel (c) of Fig. 26, again separately for pre-stellar and protostellar sources. As explained in Section 6.3, only starless sources are suitable for this analysis, and this fact is highlighted in the plot by connecting the protostellar distribution through a dashed line instead of a solid one. A few remarks can be made about this plot:

(i) The fraction of pre-stellar clumps potentially able to form massive stars $(N_{MSF}/N_{tot})_{pre}$ is generally higher in the fourth rather than in the first quadrant. This can also be seen by plotting the mass versus radius diagram for the two quadrants separately, as in Fig. 28: Both quadrants denote, with respect to the two adopted density thresholds, a similar ability to form high-mass stars, but the fraction of pre-stellar sources in the fourth quadrant populating the Krumholz & McKee (2008) area is slightly larger.

(ii) In the first quadrant, a relevant amount of pre-stellar sources that are massive and dense enough to give rise to possible high-mass star formation are found. In particular, while Ginsburg et al. (2012), based on BGPS data, claim that no quiescent clumps with $M > 10^4\,M_\odot$ and $r < 2.5$ pc are found in the range $6^\circ < \ell < 90^\circ$ (confirmed by Svoboda et al. 2016, after an accurate analysis in the range $10^\circ < \ell < 65^\circ$), in our catalogue we find 22 sources, located in the range $67^\circ < \ell < 16^\circ$, that fulfil these criteria. To explain such a discrepancy, one should perform a dedicated analysis, which is beyond the scope of this paper. Here we limit ourselves to emphasizing two aspects. First, for all sources of this group, the ambiguity about the heliocentric distance has been solved in favour of the 'far' solution (the minimum distance in the group being $d = 5979$ kpc, and 11 sources out of 22 have a distance in the catalogue $d > 10$ kpc). A different distance estimate has a linear effect on radius, but a quadratic effect on the mass, and these, in turn, could potentially affect source classification. Secondly, the masses of Ginsburg et al. (2012) are estimated for a constant temperature of $T = 20$ K (a value that is far from being representative of a starless clump, as seen in this paper), while in our case they are derived from a grey-body fit simultaneously with temperature: For the 22 sources in question, the derived temperatures are significantly lower than 20 K (with an average of 16.4 K), therefore leading to much higher values of mass. Indeed, at 1.1 mm (the wavelength used by Ginsburg et al. 2012), assuming a grey-body temperature of 20 K instead of 13 K underestimates the mass by a factor of $\sim$2, independently of the choice of β. Svoboda et al. (2016) used a more accurate estimate of temperature, derived from NH_3 line observations of each source, which, in global terms, is still higher for pre-stellar sources (a median of 13.96 K against 11.7 K in our case, see Section 6.2). In addition to this, in the particular case of our 22 sources, grey-body temperatures are found to be generally lower, with 16 of them having $T < 10$ K. Such a temperature can be genuine but could also be attributed to an SED affected by problems in the original photometry or by a relevant deficit of flux at the shortest wavelengths involved in the fit, due to multiplicity (see Section 3.1). A dedicated analysis is required for this group of sources to better define their physical conditions and confirm whether they might be genuine progenitors of massive protoclusters, or simply statistical fluctuations in a huge catalogue.

(iii) In the fourth quadrant, $(N_{\rm MSF}/N_{\rm tot})_{\rm pre}$ is found to increase towards inner longitudes ($\ell \gtrsim -35^\circ$).

(iv) As expected, in general, there is a direct relation between $N_{\rm MSF}/N_{\rm tot}$ for pre-stellar sources and the corresponding median surface density (for pre-stellar sources), shown in Fig. 27, bottom panel.

We can now start analysing the behaviour of the evolutionary diagnostics. We begin with dust temperature, whose distribution is shown in Fig. 26, panel (d). We notice that the two Galactic quadrants do not present significant differences, as can also be seen in Fig. 29, similar to Fig. 5 but with the temperature distributions given separately for the fourth and first quadrants. If we compare the top and bottom panels of this figure, the distribution of protostellar sources in the fourth quadrant peaks at slightly higher temperatures with respect to the equivalent population in the first quadrant, with the average and median temperatures of $\bar{T}_{\rm prt,IV} = 16.2$ K and $\tilde{T}_{\rm prt,IV} = 15.3$ K in the fourth quadrant, and $\bar{T}_{\rm prt,I} = 15.8$ K and $\tilde{T}_{\rm prt,I} = 14.8$ K in the first quadrant, respectively. Notice, however, that the associated standard deviations of 5 K in all cases make this difference poorly significant from the statistical point of view. In the following, however, further slight differences between source properties in the two quadrants, globally indicating a more evolved stage of sources in the fourth quadrant, will be discussed.

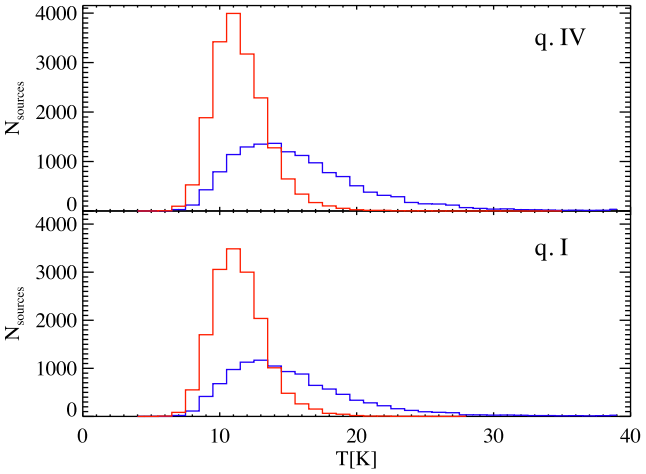

Figure 29. The same histogram as in Fig. 5, but obtained separately for sources in the fourth (top panel) and first (bottom panel) Galactic quadrants, respectively.

No significant differences are found for the pre-stellar sources in the two quadrants ($\bar{T}_{\rm pre,IV} = 12.0$ K versus $\bar{T}_{\rm pre,I} = 11.9$ K, and $\tilde{T}_{\rm pre,IV} = 11.8$ K versus $\tilde{T}_{\rm pre,I} = 11.7$ K, respectively).

Fig. 26, panel (d), shows the median temperature as a function of the Galactic longitude. It can be seen that three strong local peaks ($\tilde{T} \geq 17$ K) at -68°, -61° and -43° are found in the fourth quadrant, while two dips ($\tilde{T} \leq 13$ K) at 47° and 57° are found in the first one. However, these do not correspond to large source counts [Fig. 26, panel (a)], indicating that they should not be considered as the main cause of the overall discrepancy between the two quadrants, which therefore is more indicative of a general trend.

Peaks and dips in the temperature distribution are found in the same longitude bins for $L_{\rm bol}/M$ and $L_{\rm bol}/L_{\rm smm}$ [Fig. 26, panels (e) and (f), respectively]. This is not surprising, given the tight relation between the temperature and these two indicators, as suggested by Fig. 18. A weaker correlation is seen with bolometric temperature [Fig. 26, panel (g)].

Except for the features mentioned above, the global $L_{\rm bol}/M$ behaviour in the two quadrants does not appear very different, as corroborated by two observational facts:

(i) In Fig. 30, in which $L_{\rm bol}$ versus M, in the form of density contours, is plotted separately for the two quadrants, the overall source distribution appears to be concentrated in the same region of the diagram, with respect to the evolutionary tracks of Molinari et al. (2008).

(ii) The mean and median values of this ratio for protostellar objects, namely $[(L_{\rm bol}/M)_{\rm prt,IV}]_{\rm med} = 2.7\,L_\odot/M_\odot$ and $[(L_{\rm bol}/M)_{\rm prt,I}]_{\rm med} = 2.3\,L_\odot/M_\odot$, respectively, are very similar. They are also reported in Fig. 23, together with other evolutionary indicators. The charts corresponding to the protostellar population of the two quadrants show only slight differences, although, interestingly, these appear to be systematic: The fourth quadrant has larger T, $L_{\rm bol}/M$, $L_{\rm bol}/L_{\rm smm}$ and $T_{\rm bol}$, and lower Σ, which unequivocally indicate a (slightly) more advanced stage of evolution.

8.2 Spiral arms and star formation

The physical properties discussed in the previous section provided a first 'one-dimensional' picture of how the sources of the Hi-GAL

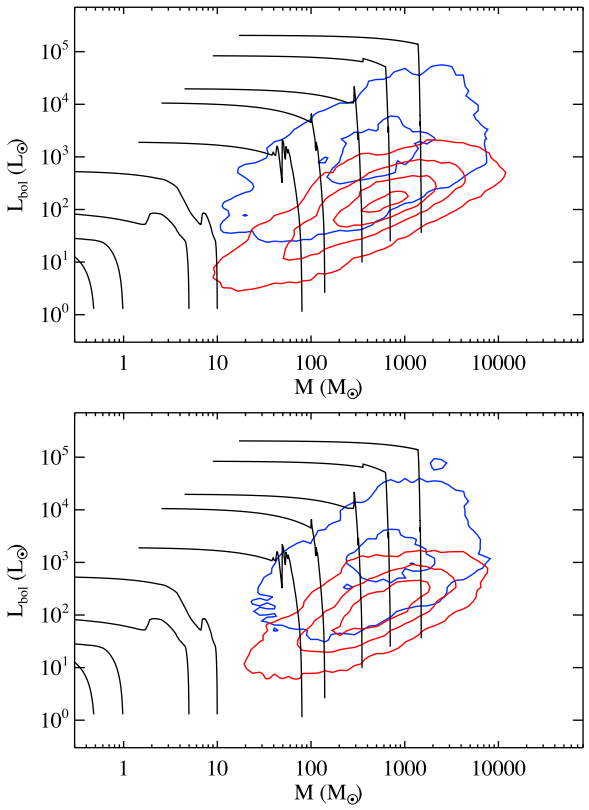

Figure 30. The same plot of L_{bol}/M as in Fig. 12, but obtained separately for sources in the fourth (top panel) and first (bottom panel) Galactic quadrants, respectively.

catalogue are distributed across the Milky Way. A more complete analysis also has to incorporate source distances to investigate their position in the Galactic plane, with respect to spiral arm topology, as already suggested by Fig. 1. In the interest of completeness, we briefly touch here on this topic, while for more details and and an extensive discussion we refer the reader to Ragan et al. (2016).

In Fig. 31, as in Fig. 1, we show the overall distribution of the Hi-GAL clumps along the Galactic plane as well as the location of the spiral arms according to the model of Hou et al. (2009). In this new figure, however, we also make an attempt to associate clumps with spiral arms. To this end, we use an arm width of 1 kpc, and then a source-to-arm association distance of 0.5 kpc (cf. Eden et al. 2013). According to this criterion, 21 996 sources out of 36 535 considered for this analysis (i.e. those provided with a heliocentric distance estimate) are associated with the arms. In addition, 14 539 are classified as 'interarm, thus an ∼2: 3 ratio, significantly different from the 1:7 expected by simulations of Dobbs & Bonnell (2007), but in better agreement with the observational evidence of Eden et al. (2013), namely 21:38 for BGPS sources between $\ell = 37.^\circ8$ and $42.^\circ5$. However, we should make the reader aware that this association between sources and arms and the consequent results are strongly affected by heliocentric distance determination, which is still a critical point in our analysis. While a new set of Hi-GAL source distances based on an improved algorithm is expected (Russeil et al., in preparation), cross-checks can be carried out (although on a relatively small number of cases) with distances quoted for objects in common with surveys such as ATLASGAL (Wienen et al. 2015) or BGPS (Ellsworth-Bowers et al. 2015) (see Appendix D). In this way, a distance estimate external to our catalogue and considered more reliable can be assumed to easily rescale the distance-dependent source properties quoted in our catalogue.

As already evident from Fig. 1, overdensities of source counts do not always correspond to arm locations. This certainly also depends on the spiral arm model of choice (see e.g. Ragan et al. 2016) but, even more, is primarily inherent to the set of estimated distances. As a matter of fact, different spiral arm models will provide different solutions so, for a certain model, a source will result being 'on-arm', while, for another, it might turn out to be 'off-arm'. Moreover, the on–off location of clumps with respect to spiral arms will also strongly depend on kinematic distances, which are notoriously limited – by their intrinsic uncertainties – in their ability of delineating the morphology of the arms. Therefore, the prescription we adopted to associate Hi-GAL clumps to spiral arms produces sharp and unnatural separations between on-arm and off-arm populations (see Fig. 31), which affects a possible comparison of the two, as well as the remaining analysis. This aspect was already evident in Roman-Duval et al. (2009), who examined the same spectroscopic survey, namely GRS, that we use here to determine distances in the first Galactic quadrant: They found that only 63 per cent of ^{13}CO emission can be associated with spiral arms, while several bright and large structures fall in 'interarm' gaps.

With these caveats in mind, we present some statistics based on grouping sources belonging to the same arm, and distributed at a different Galactocentric radius R. In Fig. 32, panel (a), first of all, we show the number statistics of protostellar objects, which the other panels are based on. This information is useful to understand the reliability of statistics presented in the other panels: Clumps are counted in bins of 0.5 kpc of Galactocentric radius, and bins poorly populated (i.e. <50 sources) are ignored in the following. The overall number of protostellar sources as a function of R is reported in panel (b), together with the same curve for pre-stellar sources [used to build the plot in panel (d)] and for the sum of the two classes. A direct comparison of the latter with the Galactocentric radius distribution of ATLASGAL sources presented by Wienen et al. (2015) is not straightforward. This is because, in that case, the plot is split between the first and fourth Galactic quadrants, and because counts are expressed in surface density, therefore normalized by area. As in Wienen et al. (2015), a peak is found around 4.5 kpc, corresponding to the peak of the light-blue line in panel (a), so that we agree with those authors that this enhancement corresponds to the intersection of the Crux–Scutum arm and the Galactic bar in the first quadrant (see also Nguyen Luong et al. 2011; Motte et al. 2014). Another peak (the largest we find) is encountered around 6.5 kpc, and again it is mostly due to the Crux–Scutum arm, but, in particular, to its portion in the fourth quadrant. In both cases, the curve of 'interarm' clumps closely follows that of the Crux–Scutum arm and strongly contributes to the aforementioned peaks, corroborating the fact that, in many locations, the distinction between 'on-arm' and 'interarm' locations is quite artificial due to the method we used to identify them. Finally, at $R \sim 10$ kpc (this distance is not probed by Wienen et al. 2015), sources of the Carina–Sagittarius arm produce a peak, which is mirrored in the overall source distribution as a plateau interrupting a decreasing trend found over a range of 2.5 kpc.

In panel (c), the ratio between pre-stellar and protostellar clumps N_{pre}/N_{prt} (discussed in Section 8.1 as a function of Galactic longitude) is shown in bins of R for different arms and for the 'interarm' sources. Values range from 0.7 to 1.8, but no specific trends are found either for the behaviour of individual arms or in the comparison between 'on-arm' and 'interarm' sources. Therefore, no suggestions come from this plot about a possible role of spiral arms in triggering or regulating star formation, confirming the conclusions

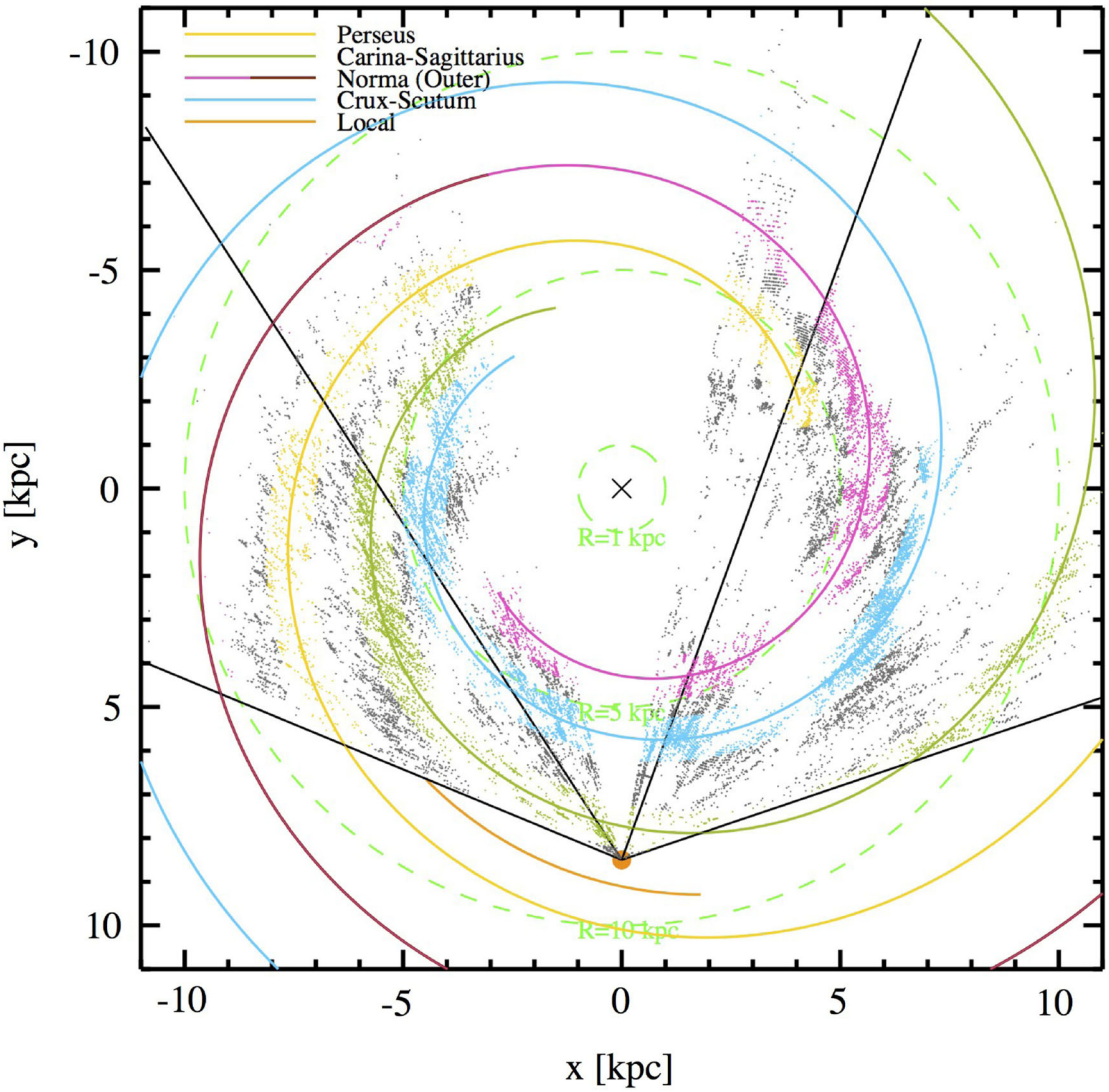

Figure 31. The same as Fig. 1, but with different colours for dots representing sources: positions within a distance 0.5 pc from the theoretical position of an arm are assigned to it and displayed with the same colour (with no reference to the starless versus protostellar classification). The remaining sources, found at 'interarm' locations, are displayed in grey.

of Eden et al. (2013) and Ragan et al. (2016). Analogously, the distributions of three evolutionary indicators such as median dust temperature, bolometric luminosity/mass ratio and bolometric temperature of protostellar sources [panels (e), (g) and (i), respectively] show a high degree of scatter and no substantial differences between arm and 'interarm' sources. A recognizable trend is present in the distribution of median bolometric temperatures, which generally increases at increasing R for all arms and for the interarm component as well. This is more evident in the overall behaviour shown in panel (j), even ignoring bins at $R > 8$ kpc, which are dominated by the Carina–Sagittarius arm in the fourth quadrant, and which are generally characterized by high values for the evolutionary indicators, as also seen in panels (e), (g), (f) and (h), although based on relatively poor statistics [see panel (a)]. Finally, the distributions of surface densities reported in panel (k) show a slightly decreasing trend with R, as recognized in all curves and in the overall distribution [panel (l)]. A linear fit to the overall distribution between 4.5 and 9 kpc to the latter gives the relation $\log_{10}(\Sigma/(\mathrm{g\,cm^{-2}})) = 0.50 - 0.04(R/\mathrm{kpc})$. A much stronger decrease of clump surface peak is claimed by Zahorecz et al. (2016), who found a drop of three orders of magnitude over the range 0–13 kpc, but this quantity cannot be directly compared with our average surface density. More generally, encountering less dense clumps at farther distances from the Galactic Centre is in agreement with the result of Ragan et al. (2016): These authors define a 'star-forming fraction' as the number ratio (based on the present catalogue) between protostellar clumps and all clumps, and find a general trend decreasing with increasing R (with a slope of -0.025). In other words, a correlation between the gradual decrease of star formation activity at large Galactocentric radii and the decrease of the clump densities (i.e. of material available for gravitational collapse) can be hypothesized.

9 SUMMARY

We presented the physical catalogue of Hi-GAL compact sources extracted in the inner Galaxy (in the longitude range $\ell = -71^\circ$ to 67°). First, we described how sources were selected from the

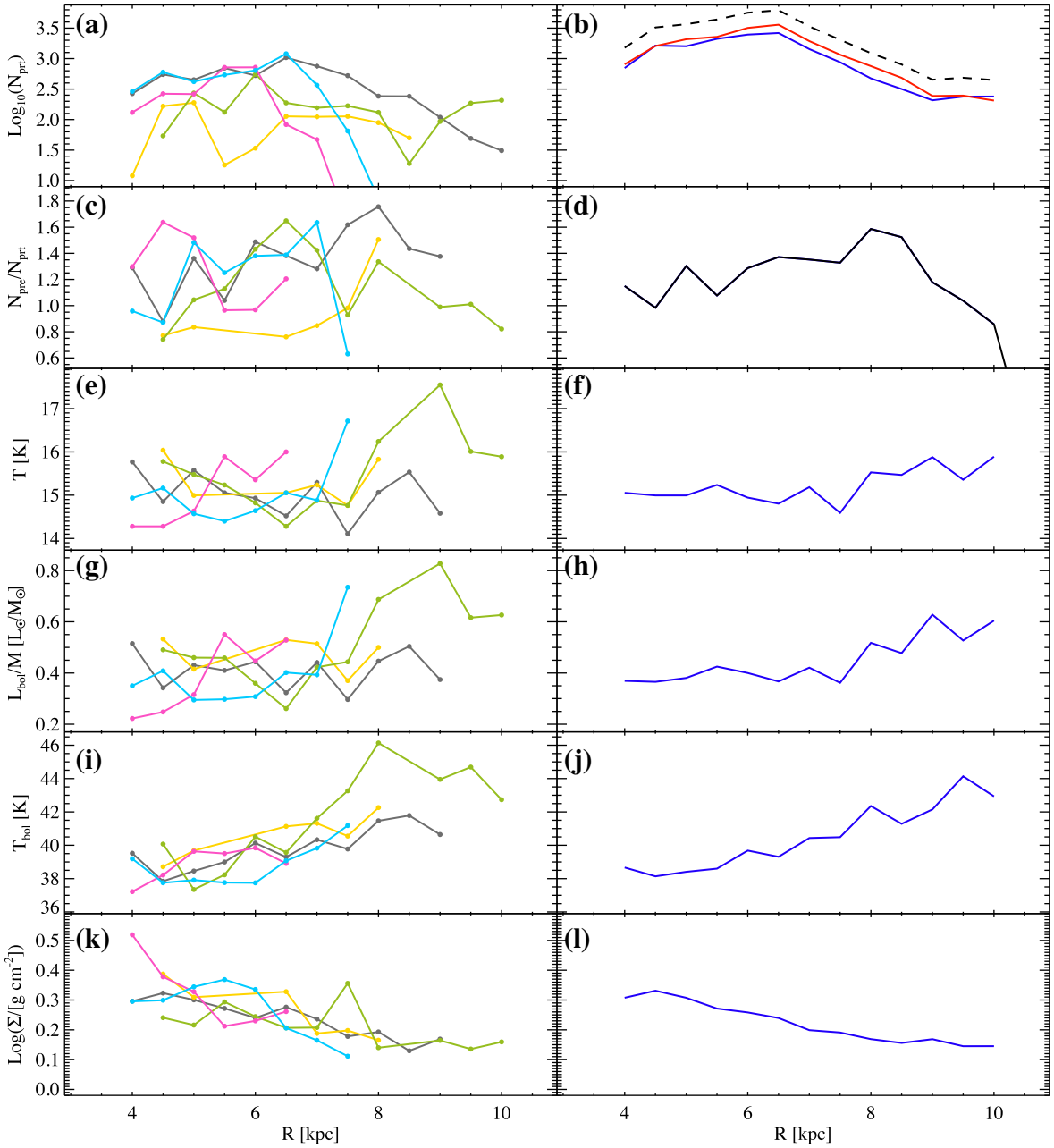

Figure 32. Number and physical properties of protostellar clumps with a distance estimate, in bins of Galactocentric radius (bin width is 0.5 kpc). In the left-hand panels, different quantities are plotted separately by spiral arms (see Figs 1 and 31 for colour coding) with the addition of 'interarm' sources (in grey). In the right-hand panels, the overall sample of protostellar sources is considered. In detail, panel (a) shows the logarithm of the number of protostellar sources, while panel (b) shows the sum of them (blue solid line); the counts of pre-stellar and the sum of pre-stellar + protostellar are also reported as red solid and black dashed lines, respectively. In panel (c), the number ratio of pre-stellar over protostellar sources is reported, while in panel (d), the same quantity is computed and reported for the entire source population (black line). Panels (e), (g), (i) and (k) are similar to panel (c), but for dust temperature, logarithm of the luminosity-to-mass ratio, bolometric temperature and logarithm of surface density, respectively. Correspondingly, panels (f), (h), (j) and (l) report the same distributions, but calculated over the entire population of protostellar sources.

Hi-GAL five-band photometric catalogue and how their physical properties were estimated. To this aim, we performed the following:

(i) Five single-band photometric catalogues of Molinari et al. (2016a) were merged, based on simple positional associations. A total of 100 922 SEDs eligible for grey-body fit were selected and considered for subsequent analysis, of which 57 065 included a heliocentric distance estimate (no distances are available in the central part of the Galaxy: $-10.^{\circ}2 < \ell < 14.^{\circ}0$).

(ii) A targeted flux extraction at 160 and 70 μm has been performed for sources missing a flux at these bands. Sources remained with only three Hi-GAL fluxes have been reported in a 'lower reliability' list. Furthermore, the *MSX*, *WISE*, MIPSGAL, ATLASGAL and BGPS catalogues have been searched for possible geometric counterparts, to extend the spectral coverage of the SEDs.

(iii) After SED building and filtering, 24 584 sources containing a flux at 70 μm have been classified as protostellar, while the remaining 76 338 sources as starless. Furthermore, based on

subsequent SED fitting and mass computation, starless sources have been classified as gravitationally bound (pre-stellar) or unbound (16 667 and 59 671 , respectively). Both these criteria are applied directly and uniquely on photometric data, and for this reason, they are prone to be refined in the future using other observational evidence. Furthermore, they cannot completely remove a certain degree of contamination among different evolutionary classes.

(iv) A grey-body spectrum has been fitted to SEDs, to obtain the average temperature and the total mass of a clump (in the case of an available distance, otherwise, at least the clump surface density has been derived, taking the source diameter at 250 μm as a reference size). The bolometric luminosity has been derived for sources provided with a distance estimate, while the bolometric temperature has been obtained for all sources.

Once the physical properties of the sources had been derived, we explored the distributions of these observables, their mutual relations with a possible evolutionary scenario and their possible connection with the Galactic large-scale structure. Main results are summarized below:

(v) Based on their size, the sources in this catalogue are in most cases classifiable as clumps. For a given distance, protostellar clumps are found to be, on average, more compact than starless ones. Consequently, the former are found to be generally denser than the latter.

(vi) A significant amount of sources, both pre-stellar and protostellar, are found to fulfil one or more criteria for compatibility with high-mass star formation. This sample can be extracted for large programmes of follow-up observations aimed to clarify the internal structure of dense clumps and put observational constraints on models of high-mass star formation.

(vii) The mass function of protostellar sources falling in a relatively narrow ($\Delta d = 0.5$ kpc) distance range generally appears wider than that of pre-stellar sources, due to completeness effects at low masses, and to a relative deficit of pre-stellar clumps at high masses (in turn likely due to evolutionary effects). As a consequence of this, the power-law slope of the pre-stellar function is systematically steeper than that of the protostellar one. Finally, no systematic bias seems to affect the mass function slope at increasing heliocentric distance.

(viii) The clump average temperature, estimated over the range $160 \leq \lambda \leq 500$ μm (so with no reference to the presence of counterparts at shorter wavelengths) and representing the physical conditions of the outer part of the clump structure, acts as an evolutionary indicator: The median temperature for pre-stellar clumps is 11.7 K, while for protostellar sources, it is 15.1 K. However, a high degree of overlap between the two populations remains and the combined use of further evolutionary indicators is then recommended to reduce such degeneracy.

(ix) We used the bolometric luminosity and its ratios with the clump mass and the sub-mm luminosity, together with the bolometric temperature, as further evolutionary indicators. An acceptable degree of separation between pre-stellar and protostellar populations is found by analysing the distributions of these observables. Since the protostellar sources span a wide range of evolutionary stages, we tried to identify possible candidates to represent both the earliest and the latest stages that we are able to probe with Hi-GAL. On one hand, we found that sources dark in the MIR may play the former role only in part, while, on the other hand, sources with $L_{\rm bol}/M > 22.4\,{\rm L}_{\odot}/{\rm M}_{\odot}$ represent the right-hand tail in the distribution of all evolutionary indicators, and are compatible, for temperature and colours, with the stage of H II regions, although this requires further observational evidence to be gathered.

(x) The behaviour of surface density with respect to clump evolution shows, in general, an increase from the pre-stellar to the protostellar phase, and a decrease (but with a large spread of values) in the most evolved protostellar objects, corresponding to the envelope clean-up phase.

(xi) Regarding the source distributions with Galactic longitude, local excesses of sources are encountered in correspondence to spiral arm tangent points or star-forming complexes. A low number ratio between pre-stellar and protostellar sources, evaluated in bins of longitude, found in correspondence to high median surface density in the same bins ($\Sigma > 0.2$ g cm^{-2}) may suggest a short lifetime of high-density clumps in the pre-stellar stage. Despite this, we find a conspicuous number of pre-stellar cores compatible with high-mass star formation, especially in the fourth quadrant.

(xii) No large differences are found between medians of clump evolutionary indicators in the fourth and first quadrants. However, although differences are quite small, median temperature, luminosity over mass ratio, bolometric over sub-mm luminosity ratio and bolometric temperature are larger in the fourth than in the first quadrant.

(xiii) Although the set of distances we adopt does not produce, in some regions of the Galactic plane, a source pattern showing well-definite spiral arms, we made a tentative assignment of sources to spiral arms modelled by Hou et al. (2009). 'On-arm' and 'interarm' populations show no relevant differences either in the pre-stellar over protostellar number ratio or in the median values of the evolutionary indicators. This result could suggest a negligible impact of spiral arms in triggering star formation. However, this result is biased by the uncertainties affecting source distance estimations and consequently association with spiral arms.

(xiv) While temperature and luminosity over mass ratio do not show clear trends as a function of increasing Galactocentric radius, a slightly increasing trend is found for the median bolometric temperature, and a slightly decreasing one for the median surface density.

In conclusion, the aim of this paper is to give a first look at the huge amount of information contained in the Hi-GAL physical catalogue of the inner Galaxy. Papers based on data taken from this catalogue have been already published (Persi et al. 2016; Ragan et al. 2016), as well as observational programmes submitted for (and also partially observed with) ALMA. A number of papers exploiting this catalogue, or aiming at completing it in the outer Galaxy, are in preparation at present, and will contribute to deepen and refine the conclusions of this work.

ACKNOWLEDGEMENTS

The authors thank the anonymous referee for her/his careful reading of the manuscript and insightful comments. This work is part of the VIALACTEA Project, a Collaborative Project under Framework Programme 7 of the European Union, funded under Contract #607380, which is hereby acknowledged. *Herschel* Hi-GAL data processing, map production and source catalogue generation is the result of a multi-year effort, which was initially funded, thanks to Contracts I/038/080/0 and I/029/12/0 from ASI (Agenzia Spaziale Italiana). *Herschel* is an ESA space observatory with science instruments provided by European-led Principal Investigator consortia and with important participation from NASA. PACS has been developed by a consortium of institutes led by MPE

(Germany) and including UVIE (Austria); KUL, CSL, IMEC (Belgium); CEA, OAMP (France); MPIA (Germany); IAPS, OAP/OAT, OAA/CAISMI, LENS, SISSA (Italy); and IAC (Spain). This development has been supported by the funding agencies BMVIT (Austria), ESA-PRODEX (Belgium), CEA/CNES (France), DLR (Germany), ASI (Italy) and CICYT/MCYT (Spain). SPIRE has been developed by a consortium of institutes led by Cardiff University (UK) and including the University of Lethbridge (Canada); NAOC (China); CEA, LAM (France); IAPS, University of Padua (Italy); IAC (Spain); Stockholm Observatory (Sweden); Imperial College London, RAL, UCL-MSSL, UKATC, University of Sussex (UK); and Caltech, JPL, NHSC, University of Colorado (USA). This development has also been supported by national funding agencies: CSA (Canada); NAOC (China); CEA, CNES, CNRS (France); ASI (Italy); MCINN (Spain); Stockholm Observatory (Sweden); STFC (UK); and NASA (USA).

REFERENCES

Aguirre J. E. et al., 2011, ApJS, 192, 4
Ali B. et al., 2010, A&A, 518, L119
Andre P., Ward-Thompson D., Barsony M., 1993, ApJ, 406, 122
André P., Ward-Thompson D., Barsony M., 2000, in Mannings V., Boss A. P., Russell S. S., eds, Protostars and Planets IV. Univ. Arizona Press, Tucson, AZ, p. 59
André P. et al., 2008, A&A, 490, L27
André P. et al., 2010, A&A, 518, L102
Avedisova V., 2000, Baltic Astron., 9, 569
Baldeschi A. et al., 2017, MNRAS, 466, 3682
Bally J., Zinnecker H., 2005, AJ, 129, 2281
Bally J. et al., 2010, A&A, 518, L90
Barnes P. J. et al., 2011, ApJS, 196, 12
Battersby C., Bally J., Jackson J. M., Ginsburg A., Shirley Y. L., Schlingman W., Glenn J., 2010, ApJ, 721, 222
Battersby C. et al., 2011, A&A, 535, A128
Beckwith S. V. W., Sargent A. I., Chini R. S., Guesten R., 1990, AJ, 99, 924
Beltrán M. T. et al., 2013, A&A, 552, A123
Bergin E. A., Tafalla M., 2007, ARA&A, 45, 339
Beuther H., Henning T., Linz H., Krause O., Nielbock M., Steinacker J., 2010, A&A, 518, L78
Beuther H., Kainulainen J., Henning T., Plume R., Heitsch F., 2011, A&A, 533, A17
Billot N. et al., 2011, ApJ, 735, 28
Bontemps S. et al., 2010, A&A, 518, L85
Brand J., Blitz L., 1993, A&A, 275, 67
Bronfman L., Nyman L.-A., May J., 1996, A&AS, 115, 81
Bronfman L., Casassus S., May J., Nyman L.-Å., 2000, A&A, 358, 521
Butler M. J., Tan J. C., 2012, ApJ, 754, 5
Carey S. J., Mizuno D. R., Kraemer K. E., Shenoy S., Noriega-Crespo A., Price S. D., Paladini R., Kuchar T. A., 2008, MIPSGAL v3.0 Data Delivery Description Document (29 August 2008). CalTech, Pasadena, CA
Carey S. J. et al., 2009, PASP, 121, 76
Cesaroni R. et al., 2015, A&A, 579, A71
Chabrier G., 2003, PASP, 115, 763
Chen H., Myers P. C., Ladd E. F., Wood D. O. S., 1995, ApJ, 445, 377
Churchwell E. et al., 2009, PASP, 121, 213
Contreras Y. et al., 2013, A&A, 549, A45
Csengeri T. et al., 2014, A&A, 565, A75
Deharveng L. et al., 2012, A&A, 546, A74
di Francesco J. et al., 2010, A&A, 518, L91
Dobbs C. L., Bonnell I. A., 2007, MNRAS, 376, 1747
Draine B. T., Li A., 2007, ApJ, 657, 810
Dunham M. M., Crapsi A., Evans N. J. II, Bourke T. L., Huard T. L., Myers P. C., Kauffmann J., 2008, ApJS, 179, 249
Dunham M. M. et al., 2014, in Beuther H., Klessen R. S., Dullemond C. P., Henning T., eds. Protostars and Planets VI. Univ. Arizona Press, Tucson, AZ, p. 195
Eden D. J., Moore T. J. T., Plume R., Morgan L. K., 2012, MNRAS, 422, 3178
Eden D. J., Moore T. J. T., Morgan L. K., Thompson M. A., Urquhart J. S., 2013, MNRAS, 431, 1587
Eden D. J., Moore T. J. T., Urquhart J. S., Elia D., Plume R., Rigby A. J., Thompson M. A., 2015, MNRAS, 452, 289
Egan M. P., Shipman R. F., Price S. D., Carey S. J., Clark F. O., Cohen M., 1998, ApJ, 494, L199
Egan M. O., Price S. D., Kraemer K. E., 2003, AAS, 203, 5708
Elia D., Pezzuto S., 2016, MNRAS, 461, 1328
Elia D. et al., 2010, A&A, 518, L97
Elia D. et al., 2013, ApJ, 772, 45
Elia D. et al., 2014, ApJ, 788, 3
Ellsworth-Bowers T. P. et al., 2013, ApJ, 770, 39
Ellsworth-Bowers T. P., Rosolowsky E., Glenn J., Ginsburg A., Evans II N. J., Battersby C., Shirley Y. L., Svoboda B., 2015, ApJ, 799, 29
Enoch M. L., Evans II N. J., Sargent A. I., Glenn J., Rosolowsky E., Myers P., 2008, ApJ, 684, 1240
Fallscheer C. et al., 2013, ApJ, 773, 102
Ferrière K. M., 2001, Rev. Mod. Phys., 73, 1031
Fish V. L., Reid M. J., Wilner D. J., Churchwell E., 2003, ApJ, 587, 701
Fontani F., Beltrán M. T., Brand J., Cesaroni R., Testi L., Molinari S., Walmsley C. M., 2005, A&A, 432, 921
García P., Bronfman L., Nyman L.-Å., Dame T. M., Luna A., 2014, ApJS, 212, 2
Giannetti A. et al., 2013, A&A, 556, A16
Giannini T. et al., 2012, A&A, 539, A156
Ginsburg A., Bressert E., Bally J., Battersby C., 2012, ApJ, 758, L29
Ginsburg A. et al., 2013, ApJS, 208, 14
Green J. A., McClure-Griffiths N. M., 2011, MNRAS, 417, 2500
Griffin M. J. et al., 2010, A&A, 518, L3
Gutermuth R. A., Heyer M., 2015, AJ, 149, 64
Guzmán A. E., Sanhueza P., Contreras Y., Smith H. A., Jackson J. M., Hoq S., Rathborne J. M., 2015, ApJ, 815, 130
Hatchell J., Fuller G. A., 2008, A&A, 482, 855
He Y.-X. et al., 2015, MNRAS, 450, 1926
Hoare M. G. et al., 2012, PASP, 124, 939
Hofner P., Wyrowski F., Walmsley C. M., Churchwell E., 2000, ApJ, 536, 393
Hou L. G., Han J. L., Shi W. B., 2009, A&A, 499, 473
Jackson J. M. et al., 2006, ApJS, 163, 145
Kainulainen J., Beuther H., Henning T., Plume R., 2009, A&A, 508, L35
Kato S., Mizuno N., Asayama S.-i., Mizuno A., Ogawa H., Fukui Y., 1999, PASJ, 51, 883
Kauffmann J., Pillai T., 2010, ApJ, 723, L7
Könyves V. et al., 2010, A&A, 518, L106
Könyves V. et al., 2015, A&A, 584, A91
Krumholz M. R., McKee C. F., 2008, Nature, 451, 1082
Lada C. J., 1987, in Peimbert M., Jugaku J., eds, Proc. IAU Symp. 115, Star Forming Regions. D. Reidel Publishing Co., Dordrecht, p. 1
Lada C. J., Wilking B. A., 1984, ApJ, 287, 610
Larson R. B., 1981, MNRAS, 194, 809
Lawrence A. et al., 2007, MNRAS, 379, 1599
Li J. J. et al., 2012, ApJ, 749, 47
López-Sepulcre A., Cesaroni R., Walmsley C. M., 2010, A&A, 517, A66
Lumsden S. L., Hoare M. G., Urquhart J. S., Oudmaijer R. D., Davies B., Mottram J. C., Cooper H. D. B., Moore T. J. T., 2013, ApJS, 208, 11
Ma B., Tan J. C., Barnes P. J., 2013, ApJ, 779, 79
Makovoz D., Marleau F. R., 2005, PASP, 117, 1113
Martin P. G. et al., 2010, A&A, 518, L105
Martin P. G. et al., 2012, ApJ, 751, 28
Maury A. J., André P., Men'shchikov A., Könyves V., Bontemps S., 2011, A&A, 535, A77
Merello M., Evans II N. J., Shirley Y. L., Rosolowsky E., Ginsburg A., Bally J., Battersby C., Dunham M. M., 2015, ApJS, 218, 1

Molinari S., Pezzuto S., Cesaroni R., Brand J., Faustini F., Testi L., 2008, A&A, 481, 345
Molinari S. et al., 2010a, PASP, 122, 314
Molinari S. et al., 2010b, A&A, 518, L100
Molinari S., Schisano E., Faustini F., Pestalozzi M., di Giorgio A. M., Liu S., 2011, A&A, 530, A133
Molinari S. et al., 2014, in Beuther H., Klessen R. S., Dullemond C. P., Henning T., eds, Protostars and Planets VI. Univ. Arizona Press, Tucson, AZ, p. 125
Molinari S. et al., 2016a, A&A, 591, A149
Molinari S., Merello M., Elia D., Cesaroni R., Testi L., Robitaille T., 2016b, ApJ, 826, L8
Molinaro M. et al., 2016, in Gianluca C., Juan C. G., eds, Proc. SPIE Conf. Ser. Vol. 9913, VIALACTEA Knowledge Base Homogenizing Access to Milky Way Data. SPIE, Bellingham, p. 99130H
Momany Y., Zaggia S., Gilmore G., Piotto G., Carraro G., Bedin L. R., de Angeli F., 2006, A&A, 451, 515
Moore T. J. T. et al., 2015, MNRAS, 453, 4264
Motte F. et al., 2010a, A&A, 518, L77
Motte F. et al., 2010b, A&A, 518, L77
Motte F. et al., 2014, A&A, 571, A32
Mueller K. E., Shirley Y. L., Evans II N. J., Jacobson H. R., 2002, ApJS, 143, 469
Myers P. C., Ladd E. F., 1993, ApJ, 413, L47
Myers P. C., Adams F. C., Chen H., Schaff E., 1998, ApJ, 492, 703
Netterfield C. B. et al., 2009, ApJ, 707, 1824
Nguyen Luong Q. et al., 2011, A&A, 529, A41
Olmi L. et al., 2009, ApJ, 707, 1836
Olmi L. et al., 2013, A&A, 551, A111
Onishi T., Mizuno N., Mizuno A., Fukui Y., NANTEN team, 2005, in Reipurth B., Jewitt D., Keil K., eds, Protostars and Planets V Posters. Univ. Arizona Press, Tucson, p. 8301
Ossenkopf V., Henning T., 1994, A&A, 291, 943
Paladini R. et al., 2012, ApJ, 760, 149
Pekruhl S., Preibisch T., Schuller F., Menten K., 2013, A&A, 550, A29
Peretto N., Fuller G. A., 2010, ApJ, 723, 555
Peretto N. et al., 2010, A&A, 518, L98
Persi P., Tapia M., Roth M., Elia D., López-Vázquez J. A., 2016, MNRAS, 459, 1946
Pezzuto S. et al., 2012, A&A, 547, A54
Piazzo L., Ikhenaode D., Natoli P., Pestalozzi M., Piacentini F., Traficante A., 2012, IEEE Trans. Image Process., 21, 3687
Pilbratt G. L. et al., 2010, A&A, 518, L1
Poglitsch A. et al., 2010, A&A, 518, L2
Polychroni D. et al., 2013, ApJ, 777, L33
Preibisch T., Ossenkopf V., Yorke H. W., Henning T., 1993, A&A, 279, 577
Purcell C. R. et al., 2013, ApJS, 205, 1
Ragan S. E., Bergin E. A., Gutermuth R. A., 2009, ApJ, 698, 324
Ragan S. et al., 2012, A&A, 547, A49
Ragan S. E., Henning T., Beuther H., 2013, A&A, 559, A79
Ragan S. E., Moore T. J. T., Eden D. J., Hoare M. G., Elia D., Molinari S., 2016, MNRAS, 462, 3123
Reid M. A., Wilson C. D., 2005, ApJ, 625, 891
Reid M. A., Wilson C. D., 2006, ApJ, 644, 990
Reid M. A., Wadsley J., Petitclerc N., Sills A., 2010, ApJ, 719, 561
Rodgers A. W., Campbell C. T., Whiteoak J. B., 1960, MNRAS, 121, 103
Roman-Duval J., Jackson J. M., Heyer M., Johnson A., Rathborne J., Shah R., Simon R., 2009, ApJ, 699, 1153
Rosolowsky E. et al., 2010, ApJS, 188, 123
Russeil D., 2003, A&A, 397, 133
Russeil D. et al., 2011, A&A, 526, A151
Sadavoy S. I. et al., 2013, ApJ, 767, 126
Salpeter E. E., 1955, ApJ, 121, 161
Saraceno P., Andre P., Ceccarelli C., Griffin M., Molinari S., 1996, A&A, 309, 827
Schisano E. et al., 2014, ApJ, 791, 27
Schneider N. et al., 2012, A&A, 540, L11
Schuller F. et al., 2009, A&A, 504, 415
Shirley Y. L., Evans N. J. II, Young K. E., Knez C., Jaffe D. T., 2003, ApJS, 149, 375
Smith M. D., 2014, MNRAS, 438, 1051
Smith R. J., Clark P. C., Bonnell I. A., 2008, MNRAS, 391, 1091
Spezzi L. et al., 2013, A&A, 555, A71
Stetson P. B., 1987, PASP, 99, 191
Stil J. M. et al., 2006, AJ, 132, 1158
Strafella F. et al., 2010, ApJ, 719, 9
Strafella F. et al., 2015, ApJ, 798, 104
Stutzki J., Bensch F., Heithausen A., Ossenkopf V., Zielinsky M., 1998, A&A, 336, 697
Svoboda B. E. et al., 2016, ApJ, 822, 59
Tackenberg J. et al., 2012, A&A, 540, A113
Tan J. C., 2005, in Kumar M. S. N., Tafalla M., Caselli P., eds, Cores to Clusters: Star Formation with Next Generation Telescopes. Springer Science+Business Media, Berlin, p. 87
Tapia M., Persi P., Roth M., Elia D., Molinari S., Saldaño H. P., Gómez M., 2014, MNRAS, 437, 606
Traficante A. et al., 2011, MNRAS, 416, 2932
Traficante A., Fuller G. A., Peretto N., Pineda J. E., Molinari S., 2015, MNRAS, 451, 3089
Urquhart J. S. et al., 2009, A&A, 507, 795
Urquhart J. S., Figura C. C., Moore T. J. T., Hoare M. G., Lumsden S. L., Mottram J. C., Thompson M. A., Oudmaijer R. D., 2014a, MNRAS, 437, 1791
Urquhart J. S. et al., 2014b, A&A, 568, A41
Vallée J. P., 2008, AJ, 135, 1301
Veneziani M. et al., 2013, A&A, 549, A130
Veneziani M. et al., 2017, A&A, 599, A7
Wang S., Gao J., Jiang B. W., Li A., Chen Y., 2013, ApJ, 773, 30
Wienen M. et al., 2015, A&A, 579, A91
Wilcock L. A. et al., 2012a, MNRAS, 422, 1071
Wilcock L. A. et al., 2012b, MNRAS, 424, 716
Wright E. L. et al., 2010, AJ, 140, 1868
Xu Y. et al., 2016, Sci. Adv., 2, e1600878
Young K. E. et al., 2005, ApJ, 628, 283
Yun J. L., Elia D., Djupvik A. A., Torrelles J. M., Molinari S., 2015, MNRAS, 452, 1523
Zahorecz S., Jimenez-Serra I., Wang K., Testi L., Tóth L. V., Molinari S., 2016, A&A, 591, A105

APPENDIX A: DESCRIPTION OF PHYSICAL CATALOGUE

The Hi-GAL physical catalogue for the inner Galaxy is hosted in the VIALACTEA Knowledge Base (VLKB, Molinaro et al. 2016), and is arranged in two tables (high- and low-reliability SEDs) both containing the same columns, defined as follows:

(i) Column [1], *ID*: running number (starting from 1 in the high-reliability table and continuing in the low-reliability one).

(ii) Column [2], *DESIGNATION*: string composed by 'HIGAL', 'BM' (which stays for 'band-merged') and Galactic coordinates of the sources, chosen as the coordinates of the shortest wavelength available Hi-GAL counterpart.

(iii) Columns [3], *GLON*, and [4], *GLAT*: Galactic longitude and latitude, respectively, assigned to the source, chosen as the coordinates of the shortest wavelength available Hi-GAL counterpart.

(iv) Columns [5], *RA*, and [6], *DEC*: the same as in columns [3] and [4], respectively, but for source equatorial coordinates.

(v) Column [7], *DESIGNATION_70*: designation of the PACS 70-μm counterpart (if available), as defined in the catalogue of Molinari et al. (2016a). The null string (in the case of a missing counterpart at this band) is '-'.

(vi) Column [8], *F70*: flux density (hereafter flux) of the PACS 70-μm counterpart (if available), in Jy, as quoted by Molinari et al. (2016a). The null value is 0.

(vii) Column [9], *DF70*: uncertainty associated with the flux in column [8], as quoted by Molinari et al. (2016a). The null value is 0.

(viii) Column [10], *F70_TOT*: sum of fluxes of all PACS 70-μm counterparts (if available) lying inside the half-maximum ellipse of the source detected by CuTEx in the SPIRE 250-μm maps. By definition, $F_{70,\,\mathrm{tot}} \geq F_{70}$. The null value is 0. This is the flux at 70 μm actually used to estimate the source bolometric luminosity (Section 4) and temperature (Section 7.2).

(ix) Column [11], *DF70_TOT*: uncertainty associated with the flux in column [10], obtained as the quadratic sum of uncertainties on single fluxes. The null value is 0.

(x) Column [12], *F70_ADD*: flux of the closest PACS 70-μm counterpart (if available) found through targeted source extraction at a detection threshold lower than in Molinari et al. (2016a) where $F_{70,\,\mathrm{tot}} = 0$ (column[11]), as described in Section 3.5. The null value is 0.

(xi) Column [13], *DF70_ADD*: uncertainty associated with the flux in column [12]. The null value is 0.

(xii) Column [14], *F70_ADD_TOT*: sum of fluxes of all PACS 70-μm counterparts (if available) found through targeted source extraction at a detection threshold lower than in Molinari et al. (2016a), where $F_{70,\,\mathrm{tot}} = 0$, and lying inside the ellipse at 250 μm (as for column [10]). The null value is 0. This is the flux at 70 μm actually used to estimate the source bolometric luminosity and temperature where $F_{70,\,\mathrm{tot}} = 0$.

(xiii) Column [15], *DF70_ADD_TOT*: uncertainty associated with the flux in column [14], estimated as for column [11]. The null value is 0.

(xiv) Column [16], *ULIM_70*: 5σ upper limit in the PACS 70-μm band, estimated where both $F_{70,\,\mathrm{tot}} = 0$ (column [10]) and $F_{70\mathrm{add},\,\mathrm{tot}} = 0$ (column[14]).

(xv) Columns [17], *DESIGNATION_160*, [18], *F160*, and [19], *DF160*: the same as columns [7], [8] and [9], respectively, but for the PACS 160-μm band.

(xvi) Columns [20], *F160_ADD*, and [21], *DF160_ADD*: the same as columns [12] and [13], respectively, but for the PACS 160-μm band.

(xvii) Column [21], *ULIM_160*: 5σ upper limit in the PACS 160-μm band, estimated where both $F_{160} = 0$ (column [18]) and $F_{160\mathrm{add}} = 0$ (column [20]).

(xviii) Columns [22], *DESIGNATION_250*, [23], *F250*, and [24], *DF250*: the same as columns [7], [8] and [9], respectively, but for the SPIRE 250-μm band.

(xix) Columns [25], *DESIGNATION_350*, [26], *F350*, and [27], *DF350*: the same as columns [7], [8] and [9], respectively, but for the SPIRE 350-μm band.

(xx) Column [28], *FSC350*: SPIRE 350-μm flux 'scaled' as mentioned in Section 3.1. Further details on the method are provided, e.g. in Giannini et al. (2012). Scaling is not performed when the source size differs by less than a factor of $\sqrt{2}$ from the instrumental beam size at this wavelength.

(xxi) Column [29], *DFSC350*: uncertainty associated with the flux in column [28].

(xxii) Columns [30], *DESIGNATION_500*, [31], *F500*, [32], *DF500*, [33], *FSC500*, and [34], *DFSC500*: the same as columns [25], [26], [27], [28] and [29], respectively, but for the SPIRE 500-μm band.

(xxiii) Column [35], *DESIGNATION_21*: designation of the MSX 21-μm counterpart (if available), as defined in the MSX point source catalogue. The null string (in the case of a missing counterpart at this band) is '-'.

(xxiv) Column [36], *F21*: flux of the closest MXS 21-μm counterpart (if available within the adopted matching radius), in Jy. The null value is 0.

(xxv) Column [37], *DF21*: uncertainty associated with the flux in column [36]. The null value is 0.

(xxvi) Column [38], *F21_TOT*: sum of fluxes of all MXS 21-μm counterparts (if available) lying inside the ellipse at 250 μm (as done for column [10]). The null value is 0.

(xxvii) Column [39], *DF21_TOT*: uncertainty associated with the flux in column [38], computed as for column [11]. The null value is 0.

(xxviii) Columns [40], *DESIGNATION_22*, [41], *F22*, [42], *DF22*, [43], *F22_TOT*, and [44], *DF22_TOT*: the same as columns [35], [36], [37], [38] and [39], respectively, but for the *WISE* 22-μm band.

(xxix) Column [45], *DESIGNATION_24*: designation of the MSX 24-μm counterpart (if available). A string beginning with 'MG' identifies a source taken from the catalogue of Gutermuth & Heyer (2015), while a string beginning with 'D' identifies a source specifically detected in this work, (cf. Section 3.3). Furthermore, a lack of a source due to saturation is identified with the 'satutared' string.

(xxx) Columns [46], *F24*, [47], *DF24*, [48], *F24_TOT*, and [49], *DF24_TOT*: the same as columns [36], [37], [38] and [39], respectively, but for the MIPSGAL 24-μm band. In column [46], in the case of saturation (see column [45]), a null value −999 is quoted.

(xxxi) Column [50], *DESIGNATION_870*: designation of the ATLASGAL 870-μm counterpart (if available). A string beginning with 'G' identifies a source taken from the catalogue of Csengeri et al. (2014), while the string 'CuTEx' identifies a source specifically detected for this work, as explained in Section 3.3. The null string (in the case of a missing counterpart at this band) is '-'.

(xxxii) Columns [51], *F870*, and [52], *DF870*: the same as columns [46] and [47], respectively, but for the ATLASGAL 870-μm band.

(xxxiii) Column [52], *DESIGNATION_1100*: designation of the BGPS 1100-μm counterpart (if available), as defined in the BGPS catalogue (Ginsburg et al. 2013). The null string (in the case of a missing counterpart at this band) is '-'.

(xxxiv) Columns [53], *F1100*, and [54], *DF1100*: the same as columns [46] and [47], respectively, but for the BOLOCAM 1100-μm band.

(xxxv) Columns [54], *DFWHM250*: circularized and (if the circularized size exceeds the instrumental beam size by a factor of $\sqrt{2}$) beam-deconvolved size of the sources as estimated by CuTEx in the 250-μm band, in arcseconds.

(xxxvi) Columns [55], *DIST*: kinematic distance of the source, in pc (Russeil et al. 2011). In the case of distance ambiguity, it represents the final choice between the 'near' and the 'far' estimates, reported in the next two columns. The null value, in the case of an unavailable distance estimate, is 0.

(xxxvii) Columns [56], *NEAR_DIST*, and [57], *FAR_DIST*: 'near' and 'far' kinematic distance estimates of the source, in pc. The null value is 0.

(xxxviii) Column [58], *DIST_FLAG*: flag indicating the quality of the distance 'near'/'far' ambiguity solution. If an external indicator is used to take the decision, the flag is 'G'; otherwise, it is

'B', and the 'far' distance is assigned to the source by default (see Section 3.4). The null value, in the case of an unavailable distance estimate, is '-'.

(xxxix) Column [59], *DIAM*: source linear diameter, in pc, obtained by combining columns [54] and [55].

(xl) Column [60], *M_LARS*: Larson's mass, in solar masses, evaluated as described in Section 3.5. The null value, in the case of an unavailable distance, is 0.

(xli) Column [61], *FIT_TYPE*: flag indicating if the expression of the grey body fitted to the source SED is given by equation (1) ('thick' case, 'Tk' flag) or equation (4) ('thin' case, 'Tn' flag).

(xlii) Column [62], *EVOL_FLAG*: flag indicating the evolutionary classification of the source (0: starless unbound; 1: prestellar; 2: protostellar).

(xliii) Column [63], *MASS*: clump total mass, in units of solar masses, derived by fitting a grey body to the source SED. In the case of an unavailable distance, the fit is performed anyway assuming a virtual distance of 1 kpc, and the corresponding mass is quoted as a negative value.

(xliv) Column [64], *DMASS*: uncertainty associated with the mass in column [63].

(xlv) Column [65], *TEMP*: dust temperature of the clump, in K, derived from the grey-body fit.

(xlvi) Column [66], *DTEMP*: uncertainty associated with the temperature in column [65].

(xlvii) Column [67], *LAM_0_TK*: value of λ_0 (see equation 1), in μm, derived from the grey-body fit. The null value, corresponding to the value 'Tn' of the flag FIT_TYPE, is 0.

(xlviii) Column [68], *L_BOL*: bolometric luminosity, in units of solar luminosity, estimated as described in Section 4. As in the case of the mass, for sources devoid of a distance estimate, a luminosity corresponding to the virtual distance of 1 kpc is calculated and quoted as a negative value.

(xlix) Column [69], *LRATIO*: ratio between the bolometric luminosity in Column [67] and its fraction computed over the range $\lambda \geq 350$ μm.

(l) Column [70], *T_BOL*: bolometric temperature, in K, calculated based on equation (5).

(li) Column [71], *SURF_DENS*: surface density, in g cm^{-2}, calculated by dividing the mass in Column [63] by the area of the circle with the diameter in Column [59]. Where the distance is unavailable, this quantity can be evaluated anyway, assuming a whatever virtual distance for intermediate calculations, and starting from Column [54] instead of [59].

APPENDIX B: POSSIBLE MID-INFRARED ASSOCIATIONS OF STARLESS HI-GAL SOURCES

In Section 3.5, we defined the classification of Hi-GAL sources into starless and protostellar, based on the absence or the presence of a detection at 70 μm, respectively. For the former ones, possible associations with MIR point sources are considered spurious, and are not taken into account for deriving the bolometric luminosity and temperature. To ascertain how reliable is this assumption, we performed two different tests.

The first test consisted of checking the impact of possible foreground MIR point sources on the incidence of chance associations with Hi-GAL sources. We chose eight Hi-GAL 4×1.4-deg^2 fields, centred on longitudes $\ell = -60^\circ$, -40°, -20°, -10°, 10°, 20°, 40° and 60°, respectively, and latitude $b = 0^\circ$, so well inside the PACS–SPIRE common science area. First, we identified all sources having a detection at 160 μm and at 21 and/or 22 and/or 24 μm, but with no detection at 70 μm, i.e. the sub-sample of the entire starless population that might be misclassified in the case of a too faint flux at 70 μm. We further restricted the investigated box area to the limits given by the maximum and minimum of longitude and latitude of the selected sources, and counted the total amount $N_{\rm MIR}$ of MSX, *WISE* and MIPSGAL sources falling within such area. Then we randomly dispersed $N_{\rm MIR}$ points across the area, and performed the association with the selected starless Hi-GAL sources, as described in Section 3.3. Finally, for each field we compared the number of associations $N_{\rm rnd}$ found with that of the actual associations between the selected Hi-GAL starless sources and MIR catalogue sources ($N_{\rm cat}$); in Fig. B1, red circles represent the obtained statistics, with $N_{\rm rnd}/N_{\rm cat}$ being >75 per cent in all cases. This suggests that most of the associations found between starless Hi-GAL sources and MIR catalogues can be explained as a chance alignment along the line of sight.

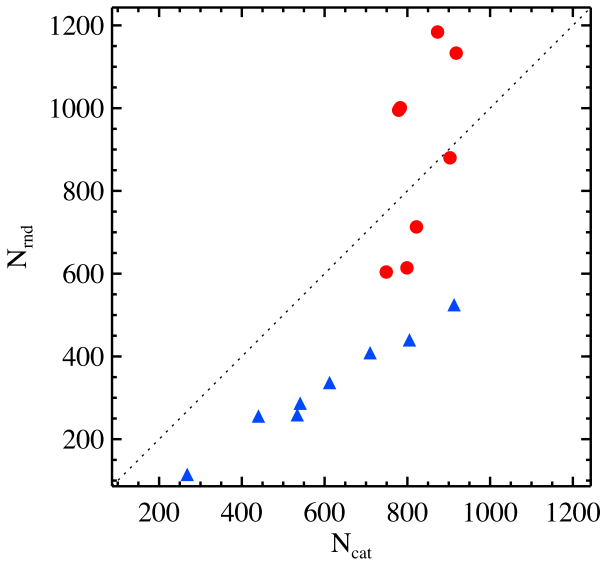

Figure B1. Comparison between the number $N_{\rm cat}$ of Hi-GAL sources (in each of eight different test fields, see text) found to be associated with MIR counterparts (being the total number of MIR sources $N_{\rm MIR} > N_{\rm cat}$) and the number $N_{\rm rnd}$ of associations established between the same Hi-GAL sources and $N_{\rm MIR}$ positions randomly dispersed in the same field. Red circles represent the statistics of starless sources detected at 160 μm, while blue triangles represent protostellar sources.

On the other hand, MIR counterparts found for protostellar sources should be considered as a more genuine effect. In fact, repeating the procedure described above on protostellar sources found in the test fields, we find an association rate smaller than 60 per cent in all cases, suggesting that, unlike the starless case, the real spatial disposition of MIR sources follows more closely the one of Hi-GAL protostellar objects, so cases of chance associations are expected to be less frequent.

The second test directly involves the photometry of the sources. The question arises whether the failed detection at 70 μm is caused by the fact that the SED is in the Wien regime of the grey body at this wavelength, emitting a too small flux to be detected with PACS, or it is due to lack of sensitivity, such that the emission at 70 μm is in excess of that expected from a grey body at a given temperature, albeit remaining below the flux threshold of the instrument.

To investigate this issue, first, we plot F_{70} versus F_{24} for protostellar sources (Fig. B2). An overall correlation between the two

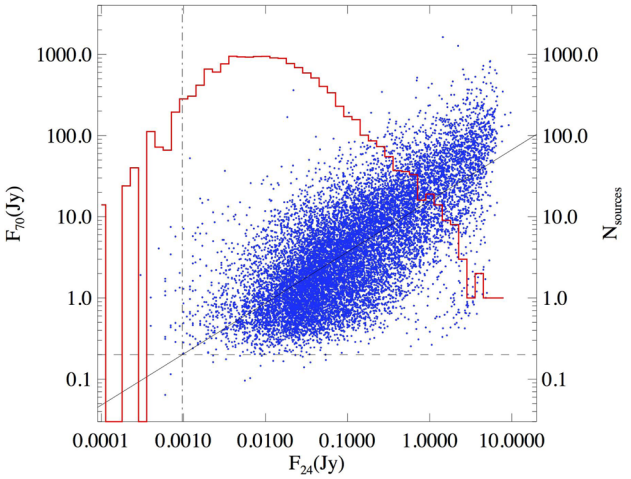

Figure B2. Scatter plot of flux at 70 μm versus flux at 24 μm for protostellar sources of the Hi-GAL catalogue provided with both these fluxes (blue dots). The solid line represents the power-law fit to the displayed points (see text). The horizontal black line represents the limit flux of 0.2 Jy at 70 μm, while the vertical dot–dashed line corresponds to the abscissa of the intersection of the previous line with the power-law fit. The red line is the histogram of flux at 24 μm of sources with detection at 160 μm and no detection at 70 μm, plotted with respect to the *y*-axis reported on the right-hand side of the box.

fluxes is seen (cf. with Spitzer literature, e.g. Young et al. 2005; Strafella et al. 2010), so that for this class of objects low PACS fluxes are expected in correspondence to low MIPS fluxes. Fitting a power law $F_{70} = a\,(F_{24})^b$ to the plotted data gives $a = 15.7 \pm 0.01$ and $b = 0.63 \pm 0.01$. Most of our sources have $F_{70} > 0.2$ Jy, so that the corresponding F_{24} suggested by the fit would be 0.001 Jy. This implies that, in principle, a source with $F_{24} > 0.001$ Jy should be observable with PACS at 70 μm as well. Nevertheless, only the 3 per cent of sources detected at 24 and 160 μm and not detected at 70 μm (histogram in Fig. B2) have $F_{24} < 0.001$ Jy, while for the rest a counterpart at 70 μm, according to the general trend of the other sources, should be detectable. Even increasing, to be more conservative, the threshold on F_{70} to the 90 per cent completeness limit for this band quoted by Molinari et al. (2016a), namely ∼0.5 Jy, only 25 per cent of MIPS sources would be fainter than the corresponding limit flux $F_{24} = 0.004$ Jy, leaving the remaining ones to be likely chance associations.

We conclude that both tests discourage to consider a positional match between a Hi-GAL source undetected at 70 μm and an MIR source as a genuine physical association in most cases. It is noteworthy that in literature, before the release of *Herschel* catalogues, the pre-stellar versus protostellar nature of sub-mm sources was ascertained just through a simple spatial association with MIR counterparts, hence suffering from possible chance alignment contamination (e.g. Csengeri et al. 2014), all the more considering the large gap in wavelength between the two bands associated ($\lambda \sim 20$ μm to $\lambda \geq 870$ μm).

APPENDIX C: DISTANCE BIAS ON SOURCE PROPERTY ESTIMATION AND INTERPRETATION

Whereas in studying a single star forming region or a cloud complex it is possible to assume a single global distance estimate for its compact source population, a Galactic plane survey such as Hi-GAL inevitably contains an extraordinary variety of distances superposed along the same line of sight. In Section 6.1, we already illustrated how such a variety produces a large spread of source physical sizes corresponding to the angular extent of the compact sources, in turn, implying substantial consequences on their structural classification. Other source physical properties, however, may turn out to be strongly biased by distance effects. A systematic study of these effects will be published in Baldeschi et al. (2017). Here we limit ourselves to a few considerations related to this issue.

C1 Source confusion and classification

The first issue originates from the simple concept of perspective confusion of two (or more) sources with a given physical separation, as their heliocentric distance increase, so that their angular separation decreases accordingly. Keeping in mind the classification of protostellar versus starless sources introduced in Section 3.5, one can imagine the basic case in which two sources, quite close to each other in the sky and belonging to these two different classes, are virtually placed at an increasing heliocentric distance and 're-observed', until they get confused at the *Herschel* resolution. The 70-μm flux determining the protostellar classification of the former source would be, in this case, assigned to the new unresolved source, including also the original starless companion, making it globally flagged as a protostellar. On one hand, this classification would remain true, in principle, as such a structure, in fact, would have a protostellar content. On the other hand, the mass actually involved in the star formation activity would be (even significantly) smaller than the value quoted for the entire clump mass. This would result, at large distances, in an overestimate of the mass assigned to protostellar structures (see also Hatchell & Fuller 2008).

To try to quantify this effect, we performed a simple test, considering all the sources of our Hi-GAL catalogue located at $d < 4$ kpc, and ideally moved all of them at a larger distance d', estimating the corresponding decrease of their mutual angular separations. Given a pair of sources i and j, located at their original distances d_i and d_j and separated in the sky by an angle φ_0, if they are virtually moved away to a distance $d' > \max(d_i, d_j)$, the new simulated angular separation would become

$$\varphi' = \varphi_0 \frac{(d_1 + d_2)}{2d'} \,. \tag{C1}$$

Probing virtual distances in steps of 1 kpc, starting from $d' = 5$ kpc, and assuming that two (or more) sources get confused when their mutual angular separation becomes smaller than the SPIRE beam at 250 μm (i.e. for $\varphi' < 18$ arcsec), a trend for the ratio (both in number and in total mass) of sources classified as protostellar over the whole source sample has been estimated.

An increment of such fractions is clearly visible in both panels of Fig. C1 (top for the number ratio and bottom for the mass ratio). A linear best fit suggests a slope of 0.005 kpc^{-1} for the protostellar fraction in number. This trend can be used to correct global properties (as, for instance, the SFR) that sensitively depend on the estimate of the protostellar population. Indeed, in Fig. C1, we displayed the same quantity also for the real population of sources, i.e. the protostellar fraction for sources of our catalogue encountered at the probed distances (i.e. located within bins of width 1 kpc, centred on the various values of d'). The observed behaviour in this case is not as smooth as in the simulated case since it depends on peculiar environments encountered throughout the plane in the considered distance bin. However, a generally increasing trend is found, as expected, for the number ratio.

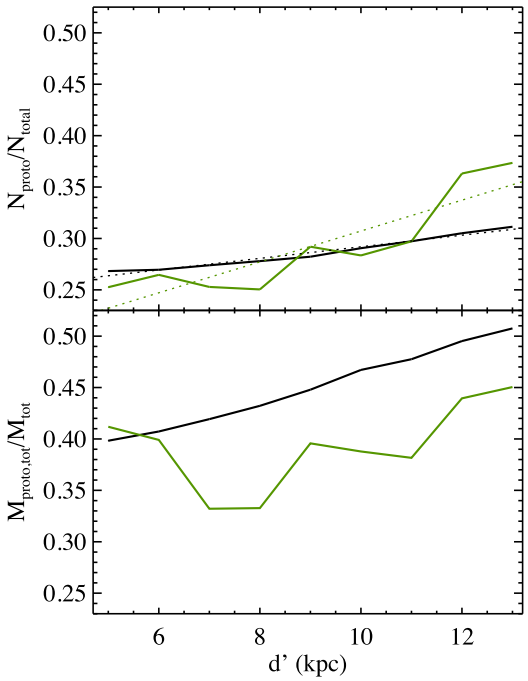

Figure C1. Distance bias affecting the estimate of the global fraction of protostellar sources, both in number (top panel) and in mass (bottom panel). All the Hi-GAL sources located within $d = 4$ kpc have been virtually moved to larger distances, starting from $d' = 5$ kpc, and their mutual separation re-evaluated accordingly. Sources getting confused after this operation define a new unresolved source that assumes a protostellar character if at least one of its original components was protostellar; the new mass is calculated simply as the sum of the masses of the original sources. Top panel: black solid line – fraction of protostellar sources over the total amount of sources, as a function of the new simulated distance, black dotted line – linear best fit of the previous one, green solid line – the same quantity as calculated for the real Hi-GAL sources encountered at the considered distances (in bins 1 kpc wide, centred at multiples of 1 kpc) and green dotted line – linear best fit to the previous one. Bottom panel: The solid lines are the same as in the top panel, but for the protostellar fraction in mass.

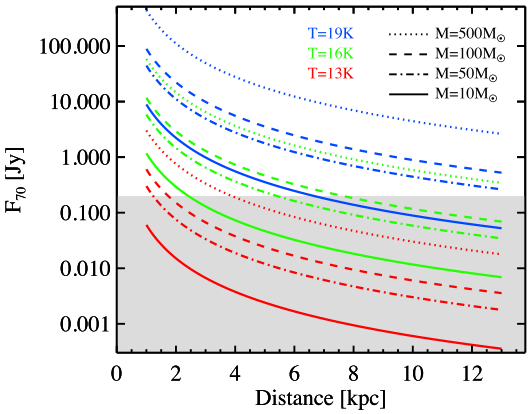

Figure C2. Decrease of the grey-body flux at 70 μm (equation 4) for a set of masses and temperatures (dust opacity parameters are those used in this paper), as a function of heliocentric distance. The correspondence between the three probed temperatures and line colours, and the one between the four probed masses and the line style are shown in the legends in the upper part of the plot. The grey-shaded area, bordered on the top on the assumed PACS sensitivity limit of 0.2 Jy at 70 μm, corresponds to the condition in which the grey-body source is not expected to be detected with *Herschel* in Hi-GAL. Considering, for example, a real protostellar source emitting a flux 10 times larger than the one expected from the grey body that best fits the SED at $\lambda \geq 160$ μm, the curves plotted for 100 and 500 $M_\odot$ would assume in this case the role of those plotted for 10 and 50 $M_\odot$, respectively, to assess the detectability of such source.

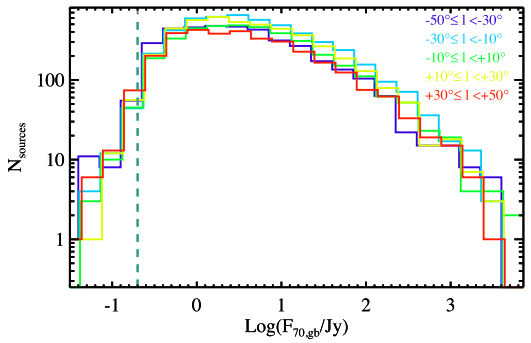

Figure C3. Distributions of 70 μm fluxes used in this paper, obtained separately over Galactic longitude bins of width 20° (the bins are reported at the top right-hand side of the plot, together with the bin–colour correspondence). The assumed PACS sensitivity limit of 0.2 Jy at 70 μm is reported as a vertical grey dashed line.

The observed trend of the mass fraction with the distance, instead, is not clearly increasing (Fig. C1, bottom panel), suggesting that it cannot be treated simply by adding up the masses of the single sources that are going to be merged, since the SED shape (determined by the peak position) of the single sources and the one of the resulting merged source can differ remarkably. Indeed, the resulting mass of the merged source would be the sum of the original masses only if all the original SEDs corresponded to the same temperature.

As already mentioned in Section 3.5, the confusion effect discussed above is in competition with the possible inability of detecting emission at 70 μm from distant and relatively small protostellar clumps, leading to their misclassification as starless sources. In Fig. C2, we propose a simple exercise to show how the grey-body flux at 70 μm, obtained with equation (4) by exploring a grid of values of mass and temperature and using the same dust parameters as reported in Section 4, decreases as a function of source heliocentric distance. We compare these trends with the typical PACS sensitivity limit at this band found in our catalogue, which mildly depends on the line of sight and we assume to be 0.2 Jy, as indicated by Fig. B2. To better investigate a possible dependence of this limit on the Galactic longitude (although Molinari et al. 2016a have already shown that the PACS 70-μm band is the least affected by this effect among the *Herschel* bands), in Fig. C3 we plot the distributions of the 70-μm fluxes used in this paper, built for five 20°-wide different chunks of longitude. For all the five histograms, the bin containing the 0.2 Jy flux is the smallest containing a statistically significant ($N > 10$) number of sources. With respect to this value, in Fig. C2 one sees that a grey body with $M \leq 50\,M_\odot$ and $T \leq 16$ K could not be detected at $d \gtrsim 5$ kpc, while only more favourable parameter combinations (such as, for example, $M \geq 500\,M_\odot$ and $T \geq 16$ K, or $M \geq 50\,M_\odot$ and $T > 19$ K) can remain detectable up to $d = 13$ kpc, a value that is representative of very far objects in our catalogue. Clearly, in the approach followed in this paper, consisting of modelling the portion of the SED at $\lambda \geq 160$ μm with a grey body and the flux observed at 70 μm ($F_{70,\,\mathrm{obs}}$) as a simple upper limit to better constrain the fit, this flux is expected to be in excess

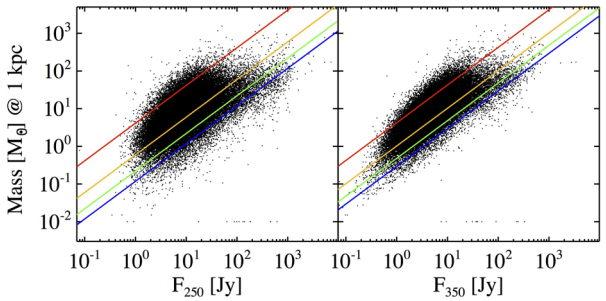

Figure C4. Left-hand panel: relation between grey-body mass and flux at 250 μm for all the sources included in the Hi-GAL physical catalogue. The same relation for a grey body is represented with solid lines for four different temperatures: 10 (red), 15 (orange), 20 (green) and 25 K (blue), respectively. Right-hand panel: the same as in the left-hand panel, but for the flux at 350 μm.

with respect to the grey body ($F_{70,\,\mathrm{gb}}$) best fitting the SED at longer wavelengths. Obviously, this adds a further degree of freedom, so that, for example, one can review the curves plotted in Fig. C2 for the case $M = 500\,\mathrm{M}_\odot$ as those of a source with $M = 50\,\mathrm{M}_\odot$ and $F_{70,\,\mathrm{obs}}/F_{70,\,\mathrm{gb}} = 10$, and so on (we estimate that, for sources present in our catalogue, $F_{70,\,\mathrm{obs}}/F_{70,\,\mathrm{gb}} < 10$ is found in around half of the cases in which $F_{70,\,\mathrm{obs}}$ is available). In conclusion, due to the difficulty in describing $F_{70,\,\mathrm{obs}}$ through a simple model, it is not possible to predict accurately its value starting from the rest of the SED; nevertheless, we expect that a minor but significant fraction of relatively low mass (and/or low temperature) clumps observed at large distances and flagged as starless sources are actually misclassified due a selection effect on the flux at 70 μm.

C2 Mass completeness limits

A discussion of the mass completeness limits for the Hi-GAL sources requires as a first step to identify the most suitable band for estimating masses. Intuitively, wavelengths at which the emission is optically thin so that the integrated flux can be considered proportional to the amount of matter in the clump should be taken into account. The 500-μm band might be the preferred one, but according to the constraints stated in Section 3.1, the flux at this band may not be present in all the considered SEDs, while fluxes at 250 and 350 μm are always present by construction. In Fig. C4, we show the relation between the masses of the catalogue sources and their fluxes at these two bands; to remove the dependence on the distance, the masses have been scaled to the same 'virtual' distance $d_\mathrm{v} = 1$ kpc, through a factor $(d_\mathrm{v}/d)^2$ (or, for sources having no kinematic distance estimate, imposing their distance to be just d_v). Of course, from the analytic point of view, such relation is expected to depend on the temperature, so that also lines corresponding to grey bodies at different temperatures and $\beta = 2$ are overplotted. As expected, the level of spread is smaller (than a tighter correlation is found) in the mass versus F_{350} plot, which we adopt hereafter for the following analysis of the completeness limit.

Molinari et al. (2016a) provided 90 per cent completeness limits for their photometric catalogues at all the five Hi-GAL bands, subdivided by tile. Thus, given a completeness limit $F_{\mathrm{compl},\,350}$ at 350 μm (as a function of the considered tile, so, roughly, of the Galactic longitude), the 90 per cent mass completeness limit will depend on the source temperature (according to the grey-body law) and on its distance (being M_compl proportional to d^2). Collapsing all the involved constants and unit conversion factors, such dependency can

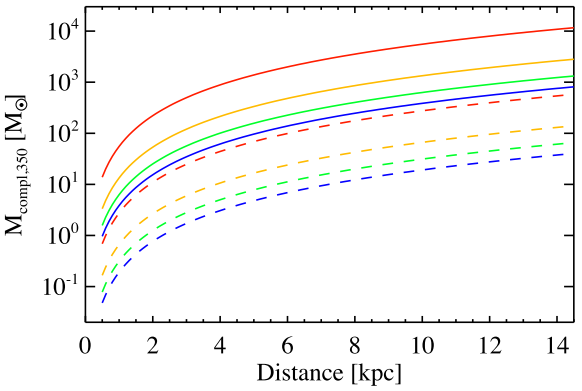

Figure C5. Curves of the 90 per cent mass completeness limit based on the photometry at 350 μm, as a function of the source distance, according to equation (C2). Two values of $F_{\mathrm{compl},\,350}$ are probed (see text): Solid and dashed curves correspond to 13.08 and 0.65 Jy, respectively. Finally, four values of the temperature parameters are probed, namely the same as in Fig. C4, represented using the same colour encoding.

be condensed as

$$\frac{M_\mathrm{compl}(T,d)}{\mathrm{M}_\odot} = 0.0705 \left(\frac{F_{\mathrm{compl},350}}{\mathrm{Jy}}\right)\left(\frac{d}{\mathrm{kpc}}\right)^2 \times \left(\exp\left(\frac{41.1094}{(T/\mathrm{K})}\right) - 1\right). \quad \text{(C2)}$$

In Fig. C5, the behaviour of the mass completeness limit based on equation (C2) is reported, showing how it varies as a function of the distance for two values of $F_{\mathrm{compl},\,350}$, namely the maximum and the minimum ones found by Molinari et al. (2016a) in their Hi-GAL completeness analysis (13.08 and 0.65 Jy, respectively), and for four temperatures between 10 and 25 K. Using the Hi-GAL physical catalogue, therefore, will require to take into account such mass completeness limits.

APPENDIX D: CLUMP PROPERTY CONSISTENCY WITH RESPECT TO PREVIOUS SURVEYS

A blind comparison between our clump property catalogue and the results of previous surveys of the Galactic ISM can turn out to be misleading if no attention is paid to the assumptions such catalogues are built on. The main one is the definition itself of the source typology, in turn, depending on the characteristics of the exploited observations (wavelength domain, tracer, resolution, sensitivity, etc.).

We reaffirm here that this paper deals with the properties of *Herschel* compact sources (i.e. with an angular extent no larger than a few tens of arcsec) whose SEDs are eligible for modified blackbody fit at $\lambda \geq 160\,\mu$m. Depending on the distance, these sources can correspond to pre-stellar or protostellar cores, or (in the most likely case) to larger clumps, or even to entire clouds (Section 6.1). The wavelength range we consider for the grey-body fit allows us to obtain global/average properties of the cold envelope component of the sources. Instead, for obtaining the bolometric luminosity, we also consider fluxes at shorter wavelengths, to take into account the emission from the possible protostellar content of the Hi-GAL source. We finally recall that, through appropriate assumptions and operations (flux scaling), we estimate the source properties as referred to a volume corresponding to the deconvolved source size observed at 250 μm.

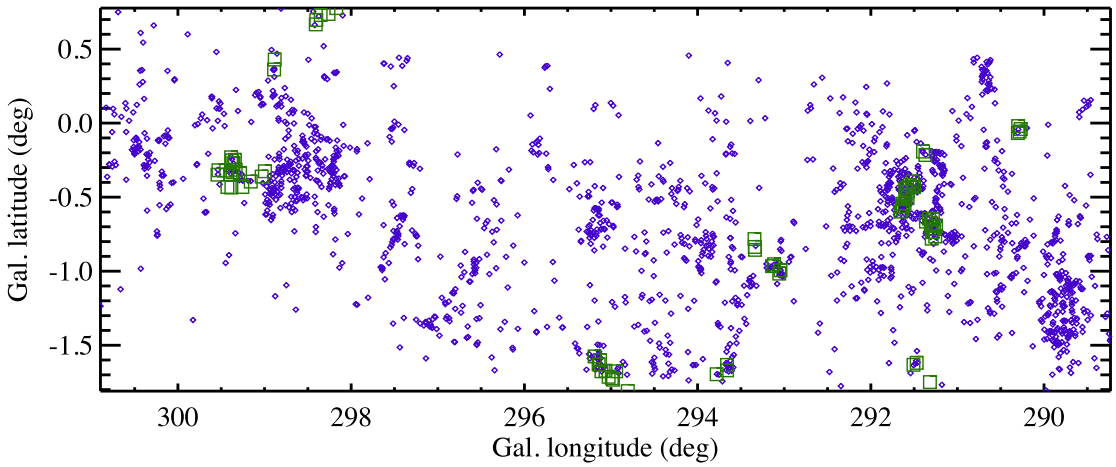

Figure D1. Spatial disposition of Hi-GAL protostellar sources (blue diamonds) and CHaMP ones (green squares), respectively, in the common surveyed area.

An interesting comparison can be carried out with the data coming from the Census of High- and Medium-mass Protostars (CHaMP) survey (Barnes et al. 2011; Ma et al. 2013). The 303 CHaMP sources were identified in HCO^+(1–0) Mopra observations in the coordinate range $280^\circ < \ell < 300^\circ$, $-4^\circ < b < 2^\circ$ (Barnes et al. 2011). Masses were estimated from HCO^+(1–0), while collecting *MSX*, *IRAS* and SIMBA-SEST photometry SEDs were built to estimate the bolometric luminosity and, at $\lambda \geq 60$ μm, the temperature of the cold envelope (Ma et al. 2013).

The most striking difference between the CHaMP and Hi-GAL source global behaviour lies in the statistics of $L_{\rm bol}/M$ (Ma et al. 2013, their fig. 2, *d*, and our Fig. 13, respectively). In their case, the $L_{\rm bol}/M$ distribution peaks at a few tens of $L_\odot/M_\odot$, while in our case, for the protostellar population, the peak position is found to be smaller by about one order of magnitude. To check this discrepancy, we searched for the Hi-GAL protostellar sources having a positional match with the ones of the CHaMP catalogue. In the common surveyed area, we found 6513 and 77 sources for Hi-GAL and CHaMP, respectively, with 69 matches within a searching radius of 2 arcmin. Cases of multiple associations were resolved keeping only the Hi-GAL closest counterpart of each CHaMP source. In this way, distance-independent quantities such as T and $L_{\rm bol}/M$ can be directly compared. Instead, M and $L_{\rm bol}$ depend on the distance adopted in the two different surveys, so that the best way to compare them is to rescale these quantities to report them to the same virtual distance $d_{\rm v}$, similarly to the procedure adopted in the previous section.

Figs D1 and D2 illustrate a comparison of the two surveys, in the overlap area. In the former, the angular disposition of the sources is shown, while in the latter masses and luminosities, scaled at $d_{\rm v} = 1$ kpc, are compared (top left- and right-hand panels, respectively). Both quantities show a wide spread around the 1:1 relation. While masses were determined using different methods, the differences in luminosity can be deduced from the different ways the SEDs were built: On one hand, CHaMP uses *IRAS* fluxes, which are expected to come from an area in the sky remarkably larger than that of the typical Hi-GAL sources (so the resulting luminosity tends to be significantly larger), while, on the other hand, such CHaMP SEDs do not cover the crucial range 100–500 μm in which emission from cold dust peaks, thus potentially neglecting part of the clump FIR luminosity. The first effect seems to be prevailing in the majority of cases, being the median of $L_{\rm bol,\,CH}/L_{\rm bol,\,HG} \sim 16$. Furthermore, since the FIR portion of the CHaMP SEDs generally peaks at shorter wavelengths than Hi-GAL SEDs, also the envelope temperatures are systematically found to be higher in the former case, as clearly shown in the right-hand lower panel of Fig. D2. All these contributions lead to shifting the CHaMP distribution of $L_{\rm bol}/M$ compared with Hi-GAL (left-hand lower panel), so that the median value for the ratio between $L_{\rm bol}/M$ of CHaMP and Hi-GAL is ∼4.

A more direct comparison can be carried out with first results of the *Herschel* key-programme The Earliest Phases of Star formation (EPoS, Ragan et al. 2012). This programme consisted of a PACS and SPIRE photometric mapping survey of objects known to be in the cold early phases of star formation. A total of 60 targets were observed, 45 of which corresponding to high-mass star-forming regions, in which Ragan et al. (2012) found 496 compact sources. Out of these, 90 lie in the portion of the Galactic plane considered in this paper [43 in the first quadrant and 47 in the fourth one, Fig. D3(a) and (b), respectively]. The sources were detected only in PACS images at 70, 100 and 160 μm, respectively. SPIRE maps were not used either for detecting counterparts or, even more so, for extracting photometry at these wavelengths. This prevents an exact match between the 90 EPoS objects and the entries of our Hi-GAL physical catalogue: First, in several cases, clusters of PACS EPoS sources might correspond to a single SPIRE counterpart due to different resolutions, and, secondly, possible Hi-GAL equivalents of EPoS sources might not survive the selection process described in Section 3.1 and based on SED regularity between 160 and 500 μm. In the end, we found 50 matches between the list of Ragan et al. (2012) and our Hi-GAL physical catalogue, within a searching radius of 1 arcmin.

For these sources, the fluxes at 70 and 160 μm can be directly compared (Fig. D4, left- and right-hand panels, respectively).[8] In both cases, the Hi-GAL ones appear generally overestimated with respect to the EPoS ones. The most general reason of this discrepancy has to be searched in the different way the fluxes were extracted in the two cases. Ragan et al. (2012) carried out PSF photometry, implicitly assuming a point-like appearance of the sources, while in this work *compact sources* were extracted with CuTEx, thus considering that source sizes can extend up to a few PSFs and consequently measuring larger total fluxes over larger areas. This aspect is emphasized in Fig. D4, using different colours for denoting the

[8] The number of comparable sources is actually smaller than 50, due to a possible lack of a flux at 70 or at 160 μm in the Hi-GAL SED.

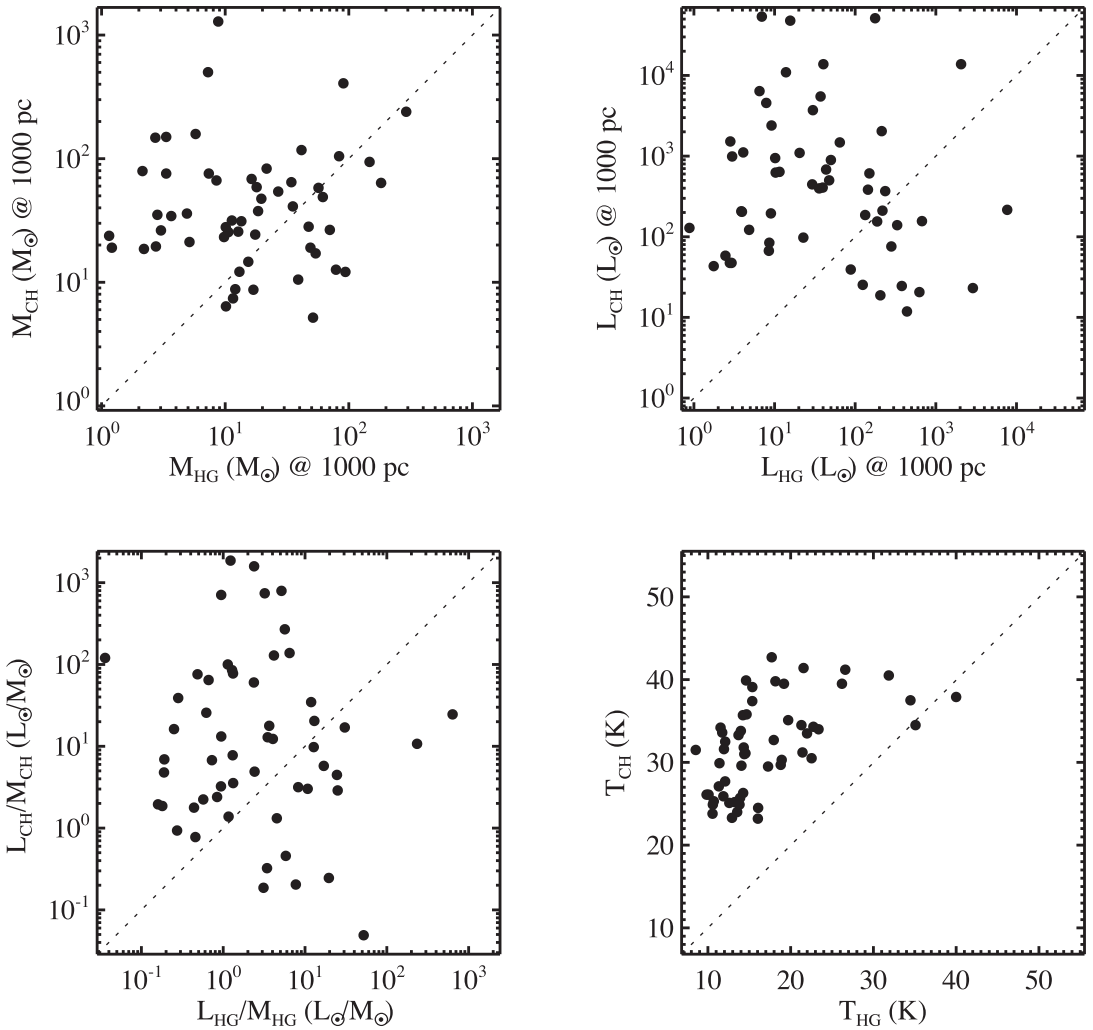

Figure D2. Comparison of physical properties derived for Hi-GAL and CHaMP compact sources. Top left-hand panel: comparison of masses for sources found in both surveys; masses are scaled to a common distance of 1 kpc to allow unbiased comparison. Top right-hand panel: the same as in the previous panel, but for bolometric luminosities. Bottom left-hand panel: comparison of L_{bol}/M ratios (distance-independent) for the sources of the two previous panels. Bottom right-hand panel: the same as in the previous panel, but for temperatures. In all panels, the bisector corresponding to the 1:1 relation is represented as a dotted line.

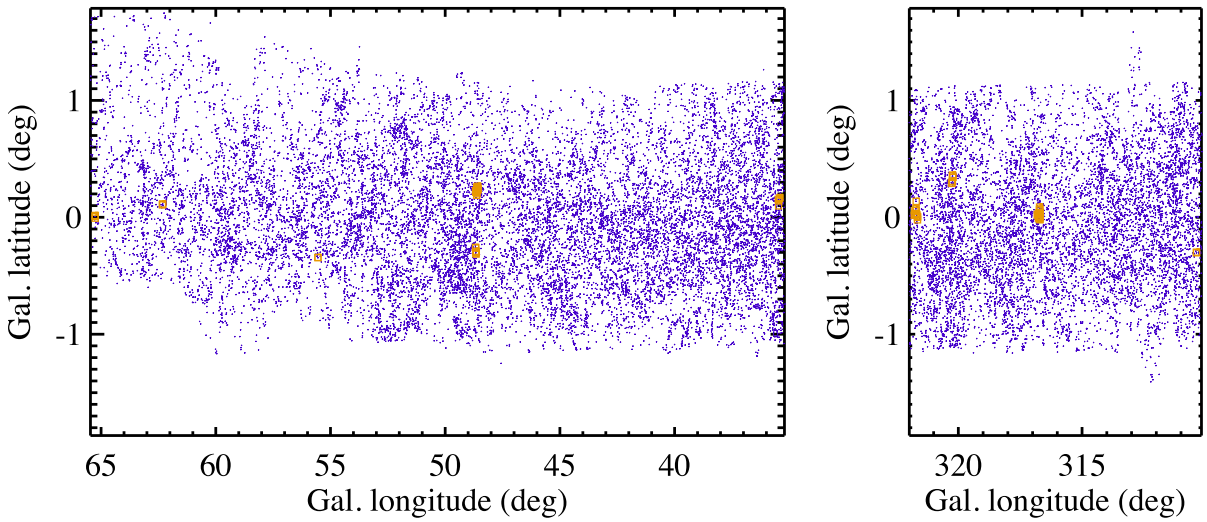

Figure D3. Spatial disposition of Hi-GAL (blue dots) and EPoS (gold squares) sources, respectively, in the common surveyed areas in the first (left-hand panel) and the fourth (right-hand panel) Galactic quadrants, respectively.

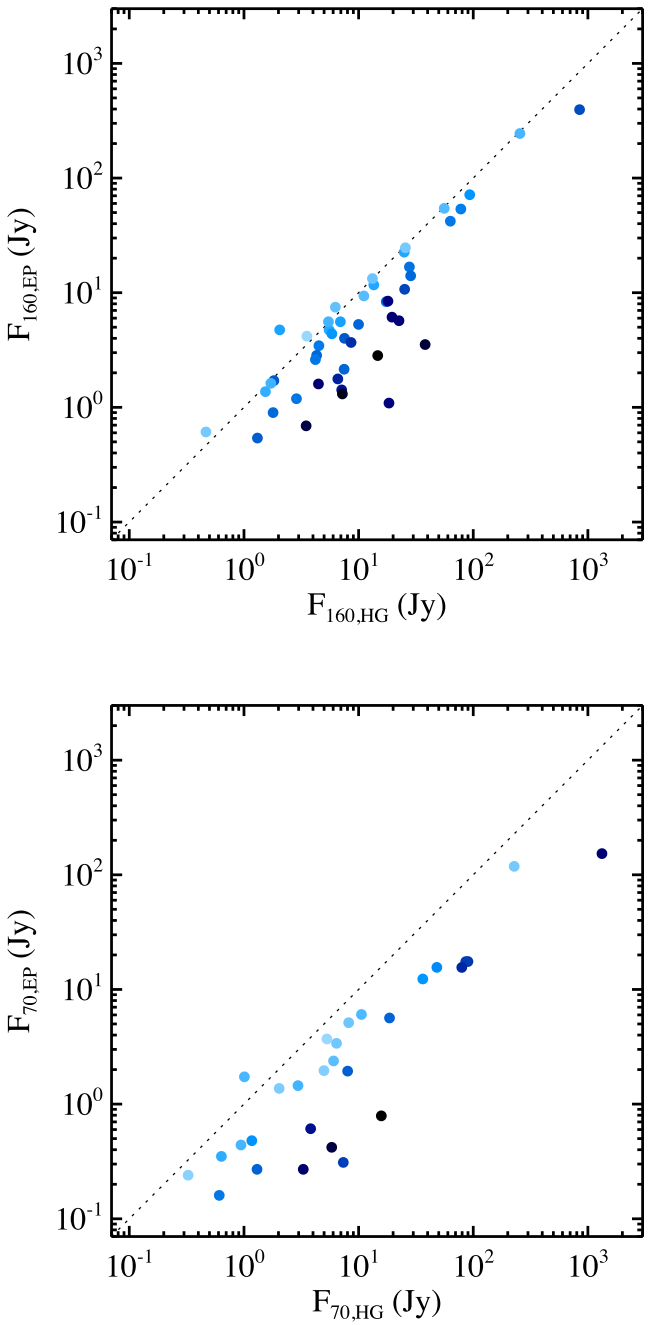

Figure D4. Comparison of EPoS versus Hi-GAL integrated fluxes at 70 (bottom panel) and 160 μm (top panel), respectively. Different shades of blue are used to represent the size of the Hi-GAL source (estimated as the average FWHM of 2D Gaussian resulting from the fit performed by CuTEX), to highlight that larger flux discrepancies correspond to larger estimates of the Hi-GAL source sizes: The lightest blue level corresponds to the smallest sizes found at 70 and 160 μm (9 and 12.4 arcsec, respectively), while black corresponds to the largest sizes (23.7 and 40.8 arcsec, respectively).

different source sizes of the Hi-GAL sources; as a general trend, the photometric data of the two surveys depart from equality as the source size estimates in Hi-GAL depart from the PSF extent.[9]

Photometric discrepancies are among possible explanations of further differences found by comparing physical properties of the two source lists, analysed in Fig. D5. EPoS source temperatures are found to be overestimated compared with those in Hi-GAL (top left-hand panel). This is expected due to the different wavelength range explored and considered for the grey-body fit, being the latter more suited to trace the peak of the cold dust (see a similar discussion in Fontani et al. 2005). This is also the main reason of generally finding lower mass estimates in EPoS than in Hi-GAL (after rescaling both at a virtual distance $d_v = 1$ kpc), as shown in Fig. D5, top right-hand panel: As a general trend, the larger is the temperature discrepancy, the larger is, consequently, the mass discrepancy. EPoS bolometric luminosities are generally smaller than Hi-GAL ones (bottom left-hand panel), being the median ratio of the two equal to ∼0.26. This is due to the wider spectral coverage of the SEDs in this paper, potentially going from 21 μm to 1.1 mm, and also to the lower fluxes measured in EPoS at 70 and 160 μm, as described above. Finally, combining the information contained in the two previous panels, in the bottom right-hand panel, we show the comparison of the L_{bol}/M ratio for the two surveys: This ratio is generally larger for EPoS, despite the larger luminosities found in Hi-GAL since masses at the denominator overcompensate for that. Furthermore, the largest discrepancies correspond to the largest temperature discrepancies.

The above comparison shows that both the considered spectral range and adopted photometry strategy can lead to quite different interpretations of the physical and evolutionary status of the same source. This must be kept in mind while discussing the results presented in this paper as well as while comparing the present Hi-GAL catalogue with other catalogues of similar sources. Particular care, for instance, has to be taken while comparing Hi-GAL clump properties with those derived for two single-band sub-mm surveys, namely ATLASGAL and BGPS, whose data have also been used in this work. Starting with the former, we compare Hi-GAL clump masses derived in this work with those derived using only the ATLASGAL flux at 870 μm (Wienen et al. 2015). Notice that in this last work, the masses are based on the fluxes of Contreras et al. (2013) and Urquhart et al. (2014b) typically much larger than those in the catalogue of Csengeri et al. (2014), due to different estimates of the source size. As a consequence of this, we could not establish an immediate association between Hi-GAL and ATLASGAL sources of Wienen et al. (2015) by simply exploiting the ATLASGAL counterparts already quoted in our catalogue (which instead are taken from Csengeri et al. 2014), but we had to search for positional matching within a searching radius of 36 arcsec, i.e. the centroid position accuracy provided by Wienen et al. (2015). In Fig. D6, top panel, a comparison of masses is shown; to make it meaningful, the masses of both lists have been rescaled to a virtual distance of 1 kpc, as also done in the previous comparisons with other surveys. Two main aspects are evident in the plot: (i) a certain degree of spread present around a linear relation , mostly due to the spread in Hi-GAL temperature, as opposed to the fact that masses of Wienen et al. (2015) are obtained for a fixed temperature (namely 23.1 and 20.8 K for the fourth and first Galactic quadrants, respectively), as highlighted by the colour scale adopted to represent the Hi-GAL temperature; and (ii) a remarkable departure of this trend from a 1:1 behaviour, in which the masses of Wienen et al. (2015) are larger than the Hi-GAL ones. This is essentially related to the aforementioned discrepancy between source sizes. In Fig. D6,

[9] Due to PACS on-board coadding, in *Herschel* parallel mode at 60 arcsec s^{-1} the PSFs turn out to be elongated along the scan direction (see e.g. Molinari et al. 2016a), being 5.9 × 12.1 arcsec^2 at 70 μm and 11.6 × 15.7 arcsec^2 at 160 μm (PACS Observer's Manual, v.2.5.1), which correspond to a circularized FWHM of 8.4 and 13.5 arcsec^2, respectively.

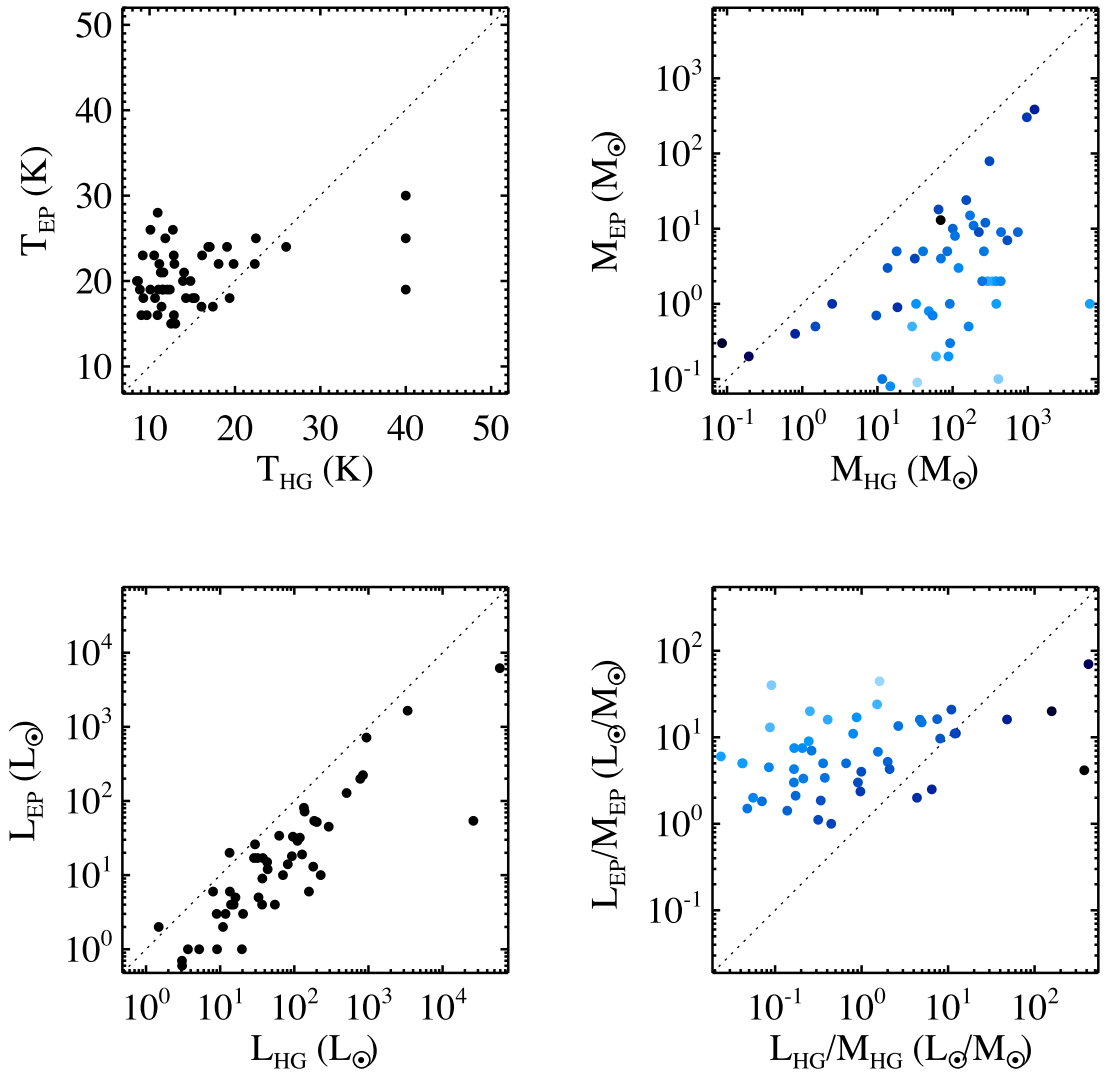

Figure D5. Comparison of physical properties derived for Hi-GAL and EPoS (Ragan et al. 2012) compact sources. Top left-hand panel: comparison of temperatures for sources found in both surveys. Top right-hand panel: the same as in the previous panel, but for masses scaled to a common virtual distance of 1 kpc to allow unbiased comparison. Different shades of blue are used for the symbols to represent the $\Delta T = T_{\rm HG} - T_{\rm EP}$ temperature discrepancy between Hi-GAL and EPoS for each source, going from 21 K (black) to −17 K (light blue). Bottom left-hand panel: the same as in the top left-hand panel, but for bolometric luminosities scaled to a common virtual distance of 1 kpc. Bottom right-hand panel: comparison of $L_{\rm bol}/M$ ratios for the sources of the previous panels. Different shades of blue are used as in the top right-hand panel. Finally, in all panels, the bisector corresponding to the 1:1 relation is represented as a dotted line.

bottom panel, it can be seen how rescaled diameters (or, equivalently, angular sizes) of sources determined by Wienen et al. (2015) are systematically and significantly larger than those observed for Hi-GAL sources, so that the fluxes (and, correspondingly, the masses) are evaluated over larger areas of the sky.

In a similar way, it is possible to make a comparison of masses derived in this paper and those of a sample of massive BGPS sources studied in Svoboda et al. (2016). In this case, the BGPS source designation used is the same as in the BGPS catalogue (i.e. Ginsburg et al. 2013). Similarly to the ATLASGAL case, the majority of BGPS masses appear in excess compared to Hi-GAL (Fig. D7, top panel), typically as a consequence of a larger angular size assigned to the source (Fig. D7, centre panel). Again, the spread in mass differences appears mostly due to the spread of Hi-GAL source grey-body temperatures.

This comparative analysis with BGPS parameters offers us the opportunity of testing the heliocentric distances used in our catalogue ($d_{\rm HG}$). The comparison with BGPS distances ($d_{\rm BC}$), derived by Ellsworth-Bowers et al. (2013, 2015), is shown in the bottom panel of Fig. D7. A significant number of points are located close to the bisector (459 within $|d_{\rm BC} - d_{\rm HG}| < 1$ kpc, out of 816 plotted points), demonstrating a good agreement between the two methods in these cases. Using a different colour for sources of our catalogue for which the near/far distance ambiguity is not solved (so that the far distance is chosen by default and a bad-quality flag is assigned, see Section 3.4), it can be seen that in several cases the validity of such choice is supported by a good agreement with a BGPS distance. Departures from the 1:1 behaviour, following peculiar trends (e.g. the one at $5 \lesssim d_{\rm HG} \lesssim 7$ kpc) are ascribable to different Galactic rotation models adopted. Another trend is clearly visible along the 'orthogonal' direction, easily explainable with cases in which the near distance estimate has been assigned in one of the two catalogues, and the far distance in the other. This trend is not as tight as the one around the bisector: Delimiting by eye the region

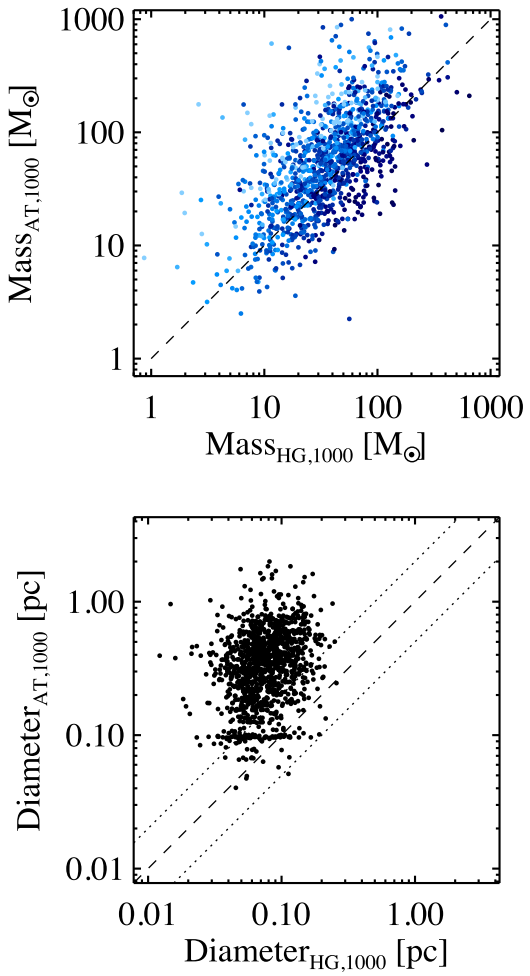

Figure D6. Comparison of physical properties derived for Hi-GAL and ATLASGAL (Wienen et al. 2015) compact sources, rescaled to a common virtual distance $d_v = 1$ kpc. Top panel: comparison of masses for sources found in both surveys. Different shades of blue are used for the symbols to represent the Hi-GAL temperature going from 5 K (black) to 30 K (light blue). The grey-dashed line represents the 1:1 relation. Bottom panel: comparison of diameters, rescaled to d_v. The grey-dashed line represents the 1:1 relation, while the dotted lines correspond to the ratios 2 and 0.5, respectively.

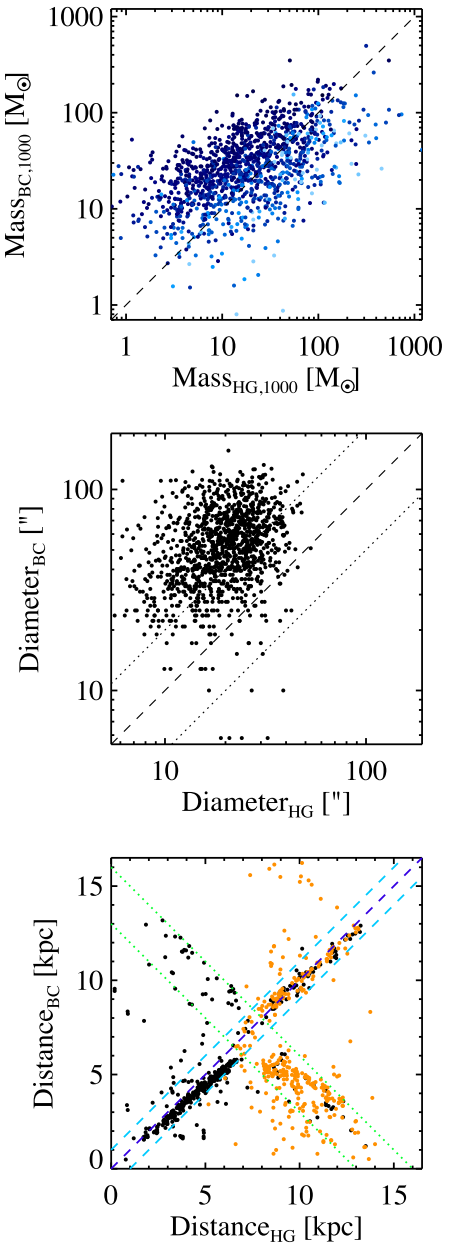

Figure D7. Middle panel: the same as the top and bottom panels of Fig. D6, respectively, but for BGPS sources (Svoboda et al. 2016). Top panel: Angular beam-deconvolved diameters are compared, instead of linear sizes, this information being directly available in the catalogue of Svoboda et al. (2016). Bottom panel: comparison of heliocentric BGPS and Hi-GAL distances: Black dots are sources for which the far/near Hi-GAL distance ambiguity has been fully solved in this work and orange dots for the less reliable cases in which the far distance has been assumed as the final decision due to a lack of other indicators. The bisector corresponding to the 1:1 relation is represented as a dark-blue dashed line; two further light-blue dashed lines are plotted 1 kpc above and below it, respectively. Two green dotted lines represent the region populated by sources for which the near/far distance ambiguity has been solved in opposite ways in the two catalogues.

populated by sources following this trend (see figure), and neglecting the area corresponding to the intersection with the ±1 kpc belt around the bisector, we find 226 sources characterized by this discrepancy. Noticeably, in the lower part of this area, corresponding to sources with an assigned far distance in our catalogue, such assignment is flagged in most cases as 'bad quality'. Finally, a total of 131 sources (i.e. the 16 per cent of the sources considered for this test) remain out of these two main trends, and correspond to distances that can not be reconciled by simply changing the near/far decision.

[1]*INAF-IAPS, via del Fosso del Cavaliere 100, I-00133 Roma, Italy*
[2]*Space Telescope Science Institute, 3700 San Martin Dr., Baltimore, MD 21218, USA*
[3]*Astrophysics Research Institute, Liverpool John Moores University, Liverpool Science Park Ic2, 146 Brownlow Hill, Liverpool L3 5RF, UK*
[4]*Aix Marseille Univ., CNRS, LAM, Laboratoire d'Astrophysique de Marseille, F-13388 Marseille, France*
[5]*Max Planck Institute for Astronomy, Königstuhl 17, D-69117 Heidelberg, Germany*
[6]*Infrared Processing Analysis Center, California Institute of Technology, 770 South Wilson Ave., Pasadena, CA 91125, USA*
[7]*Dipartimento di Matematica e Fisica, Università del Salento, I-73100, Lecce, Italy*
[8]*CNRS, IRAP, 9 Av. colonel Roche, BP 44346, F-31028 Toulouse cedex 4, France*
[9]*Université de Toulouse, UPS-OMP, IRAP, F-31028 Toulouse cedex 4, France*
[10]*Department of Physics, Nagoya University, Chikusa-ku, Nagoya, Aichi 464-8601, Japan*
[11]*Department of Physics and Astronomy, University of Calgary, AB T2N 1N4, Canada*
[12]*Center for Astrophysics and Space Astronomy, University of Colorado, Boulder, CO 80309, USA*
[13]*Canadian Institute for Theoretical Astrophysics, University of Toronto, McLennan Physical Laboratories, 60 St. George Street, Toronto, Ontario, Canada*
[14]*School of Physics and Astronomy, University of Leeds, Leeds LS2 9JT, UK*
[15]*School of Physics and Astronomy, Cardiff University, Cardiff CF24 3AA, UK*
[16]*IPAG, University Grenoble Alpes, F-38000 Grenoble, France*
[17]*AIM Paris-Saclay, CEA/IRFU – CNRS/INSU – Univ. Paris Diderot, Service d'Astrophysique, CEA-Saclay, F-91191 Gif-sur-Yvette Cedex, France*
[18]*INAF, Osservatorio Astrofisico di Arcetri, Largo E. Fermi 5, I-50125 Firenze, Italy*
[19]*I. Physik. Institut, University of Cologne, Zülpicher Strasse, D-50937 Köln, Germany*
[20]*European Southern Observatory, Karl Schwarzschild str. 2, D-85748 Garching, Germany*
[21]*Max-Planck-Institut für Radioastronomie, Auf dem Hügel 69, D-53121 Bonn, Germany*
[22]*ASI Science Data Centre, I-00044 Frascati, Roma, Italy*
[23]*ESA/ESAC, PO Box 78, Villanueva de la Cañada, E-28691 Madrid, Spain*
[24]*Dipartimento di Fisica e Scienze della Terra, Università degli Studi di Ferrara e Sezione INFN di Ferrara, via Saragat 1, I-44100 Ferrara, Italy*
[25]*Instituto de Astrofísica e Ciências do Espaço, Universidade do Porto, CAUP, Rua das Estrelas, P-4150-762 Porto, Portugal*
[26]*Dipartimento di Fisica, Università di Roma 'La Sapienza', P.le Aldo Moro 2, I-00138 Roma, Italy*
[27]*DIET, Università di Roma 'La Sapienza', I-00185 Roma, Italy*
[28]*ESA, Directorate of Science, Science Support Office, ESTEC/SCI-S, Keplerlaan 1, NL-2201 AZ Noordwijk, the Netherlands*
[29]*Departamento de Fisica, Universidad de Atacama, Copayapu 485, 1530000 Copiapó, Chile*
[30]*Observatoire de l'Université de Genève, 51 chemin des Maillettes, CH-1290 Sauverny, Switzerland*
[31]*Observatoire Astronomique de Strasbourg, Université de Strasbourg, CNRS, UMR 7550, 11 rue de l'Université, F-67000 Strasbourg, France*
[32]*CAS Key Laboratory of Space Astronomy and Technology, National Astronomical Observatories, Chinese Academy of Sciences, Beijing 100012, China*
[33]*Département de physique, de génie physique et d'optique and Centre de recherche en Astrophysique du Québec, Université Laval, 1045 avenue de la médecine, Québec G1V 0A6, Canada*
[34]*Italian ALMA Regional Centre, INAF-IRA, Via P. Gobetti 101, I-40129 Bologna, Italy*
[35]*Centre for Astrophysics Research, School of Physics, Astronomy and Mathematics, University of Hertfordshire, College Lane, Hatfield AL10 9AB, UK*
[36]*INAF – Astrophysical Observatory of Catania, Via Santa Sofia 78, I-95123 Catania, Italy*
[37]*Jeremiah Horrocks Institute, University of Central Lancashire, Preston PR1 2HE, UK*
[38]*CERN, 385 Route de Meyrin, CH-1217 Meyrin, Switzerland*
[39]*INAF – Astronomical Observatory of Capodimonte, via Moiariello 16, I-80131 Napoli, Italy*
[40]*INAF – Osservatorio Astronomico di Trieste, via G.B. Tiepolo 11, I-34131 Trieste, Italy*
[41]*Department of Physics 'E.Pancini', University Federico II, via Cinthia 6, I-80126 Napoli, Italy*
[42]*Institute for Computer Science and Control (MTA SZTAKI), Laboratory of Parallel and Distributed Systems, Victor Hugo u. 18-22, Budapest 1132, Hungary*
[43]*Department of Physics and Astronomy, University College London, London WC1E 6BT, UK*
[44]*STFC, Rutherford Appleton Labs, Didcot OX1 1QX, UK*
[45]*Nobeyama Radio Observatory, 462-2 Nobeyama Minamimaki-mura, Minamisaku-gun, Nagano 384-1305, Japan*

This paper has been typeset from a TEX/LATEX file prepared by the author.